1979

Part I. The hadron spectrum at ground level; Part II. The stability of the period of Cygnus X-3

Robert Keith Fickle
Iowa State University

Part I - The hadron spectrum at ground level
Part II - The stability of the period of Cygnus X-3

by

Robert Keith Fickle

A Dissertation Submitted to the
Graduate Faculty in Partial Fulfillment of
The Requirements for the Degree of
DOCTOR OF PHILOSOPHY

Major: Physics

Approved:

Signature was redacted for privacy.

In Charge of Major Work

Signature was redacted for privacy.

For the Major Department

Signature was redacted for privacy.

For the Graduate College

Iowa State University
Ames, Iowa
1979

TABLE OF CONTENTS

LIST OF FIGURES

LIST OF TABLES

INTRODUCTION

This thesis is divided into two parts, corresponding to two separate research projects. The first part deals with a study of cosmic ray hadrons at ground level in the energy range 30-1000 GeV. The study was performed at Iowa State University with an apparatus whose principal elements were a calorimeter for determining particle energies and a large atmospheric pressure gas Cerenkov counter used to investigate particle velocities. The results of the experiment show the cosmic ray spectrum to be consistent with a simple power law over the full range of energies investigated; an upper limit on the flux of massive particles is also derived.

The second part of the thesis describes a study of the periodically variable X-ray source Cygnus X-3. The source was observed in January 1978 using the SAS-3 X-ray astronomy satellite, and an anomalous phase was found for the 4.8-hr variation of the X-ray intensity. Analysis shows the anomaly to be explained as the result of a continuous change in the period at a rate $\frac{\dot{P}}{P} = 5.1 \pm 1.3 \times 10^{-6} \mathrm{yr}^{-1}$, which is consistent with previous upper limits on the period derivative and in agreement with the predictions of several models.

PART I. THE HADRON SPECTRUM AT GROUND LEVEL

INTRODUCTION

The study of cosmic rays has been of great importance in developing our understanding of particle physics. Though the large accelerators have nearly replaced cosmic rays as a source of high energy particles, the latter still provide significant information in some areas. The most obvious deficiency of accelerators is that their energies are currently limited to $\sim 10^{12}$ eV in the lab frame, while the cosmic ray spectrum extends to at least 10^{21} eV. Thus cosmic ray experiments continue to provide hints of the phenomena to be found at energies inaccessible to present-day accelerators.

There are, of course, disadvantages to doing particle physics via cosmic rays. The intensity of particles is much lower than that available at accelerators; this is particularly true at high energies, due to the steepness of the cosmic ray spectrum. Thus detectors must have large geometric acceptance, typically one or more m^2sr for energies near 10^{12} eV. To get this at a reasonable cost, one sacrifices complexity of design and consequently much of the detailed information on interaction characteristics which would otherwise be available. In many cases, it is not even possible to identify the incident particle.

To help overcome these problems, some indirect methods have evolved for studying interactions. The atmosphere functions as a "target" in which incident particles interact; properties of interactions are obtained by studying the flux of secondary particles emerging from the interactions at depths in the atmosphere up to many interaction lengths. Experiments of this sort include air shower studies, measurements of the muon and neutrino fluxes, studies of the hadron spectrum at various atmospheric depths, searches for new kinds of particles, etc. Results available from the studies include the primary spectrum and composition, mean multiplicities of interactions, mean interaction lengths, transverse momentum distribution, and so forth.

The research on which this paper is based is a study of particle fluxes at ground level (atmospheric depth 990 g/cm^2). Since the interaction length of incident nucleons in air is about 100 g/cm^2, essentially none of the primary cosmic rays survive to this level and therefore the particles seen are reaction products. The general picture of secondary production in the atmosphere is indicated by the following reaction: nucleon + nucleus$\rightarrow$ $\pi^{\pm}$, π^0, p, $\bar{p}$, n, $\bar{n}$, strange particles, etc. Strange particles are less than 10% of the products, which we may ignore. "Etc." may include particles produced only at extremely high energies or under other conditions which

have prevented their observation at accelerators; one goal of cosmic ray studies of this sort is to search for such new particles. The charged pions, protons, and neutrons produced in the collision may each interact subsequently with air nuclei lower in the atmosphere, each producing another group of secondaries. Charged pions can also decay into muons, which do not interact strongly and survive to form the majority of the sea level flux. Neutral pions decay in 10^{-16} seconds to form γ rays which multiply to form electromagnetic showers or cascades of electrons and γ rays. The electromagnetic cascade process is described in some detail by Rossi[1]. In brief, a high energy γ ray will interact with an air nucleus to form an electron-positron pair. These electrons will each interact via bremsstrahlung collisions to form γ rays, which produce more pairs; the process continues to distribute the available energy among more and more particles until their average energy is too small for particle production to occur, at which point the shower begins to die away. Fig. 1 shows the genetic relation between the various components.

At sea level, the hadron intensity above 1 GeV/c[2,3,4] is about 4×10^{-4} $(cm^2\text{-}sr\text{-}s)^{-1}$ while the muon rate[5] is $\sim$ 8×10^{-3} $(cm^2\text{-}sr\text{-}s)^{-1}$. Electrons are about one-third as numerous as muons at low energies. The spectra of all species above 10 GeV tend to fall in power laws, $dN/dE \propto E^{-\gamma}$, with

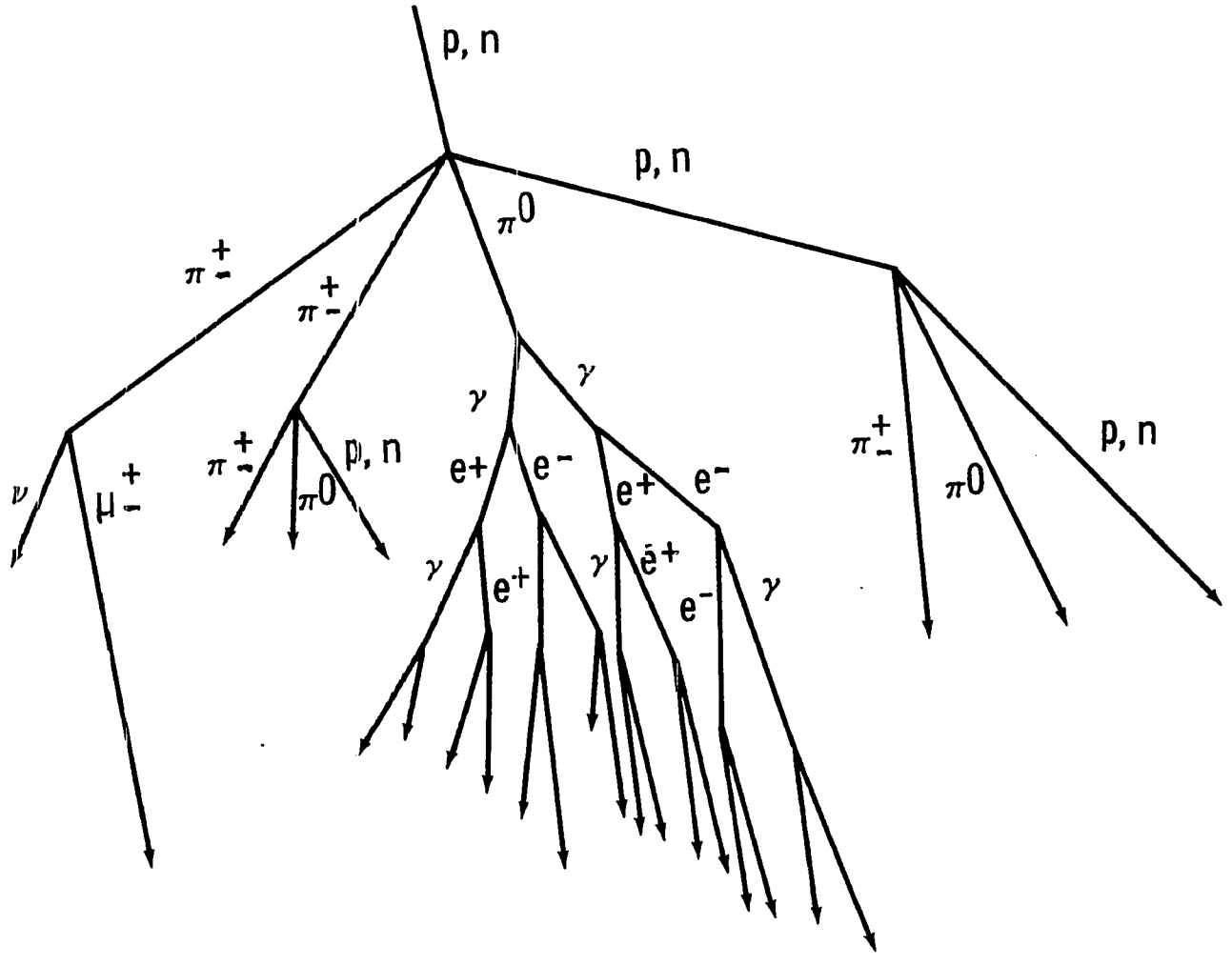

Fig. 1. Genetic relations between the various cosmic ray components

γ between 2.5 and 3. These intensities include both showers of particles produced by single cosmic ray primaries, and "single" particles, i.e. those whose accompanying showers have been absorbed in the atmosphere or are too far away to be detected.

The present experiment was originally designed to search for massive hadrons among cosmic rays. Particular motivation was provided by the work of Baruch, Brooke, and Kellermann[6,7,8] who interpreted their anomalous results with a sea level detector in the 10^{12} eV region as being due to production of massive particles (mass $\sim$40 GeV/c^2) in the atmosphere. Their results were later withdrawn, the anomaly being due to an electronic failure in their apparatus; however it did draw attention to the need for further study in this energy region. The emphasis of this experiment was thus shifted to a measurement of the hadron spectrum. The ability to investigate particle masses was retained as a unique feature of the apparatus, allowing the pion to proton ratio to be measured.

During the course of the research, a secondary objective of understanding the capabilities and limitations of the detector developed. The main detector element was a shallow calorimeter which gives a rough measure of incident energy with a minimal use of expensive equipment. The shallow calorimeter is potentially of great use in work above 10^{12} eV where deep calorimeters become increasingly expensive, and

some evaluation of its performance was desired. Sections of this paper dealing with the apparatus and with the results and conclusions contain some evaluation of the calorimeter. A calculation of muon interaction rates in the calorimeter was made, and this information is included in Appendix I. Also, a Monte Carlo simulation of hadron interactions was used to predict the response of the calorimeter to hadrons; these results are presented in Appendix II. The data on calorimeter performance may help determine the usefulness of such calorimeters for future experiments.

Review of Literature

One of the earliest measurements of sea level hadrons above 10 GeV was done by G. Brooke et al. at the University of Durham[2,3]. Their apparatus consisted of a magnetic spectrometer with trajectories determined with neon flash tubes. A neutron monitor was used to distinguish nuclear active particles (pions and protons) by their production of evaporation neutrons. Those particles with negative charge were taken to be pions, and the difference between negative and positive particle rates was attributed to protons. This involves the assumption that the hadrons observed are mostly pions and protons and that $\pi^{\pm}$ are produced in equal quantities in the atmosphere. The spectrum was measured up to 100 GeV for both pions and protons. A later

experiment by I.S. Diggory et al.[9] with a similar apparatus confirmed the results of Brooke et al. in the range 1-30 GeV.

Another apparatus used in studying hadrons is the calorimeter. In this detector the incident particle interacts with a target or absorber, such as iron, which is typically ten interaction lengths in thickness. Detectors are interleaved with the absorber to measure that portion of the incident energy - as much as 80% - which goes into ionization and similar processes. The energy deposition occurs mostly through the production of π^0's which decay to γ rays, thus transferring their energy to electromagnetic showers. The total ionization in the detectors is roughly proportional to the incident particle's energy over a wide range;[10] computer simulations of the physical processes can yield more exact relations, if needed. This method was originally used by Grigorov et al.[11] and has been widely applied, since it can give energy resolutions of 20% at energies up to at least 10^{13} eV. The calorimeter detects neutrons, protons, and pions with equal ease; in fact, they can be distinguished only because the neutron has no charge. To obtain separate spectra of pions and protons, one may assume, for example that neutrons and protons have equal intensities, and that all other charged hadrons are pions.

An experiment by Cowan and Matthews[12] used a deep calorimeter of the sort described above to study hadrons

in the range 10^{11}-10^{13} eV at ground level (elevation 250 m). Their calorimeter consisted of six cloud chambers with 24 g/cm^2 carbon targets between the chambers, followed by eight layers of iron plate (each 80 g/cm^2) separated by ion chambers. With this arrangement, the cloud chambers could be used to study interactions of the incident particles in some detail, while the thick iron absorber assured a good measure of the total energy. The acceptance of the detector was 6500 cm^{2}sr.

Another calorimeter apparatus was operated at sea level by F. Siohan *et al.*[10]. Their device used eight iron absorbers, each 120 g/cm^2 thick, and seven layers of liquid scintillation counters. Four layers of spark chambers were also used to identify events visually. The acceptance was 6900 cm^{2}sr.

As mentioned above, both the magnetic spectrometers and deep calorimeters become expensive for applications above 10^{12} eV, which require rather large geometric acceptances. One solution is the shallow calorimeter, in which the target is thin enough that incident particles interact only once. The electromagnetic cascade resulting from π^0 decay following the interaction is allowed to develop in the absorber and sampled with a layer of detectors; the detector pulse is taken as a measure of the cascade energy and thus of the incident particle's energy. This method has the obvious shortcoming that the cascade size is only loosely related to the incident

energy; fluctuations in the fraction of incident energy given to π^0's and in the point of interaction make the energy determination uncertain by about a factor of two for individual events. The Monte Carlo simulations in Appendix II indicate that the hadron spectrum can be determined fairly well, provided that the spectral shape does not change rapidly with energy.

The shallow calorimeter method was first used by Dmitriev et al.[13] and was more recently revived by Baruch, Brooke, and Kellermann[6,7,8,14]. Baruch et al. used a target of graphite 60 g/cm^2 thick. A layer of lead 7 radiation lengths (r.l.) thick was placed under the target, followed by a layer of proportional detectors, followed by an additional 3 r.l. of lead and another layer of detectors. The proportional detectors were 3.5 cm in diameter. To eliminate events due to incident electrons, 8.6 r.l. thickness of lead shielding surrounded the apparatus. The detector was 4m^2 in area and flat enough to give nearly 2π angular acceptance. Baruch et al. chose their particular design to investigate closely spaced hadrons in air showers. The combination of large area, low cost, and the good spatial resolution provided by the proportional detectors was ideal for their purposes.

The three detector types described above account for most studies on hadrons at ground level. The hadron spectra found in the experiments referred to above are compared with

the spectrum determined by this experiment in the section of this paper dealing with results. Magnetic spectrometers have been successfully used at energies up to 100 GeV. At higher energies the deep calorimeter has received the most widespread use because it provides a fairly precise and unambiguous determination of incident energy and is easier to build in large geometries than magnetic spectrometers. For applications where good energy resolution is not required, the shallow calorimeter provides an even less expensive alternative.

In the remaining sections of this paper, the apparatus is first described in some detail. The data are then presented in various ways appropriate to understanding the physics. Results for the hadron spectrum and the π/p ratio are given. Finally, a summary of findings on the hadron spectrum and on the calorimeter performance is presented.

THE APPARATUS

The apparatus for this experiment was designed to search for massive particles like those postulated by Baruch et al.[8] A shallow calorimeter similar to theirs was thus chosen for energy determination. The particles hypothesized by Baruch et al. were expected to arrive with Lorentz factor γ of about 100, so a gas Cerenkov counter was added to investigate the velocities of incident particles. The Cerenkov counter is a major distinguishing feature not found in previous experiments at ground level.

Physical Arrangement

The apparatus is shown in Figs. 2 and 3. Fig. 2 is a side view of the apparatus. Fig. 3 shows a top view of the various detector layers. The main elements of the apparatus are a large volume gas Cerenkov counter and a single interaction target and shallow calorimeter. Velocity information from the Cerenkov counter and energy information from the calorimeter can be used to determine particle masses, allowing pions and protons to be distinguished. A typical event is sketched in Fig. 2. The hadron passes through the Cerenkov counter, then interacts in the target to produce secondaries, some of which are electromagnetic and form a cascade in the lead below the target.

The electronics logic was arranged so that an "event"

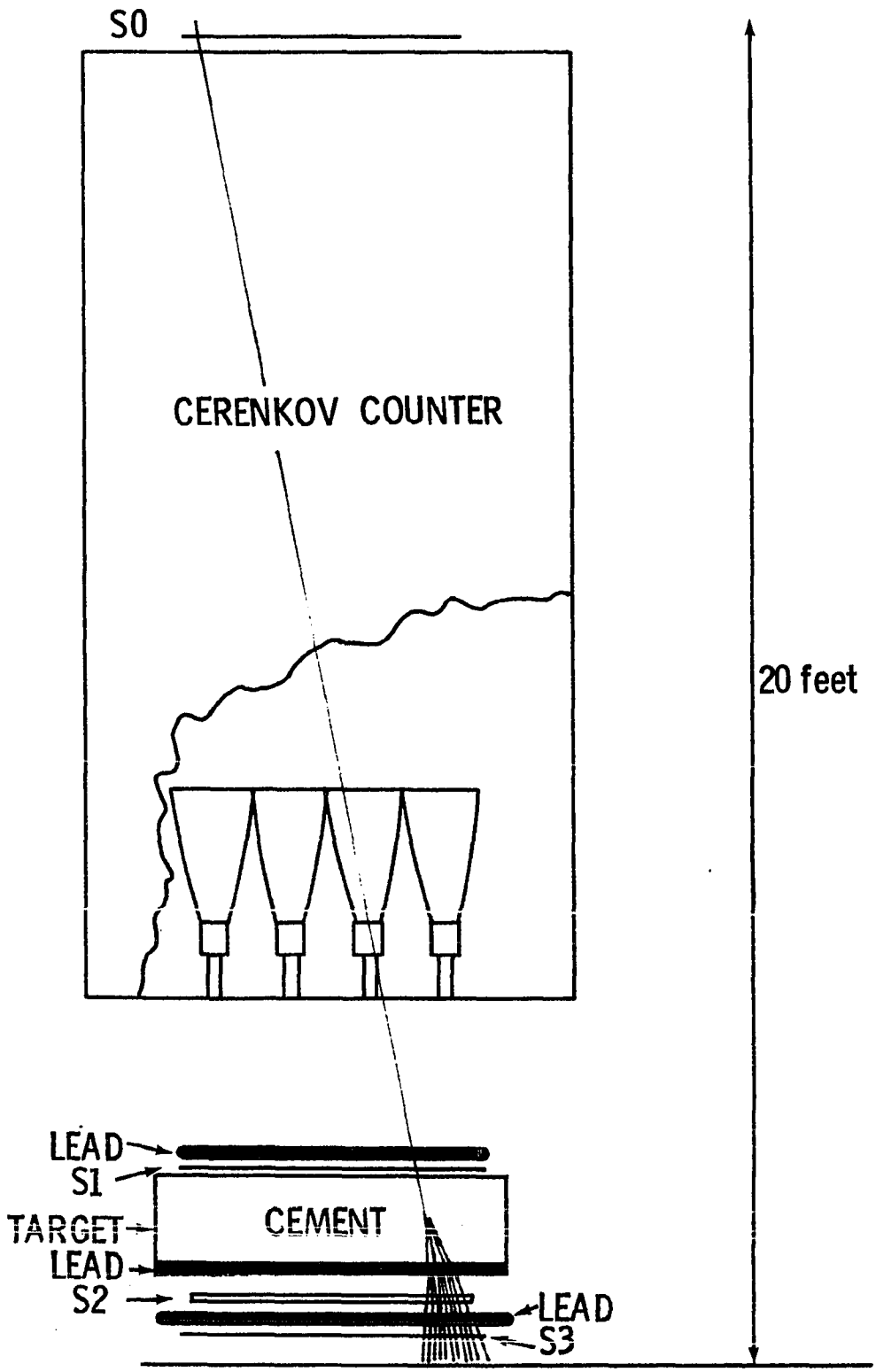

Fig. 2. Side view of the apparatus

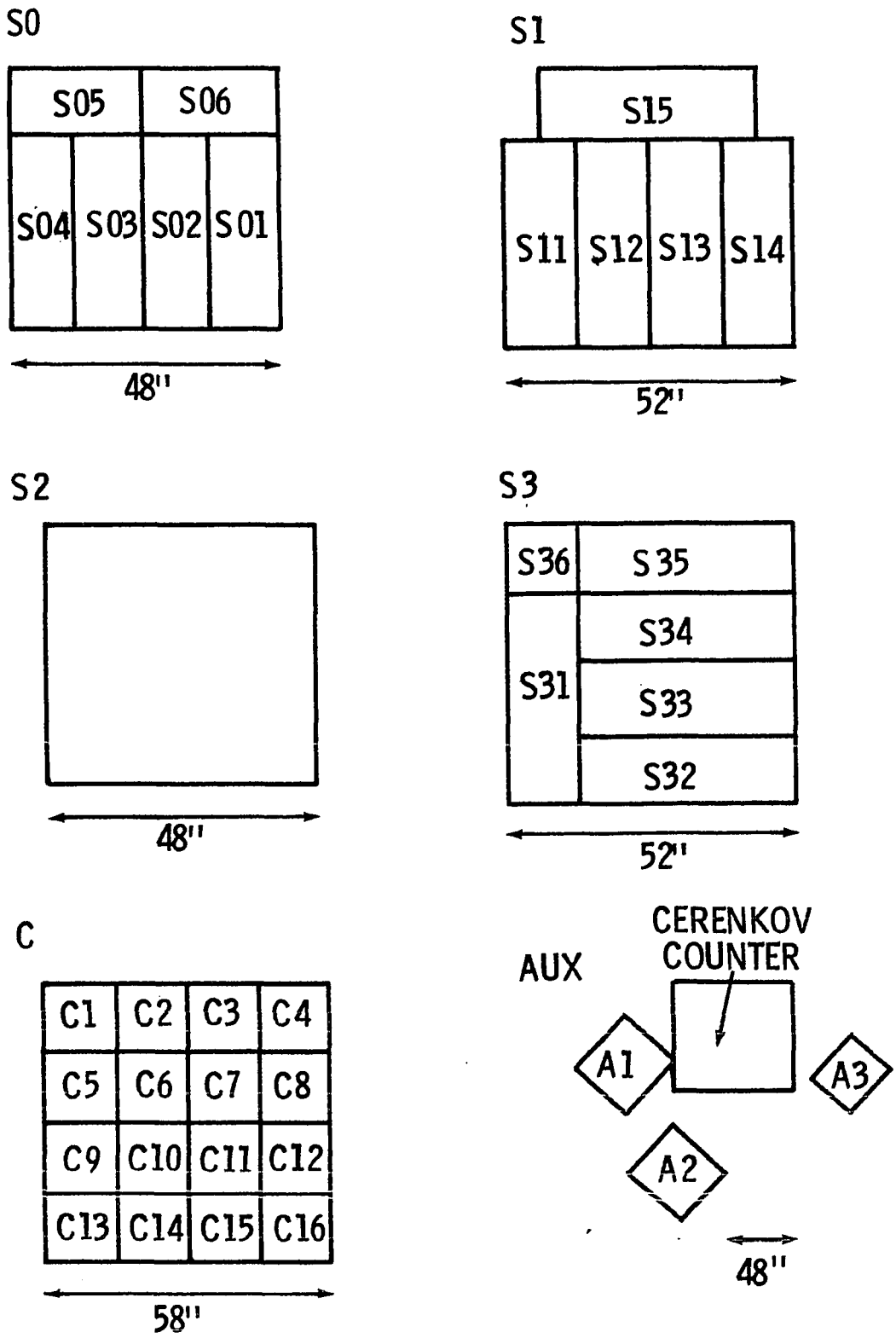

Fig. 3. Top view of the various detector layers

should correspond to the passage of a single cosmic ray hadron. Whenever signals from the triggering scintillators (S0 and S1) were in coincidence with a large pulse from the calorimeters (S2 or S3) an event was registered. The signals from all detectors were recorded for each event for later analysis. The triggering requirements could also be satisfied by electrons or muons which initiated electromagnetic cascades in the calorimeter. Electrons were eliminated by the layer of lead above the S1 detectors, and calculations of muon event rates (see Appendix I) showed them to be small compared to hadron rates at energies above 35 GeV. Thus events satisfying the trigger requirement were dominantly hadron-induced.

The Cerenkov counter used a gas filling at atmospheric pressure. The radiator pathlength of 3.5 m was chosen to give an inefficiency due to photoelectron statistics of less than 4% with a helium filling. In practice, an air filling was used for which the yield was 80 photons or $\sim$ 15 photoelectrons for β=1 particles. Cerenkov light was detected by sixteen photomultipliers mounted in light buckets made of aluminized mylar. Each light bucket was 14.5" square and the photomultipliers were 5" in diameter. This gives a 9% probability that an incident particle would strike the face of a photomultiplier, which must be considered in analyzing results of the Cerenkov counter's operation. A particle

striking a photomultiplier tube would produce a signal even if the particle produced no Cerenkov photons in the radiator. The enclosure was made air tight to allow filling with gases of various indices of refraction, and the interior was painted black so that only photons originating within the Cerenkov counter's nominal acceptance were detected.

The roof over the apparatus contained 23.5 g/cm^2 of cement and 8 g/cm^2 of roofing tar. It was estimated that 30% of incident hadrons would interact in the roof and thus be eliminated by triggering requirements. The target above the calorimeter was made of cement blocks stacked to a thickness of 108 g/cm^2. A layer of lead 3.3 r.l. in thickness served to develop the electromagnetic cascade from an interaction in the target. The cascade was viewed by scintillator S2, then developed further in another 3.3 r.l. of lead before being viewed by S3. The S3 layer consisted of six individual scintillation detectors, whose arrangement is shown in Fig. 3. S31-S35 were each 3/16" x 13" x 39", and S36 was 3/16" x 13" x 26"; each S3 scintillator was viewed by a single RCA 8575 photomultiplier. S2 was a single plastic scintillator 1.5" x 48" x 48" in size and was viewed by two EMI 9618 photomultipliers. The response of the S2 scintillator to single muons was measured as a function of position and was found to vary by no more than ±12% over the detector's area; for the S3 detectors, the response varied ±9%.

Also shown in Figs. 2 and 3 are the scintillator arrays S0, S1, and AUX. S0 and S1 helped define the acceptance of the apparatus. The layer of lead above S1, which was 9 r.l. thick, served to eliminate events caused by incident electrons; the pulse height from S1 was measured for each event in order to help eliminate events due to multiple incident particles, and also to identify interactions in the lead. AUX, an auxiliary scintillator array of total area $3.8 m^2$, was used to identify events accompanied by one or more particles near the calorimeter.

The operating voltages for the photomultipliers in S2 and S3 were chosen to give the smallest gain for which pulses could be measured easily. This was done to minimize saturation of the photomultipliers for large pulses; since saturation occurs when high current flows in the photomultipliers, the voltage (and thus the current) was kept to a minimum. The bases on the S3 photomultipliers were modified to allow pulses to be taken from the sixth dynode; pulses were taken from the eighth dynode of the S2 photomultipliers. These dynodes were chosen to get large enough signals to be measured readily while avoiding unnecessarily high multiplication gain.

Voltages for the other scintillators were set simply to provide enough gain to see single particles. The operating voltages for the Cerenkov counter photomultipliers were set

using a pulsed light-emitting diode to get equal gains from all 16 tubes.

Electronics

A system for automatic recording of data was developed for the apparatus. An "event" was defined electronically to be a group of signals satisfying the triggering requirement that a single charged particle traverse the Cerenkov counter and produce a large signal in S2 and/or S3. As previously explained such events are dominantly hadron induced.

The trigger logic for selecting events, shown in Fig. 4, may be written as S0·S1·(S2+S3). For Runs 15 and 16 only, the trigger was modified to be S1·(S2+S3) in order to increase the event rate by increasing the acceptance. Thresholds for S2 and S3 were set at levels corresponding to 50 or more particles traversing the scintillators. Trigger rates ranged from 1/hr to 10/hr depending on thresholds.

S0 and S1 were run in an "exclusive-OR" logic; i.e., the trigger required one and only one counter in S0 to fire, and one and only one counter in S1 to fire. This requirement was adopted when early runs showed most of the events to be air showers. Although the number of triggers by air showers was greatly reduced, hadrons with a small density of accompanying particles were not excluded. The AUX counters were added to investigate the properties of accompanying

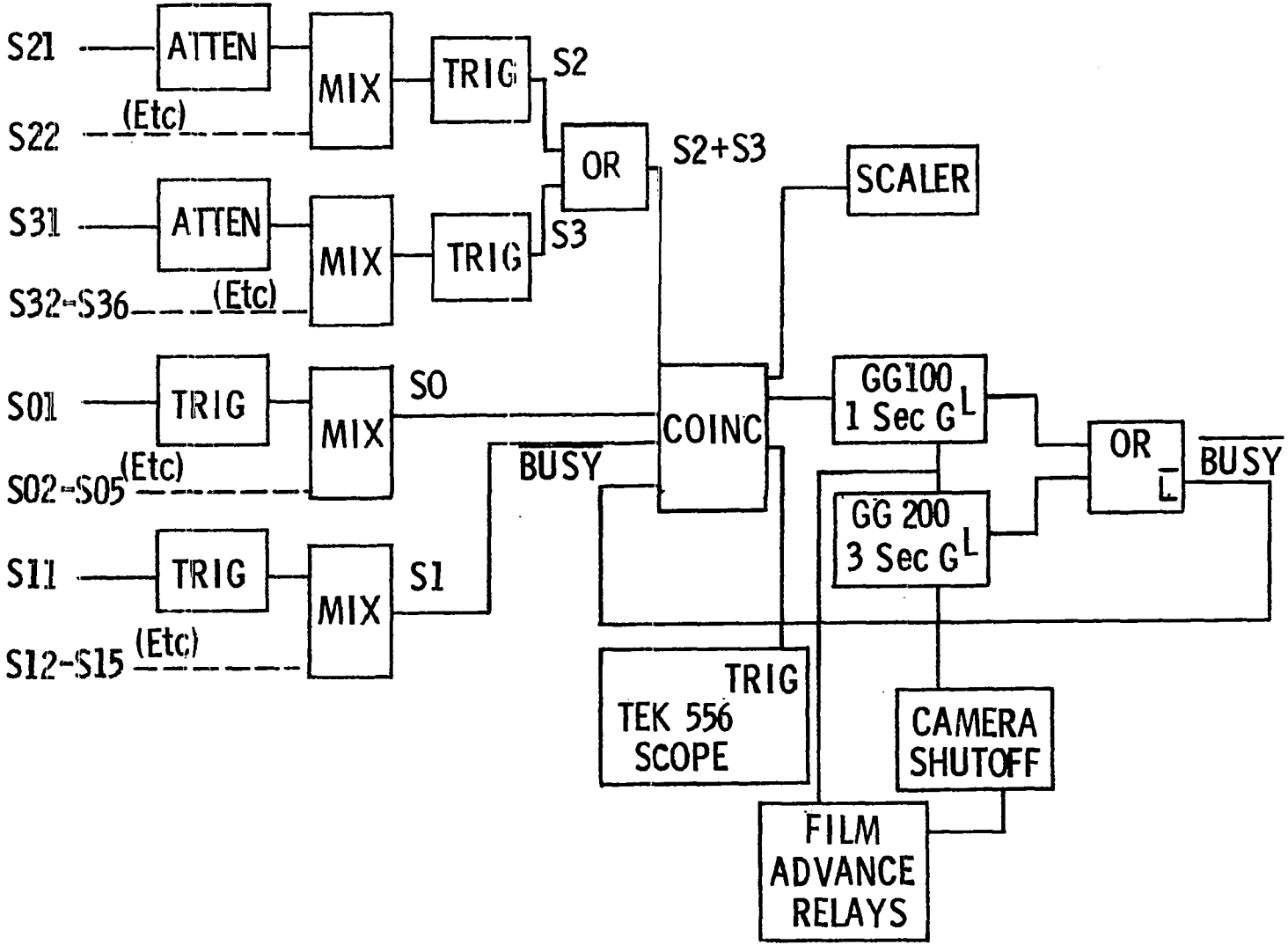

Fig. 4. Logic for event recognition

particles.

For Runs 15 and 16, the S0 array was removed from the triggering requirement so that the logic was S1·(S2+S3). This increased the acceptance by more than a factor of 10, allowing data on high energy events to be gathered rapidly, and the S0 signals were recorded so that no information was lost by this procedure.

To calculate the acceptance for the two different trigger modes, a computer program was written which divided the triggering detectors (S0 and S2 for Runs 1-14, S1 and S2 for Runs 15 and 16) into 40 x 40 square arrays. The acceptance of each pair of one square in the top layer and one square in the bottom was calculated, and the total acceptance was found as the sum over all pairs. A weighting factor was included in the calculation for the angular distribution of incident hadrons. Ashton and Saleh[15] found the hadron intensity to vary with zenith angle according to $I=I_0\cos^8\theta$. With this weighting an acceptance of 641 cm^2-sr for Runs 1-14 and 7460 cm^2-sr for Runs 15 and 16 was determined.

Signals from the Cerenkov counter and detectors S1, S2 and S3 were recorded as analog pulses by displaying them on a Tektronix 556 dual-beam oscilloscope and photographing the display with an automatic camera. The display electronics are shown in Fig. 5. Pulses were displayed at 100 ns/div., using delay cables of up to 500 ns to space the pulses along

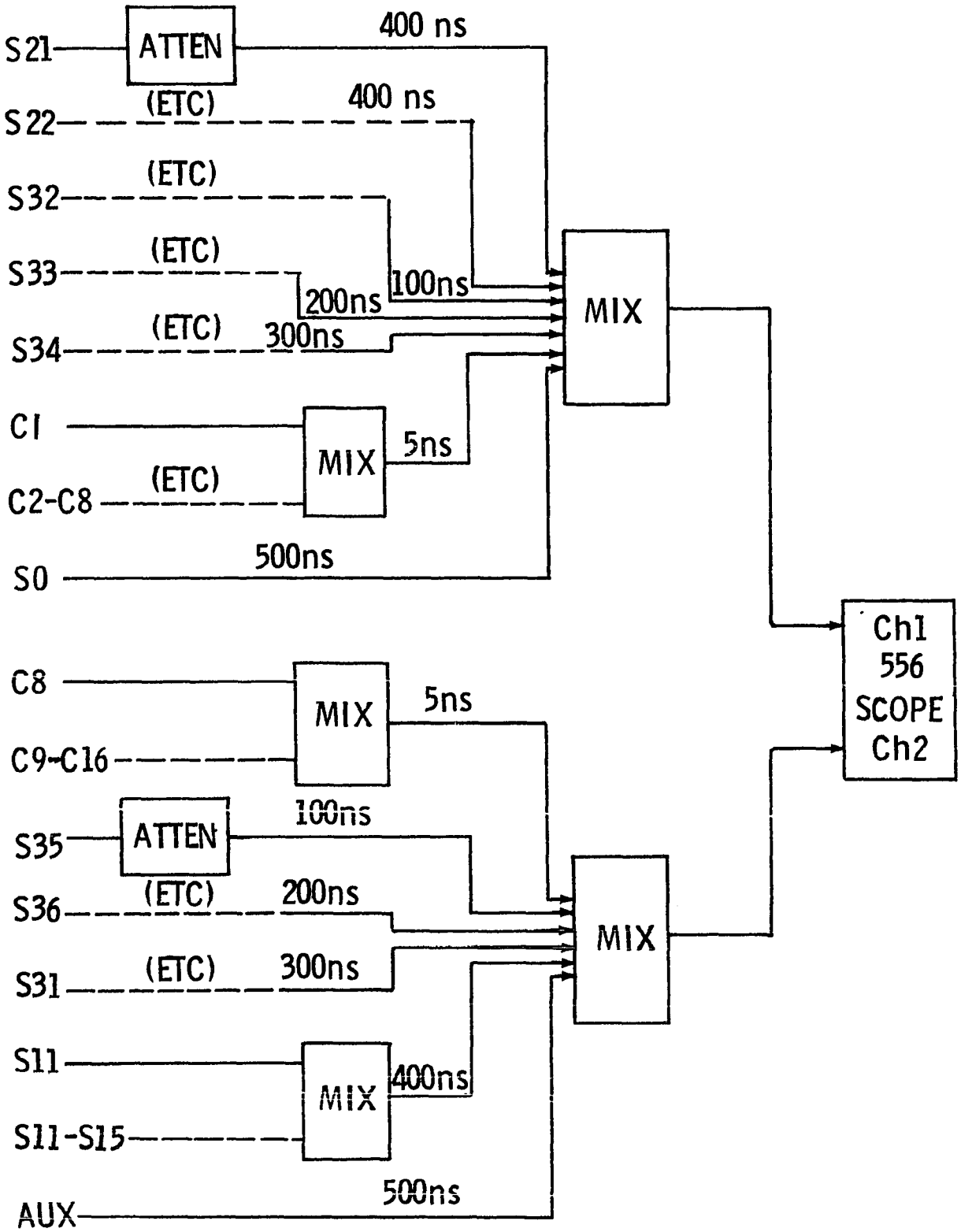

Fig. 5. Electronics for oscilloscope display of detector signals

the trace. For each event, the record on film included the pulses from each detector in S3 individually, the summed pulse from the S2 photomultipliers, the summed pulses from the S1 detectors, the Cerenkov signals summed into two pulses, and digital pulses from the AUX counter and from the S0 layer.

A typical event record is shown in Fig. 6. The figure shows the dual traces (dark) against the oscilloscope screen. Time increases from left to right, and an upwards deflection indicates positive voltage. The pulses from all detectors except S1 are negative. The pulse from each detector can be identified by its position on the trace, as indicated by arrows. Timing, pulse heights, and pulse shape can all be determined from the film record.

Since the camera shutter was too slow to operate in the time available, it was left permanently open, with logic to the oscilloscope trigger prohibiting more than one set of traces per photograph. After each event the film was automatically advanced one frame. Dead time during film advance was about three seconds, which was a negligible fraction of the running time. Data were recorded on 100 foot rolls of Tri-X 35 mm film in runs of about 1000 events each.

Test and Calibration Procedures

Calibration of the calorimeter detectors

In order to relate pulse height from the detectors to incident energy, a calibration is required. For this exper-

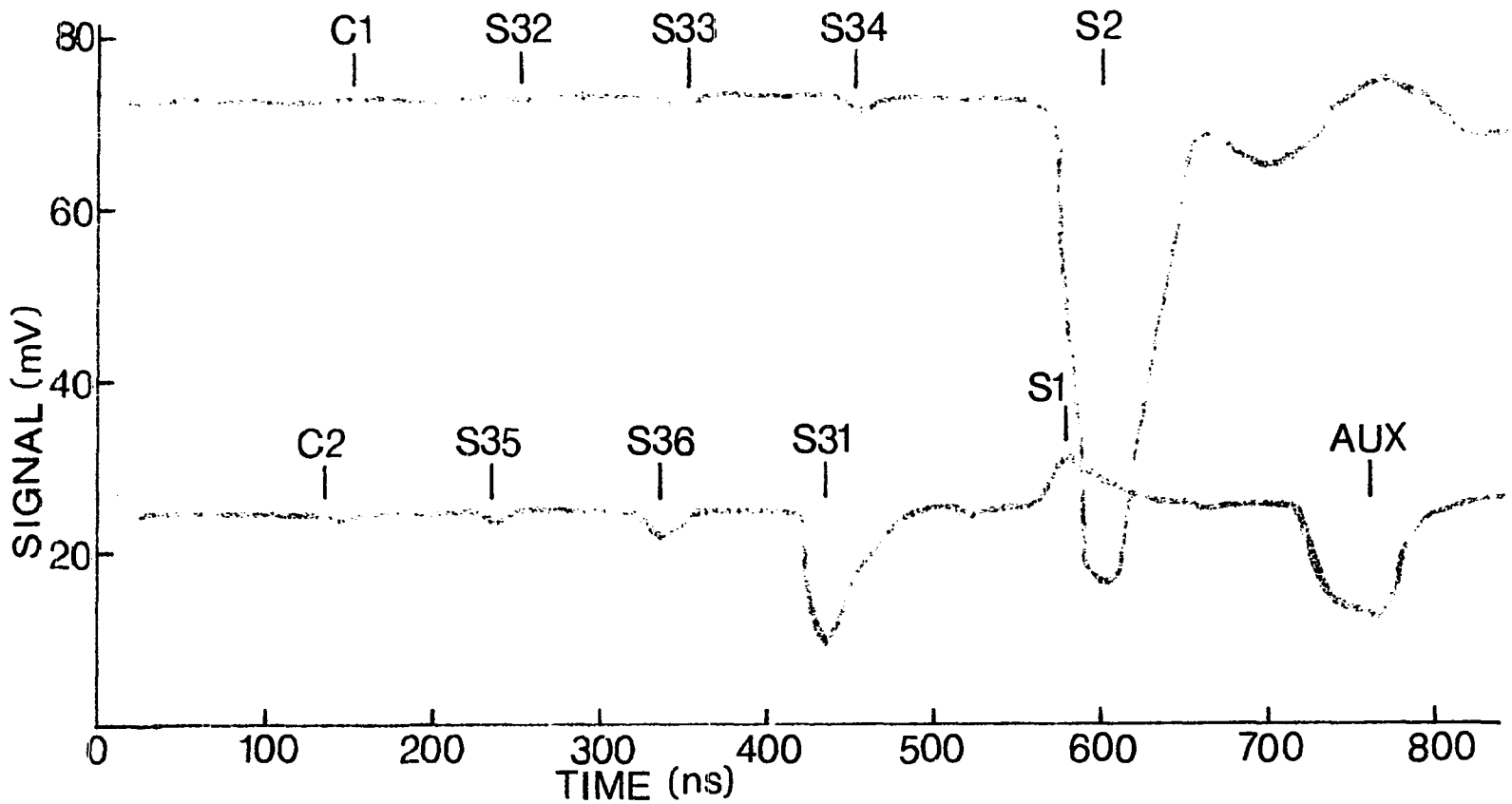

Fig. 6. Oscilloscope record of a typical event

iment a two-step process was used, in which the observed pulse heights were first converted to the cascade size traversing the detectors for each event. Calculations of cascade size as a function of incident energy were then used to convert the resulting cascade size spectrum to an incident energy spectrum. The relation between cascade size and incident energy must be calculated separately for pions, protons, and muons. These calculations are discussed in the data analysis section.

Since 10^{12} eV incident pions produced an average cascade of 2×10^3 particles traversing the scintillators in the calorimeter, it was necessary to determine the response of the photomultipliers used to large light pulses. In order to do this, a light-emitting diode (LED) was used as a calibration source. The LED was driven by a short current pulse to deliver light outputs of $\sim 3 \times 10^5$ photons in pulses of ~ 3 ns duration. The driving circuit for the LED was designed after that of McFarlane[16] with some modifications to increase the light output. The pulse was made as short as possible to simulate the light pulse from the scintillators employed. Neutral-density filters were used to reduce the light output by known factors, so that photomultiplier response over a wide range ($>10^3$) of light intensity could be determined.

The light reaching a photomultiplier from a single relativistic particle traversing its associated scintillator

was taken as a unit of intensity called the "equivalent particle" (ep). The "equivalent particle" is a useful unit because results of electromagnetic shower calculations and measurements are usually given in terms of the number of particles present in the cascade as a function of depth; it also has the advantage of being independent of scintillator thickness, efficiency of light collection, etc.

The pulse height due to single particles traversing each scintillator was determined in the following way. For S2, single particles were selected by the trigger S0·S1·S3 with the S3 threshold much less than 1 ep, and the most frequent pulse height in S2 was taken to be that caused by single particles. For S3, a similar procedure was followed except that a ^{106}Ru β-emitting source was used to provide higher counting rates, with a trigger scintillator underneath the S3 scintillator to assure that the electron passed completely through the S3 scintillator. The pulse height distributions from the detectors due to single particles are shown in Fig. 7. In all cases the single-particle peak is clear and therefore the pulse height corresponding to 1 ep is known for each detector.

The LED light source was then calibrated in ep-units and used to measure the response of the photomultipliers to large light pulses. Calibration curves of pulse height from each photomultiplier, as a function of light intensity were gen-

Fig. 7. Pulse height distributions produced by single particles traversing S2 and S3 detectors

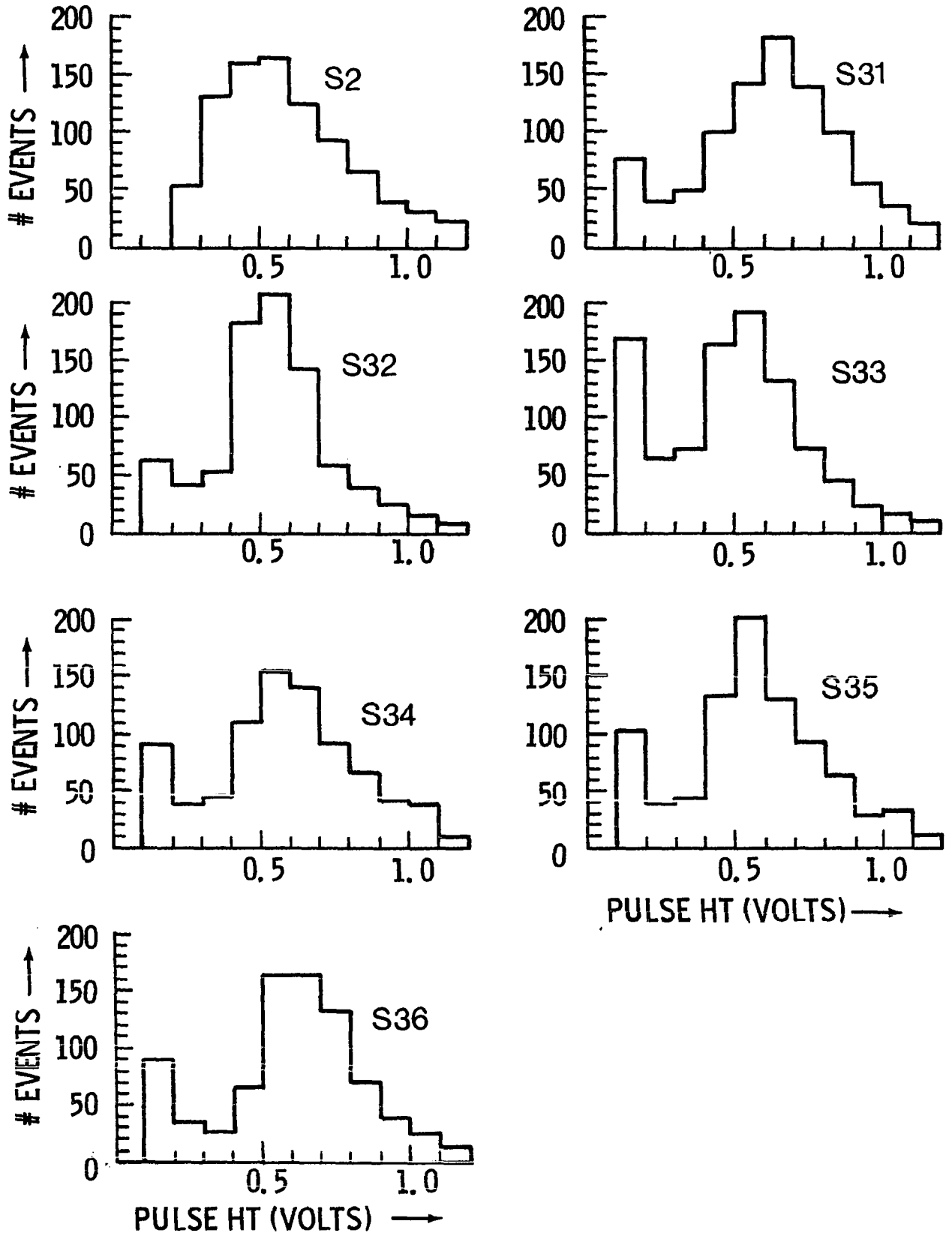
S2
S31
S32
S33
S34
S35
S36
EVENTS
PULSE HT (VOLTS)
200
150
100
50
0
0.5
1.0

erated using neutral-density filters to vary the light intensity by known factors. To make the calibration as direct as possible, the pulse height measurements were made on the 556 oscilloscope display using the same cabling arrangement as was used in the experimental runs. The results of the calibrations are shown in Figs. 8 and 9.

The neutral-density filters used in calibrating the photomultipliers were Wratten gelatin types available from Kodak. Since their attenuations were used to determine the calibration curves for the detectors, direct measurement of the filter values was desired. A test was devised in which an incandescent bulb and a yellow filter provided light near the wavelength of the LED used in calibrations, and the anode current in a photomultiplier tube was used as a measure of light intensity. The photomultiplier current was measured for various filter combinations and for various distances between the light source and photomultiplier, so that the filter attenuations could be compared to the $1/r^2$ variation of light intensity with distance over a range of 10^3 in intensity. Fig. 10 shows the result of this comparison. A least-squares fit showed the filter values to be (1.035±.016) x their nominal values. A correction factor for this was applied to the calibration curves, amounting to 12% at 4000 ep and decreasing at smaller pulse heights.

Errors in the calibration curves arise from several

Fig. 8. Calibration curves for S2 and S31-S33

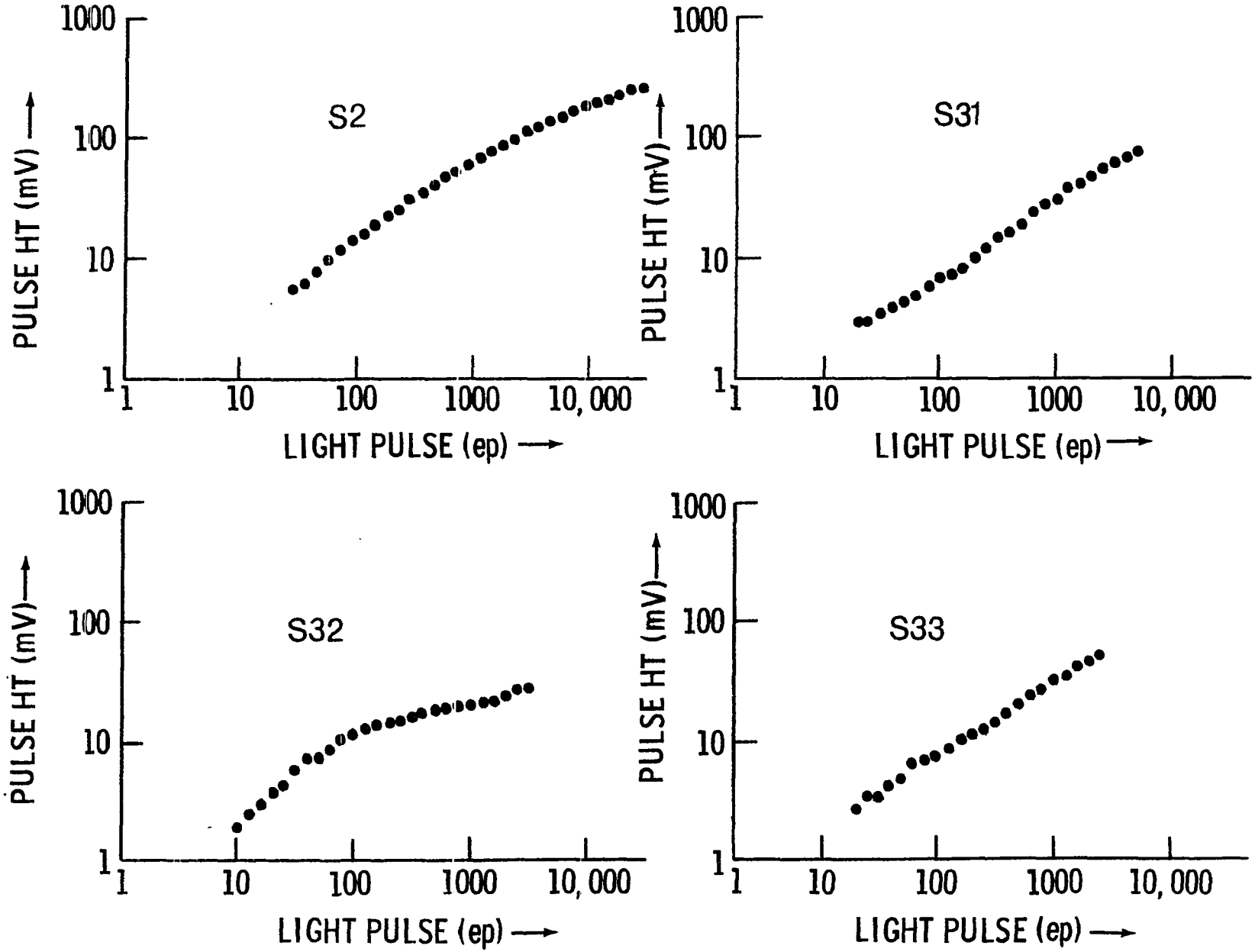
S2
S31
S32
S33
PULSE HT (mV)
LIGHT PULSE (ep)
1000
100
10
1
1
10
100
1000
10,000

Fig. 9. Calibration curves for S34-S36

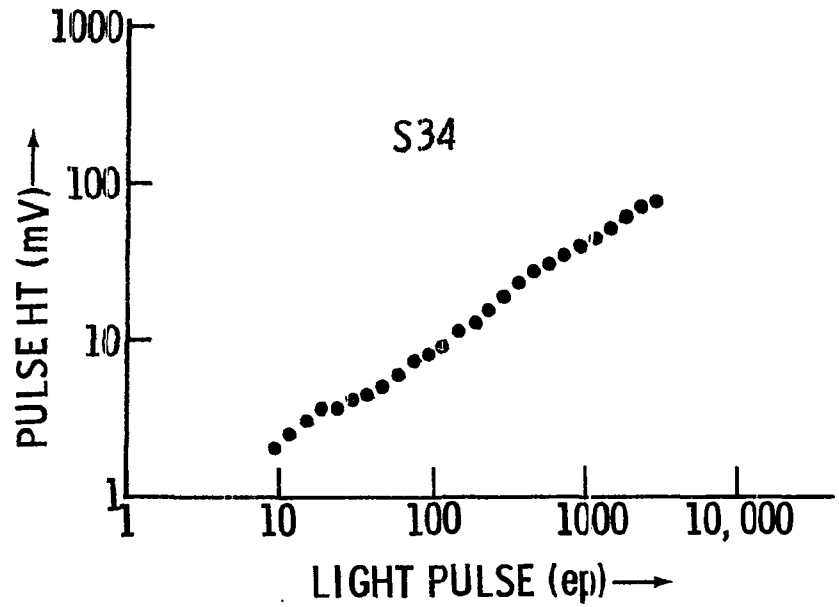
S34
PULSE HT (mV)
1000
100
10
1
1
10
100
1000
10,000
LIGHT PULSE (ep)

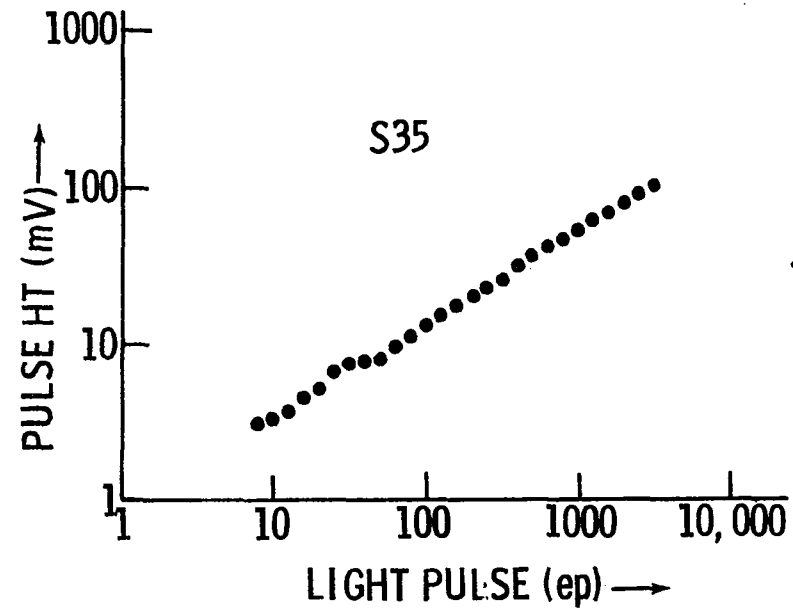
S35
PULSE HT (mV)
1000
100
10
1
1
10
100
1000
10,000
LIGHT PULSE (ep)

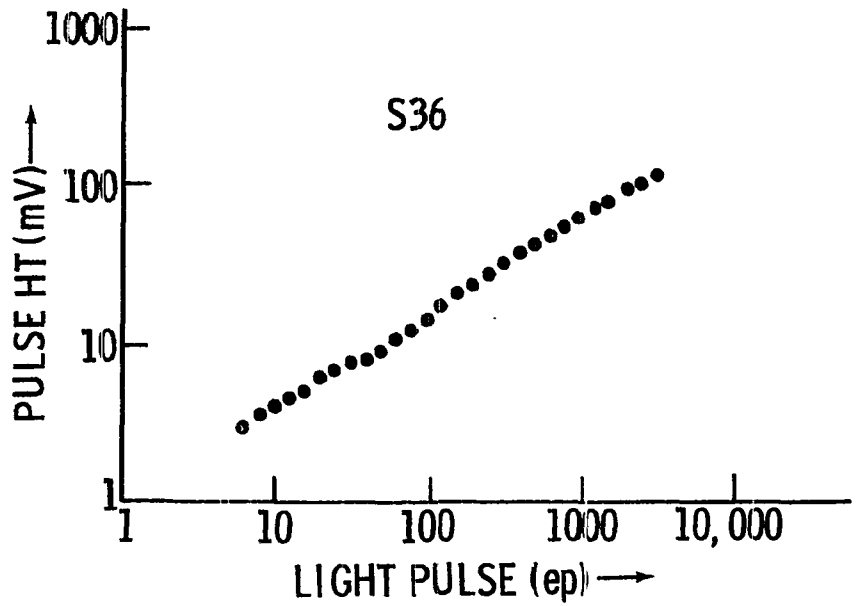
S36
PULSE HT (mV)
1000
100
10
1
1
10
100
1000
10,000
LIGHT PULSE (ep)

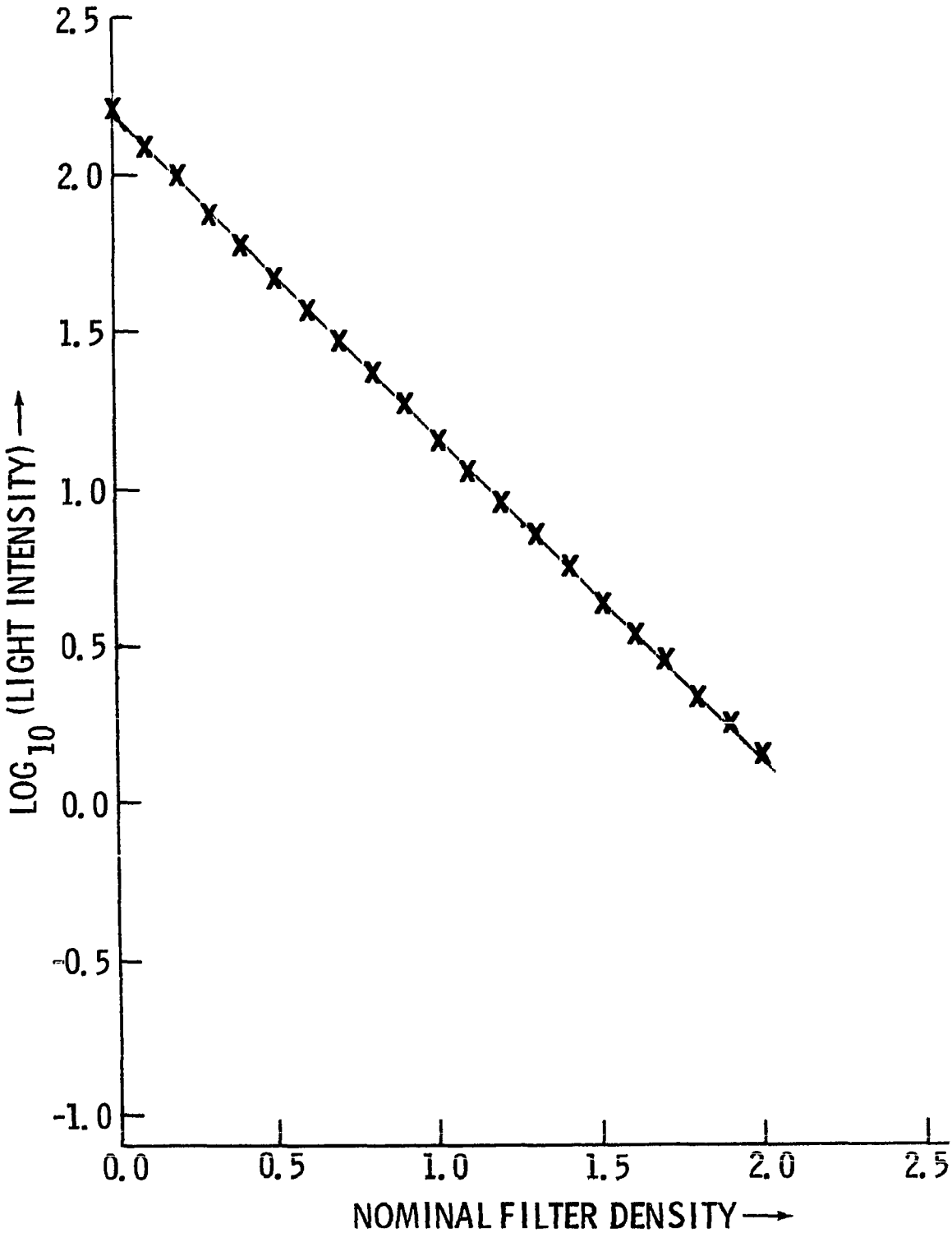

Fig. 10. Transmitted light intensity vs. nominal filter density for neutral-density filters

sources. The calibration depends directly on the measurements of pulse heights on the oscilloscope, on the values of the neutral-density filters, on the measurement of single-particle pulse heights for each detector, and on the relation between pulse height on the oscilloscope and pulse height on the measuring screen where films are scanned.

The accuracy of pulse heights measured on the oscilloscope during calibration were limited by the visual accuracy of ± 0.05 cm. on the scope screen and by the reproducibility - ± 13% - of the measurements. For low light intensities, the photomultiplier pulses showed some spread in height on the oscilloscope, as expected from statistical fluctuations in the number of photons detected per pulse. This reduced the accuracy to varying degrees; the fluctuations were most critical in comparing pulse heights from the LED source to those produced by single relativistic particles. The measurement of pulse heights from single particles also contributed to the error in the comparison.

The single-particle levels for the S2 and S3 layers were taken from the distributions shown in Fig. 7. The uncertainty in locating the center of each distribution was about 15%. There was also about a 15% error in calibrating the LED source, so that a total error of ±20% is present in the cascade size scale for each scintillator. This error would result in a systematic overestimation or underestima-

tion of cascade sizes as determined by the calorimeter.

The pulse heights for each event were measured on a scanning screen of unknown magnification. Rather than calculate the magnification from image and object distances for the optics, the scale illumination marks on the oscilloscope screen were used to make a direct determination. The scale illumination was visible on the scanning screen for many events and the spacing between divisions was simply measured with the same millimeter ruler used for measuring pulse heights. One division on the oscilloscope (1 cm) was thus found to measure 32.0±0.5 mm on the scanning screen. No variation of this value was found with position on the oscilloscope, and no variation between runs was noted.

In conclusion, the calibration curves in Figs. 8 and 9 give the best estimate of the relation between the number of particles traversing the scintillators and the pulse heights produced by the detectors. The dominant error due to calibration seems to lie in the measurement of pulse heights due to single particles. The effect of this error is an overall uncertainty of ± 20% in the cascade size scale.

Tests of the Cerenkov counter

A major concern throughout the experiment was the reliability of the Cerenkov counter, since to be useful in identifying massive particles it would have to detect the

Cerenkov light produced by protons and pions, which account for the majority of all events. It was estimated that for an air filling, the Cerenkov counter would produce 80 photons, giving rise to about 15 photoelectrons.

The ability to detect pulses of this size or smaller was tested using a ^{106}Ru source of electrons to produce Cerenkov light in a 0.3 cm thickness of plexiglas; this arrangement produced about 80 photons for $\beta=1$ particles. The photons were detected by a photomultiplier in a laboratory dark box. The pulses from the photomultiplier for this arrangement were easily detected and were well above background.

The Cerenkov counter was subjected to several further tests to determine its absolute efficiency. As a preliminary check, the efficiency of light collection was determined for the light buckets.

A typical map of light collection efficiency as a function of position is shown in Fig. 11. (The efficiency is normalized to 100% for incidence on the photocathode). The mapping square size is roughly the size of the Cerenkov light cone for $\beta=1$ particles. None of the efficiencies is low enough to prevent detection of particles with $\beta=1$.

Another test was devised in which events due to incident electrons were selected and the fraction of these events having Cerenkov signals was measured. The lead shielding and cement target were removed for this test, and the S1

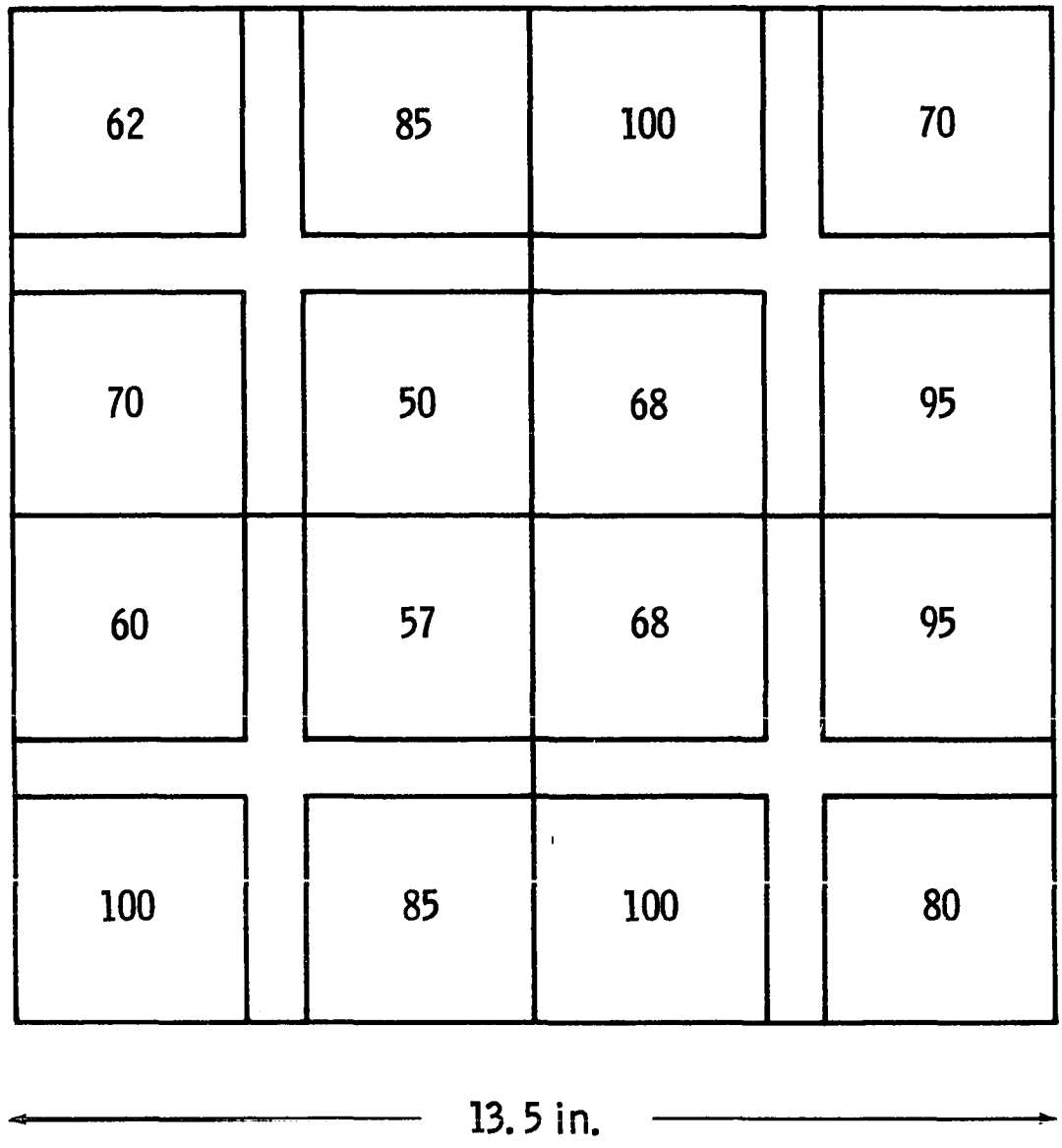

Fig. 11. Light collection efficiency map of a light bucket in the Cerenkov counter

detectors were placed directly above the layer of lead overlying S2. Incident electrons were selected by requiring triggers in S0 and S1, a pulse of at least 5 ep in S2, and no pulse in S3. Events with signals in S3 could be caused by muons and were thus rejected. The Cerenkov counter showed signals for only 55±3% of the events satisfying these requirements. However, this test is not conclusive; some of the events are caused by particles outside the Cerenkov counter's acceptance, as discussed in the section on data analysis.

DATA AND DATA ANALYSIS

Construction of the apparatus was completed during the period June 1975-November 1976. The initial experimental arrangement did not include the shielding lead above S1 or the AUX detector array. Operation of the apparatus was alternated with periods of data analysis from December 1976 to July 1978. Runs 1-3, taken in January and February 1977, were used as a preliminary tune-up period. A number of electronic failures were corrected, and the logic was also modified to reject air shower events. Data for Runs 4 and 5, taken in March and April of 1977, were used to gain statistics on events at high energy. In analyzing these runs, it was found that the Cerenkov counter gave signals for only 65% of the events, instead of the expected 100% at high energy. Thorough tests of the Cerenkov counter were performed, some problems with the electronics were corrected, and Runs 6-8 were recorded in August-October 1977. When these runs also showed the Cerenkov efficiency to be low, a physical cause was suspected. The AUX counters were then added to investigate the effects of accompanying particles on the Cerenkov efficiency. Runs 9-12, in April-May 1978, were used in this investigation. Finally, in June 1978, the lead shielding over S1 was added. The lead removed events caused by incident electrons, which were found to account for about half the event rate in earlier runs. Runs 13-16, which occurred in June-July 1978, were thus the only

Table 1. Summary of Runs

Run Number	Threshold	Triggering Logic	Running Time	Total Exposure	Number Events
13	20 ep	S0•S1•(S2+S3)	74.3 hr	1.71×10^8 cm^2-sr-s	499
14	50 ep	S0•S1•(S2+S3)	183.5 hr	4.23×10^8 cm^2-sr-s	644
15	100 ep	S1•(S2+S3)	72 hr	1.93×10^9 cm^2-sr-s	757
16	200 ep	S1•(S2+S3)	284 hr	7.63×10^9 cm^2-sr-s	1508

runs used to determine the hadron spectrum. Table 1 gives a summary of Runs 13-16.

Data Recording Procedures

For each run, data were recorded by photographing the oscilloscope traces from each event on a single roll of film. During the runs, operation was checked at least once per day to minimize data lost due to equipment failures. More complete checks of all detectors were performed between runs.

The daily procedure included recording the number of events registered on the scaler, any abnormal conditions found during the check, and the time of check in a log book. The checks were labeled "check #1", "check #2", etc. and a template was photographed to mark the film thusly at each check. In this way, if an equipment failure occurred between check #1 and check #2, for example, all frames of film between those two labels could be disregarded. The high voltage supplies and logic bin voltages were measured and readjusted, if necessary, at each check. Count rates for S0, S1, and S0•S1 were measured and recorded, and the oscilloscope traces were viewed (for S0•S1 trigger) to assure that the traces were clean and all signals were present. The camera's operation and triggering were also checked in advancing the film after photographing the template.

Checks between runs were directed toward discovering

less obvious failures of individual detectors. The high voltage supplied to each photomultiplier was measured and recorded, and noise rates for all photomultipliers were recorded. The signals displayed on the oscilloscope were all viewed individually to ensure that they arrived at the right positions and had reasonable pulse shapes. A pulsed LED source was also used to check the gain of each photomultiplier in the Cerenkov counter.

Preliminary Data Reduction

After the end of each run, the film was developed and mounted on the scanning machine where pulse heights were measured. For each event, timing of all pulses was checked and the pulse height from each detector was measured in millimeters on the scanning screen and recorded in a data book. The data were then put on punch cards and read into computer disk files for analysis. Running time for each run was calculated from the log book records.

Less than 5% of the events were rejected due to poor photographic quality. No noise on the oscilloscope traces was visible, and pulses were measured to within ±.5mm on the measuring screen, which corresponded to ±.3mV on the oscilloscope. Pulses were occasionally too large to be measured; the oscilloscope beam, moving more rapidly to cover larger pulses, did not leave enough light intensity for the

tops of some pulses to be seen on the film. This problem was most frequent with the Cerenkov signals and with S1, for which the pulse height was not particularly important. For a few events, S3 or S2 pulses were too large to measure, and lower limits on the pulse height were used in these cases. Pulses more than 30 ns from the expected positions were rejected.

Data analysis was done using a PDP 11/45 computer. The calibration curves for the S2 and S3 detectors were entered as an array. A subroutine was used to read event records from disk and convert pulse heights for the detectors to cascade size in ep using the calibration curves. Histograms of cascade size for the S2 and S3 detectors and of pulse heights for S1 and C were made. The cascade sizes from all S3 detectors were added together for each event and histogrammed, and the sum of the cascade sizes in S2 and S3 was also histogrammed. Events with or without signals from S0, AUX, or the Cerenkov counter could be selected separately for analysis.

For brevity in the following sections, pulse height in the various detectors are referred to by simply naming the detectors. For example, the cascade size in equivalent particles in detector S2 is simply written "S2" and the expression "S2+S3" means "the sum of the cascade size in detector S2 and the cascade size in all S3 detectors".

Preliminary Analysis of Results

The total cascade size S2+S3 is proportional to the energy of the electromagnetic cascade. The energy of the cascade, in turn, is roughly proportional to the incident particle's energy. Thus the cascade size spectrum is expected to be similar to the energy spectrum of incident particles. Figs. 12 and 13 show the raw differential spectra of cascade size, dN/d(S2+S3) vs. S2+S3 for Runs 13-16. To set the scale, a cascade energy of 100 GeV corresponds to S2+S3 = 1500 ep. The errors shown are statistical only. The spectra all fall as power laws with $dN/d(S2+S3) \sim (S2+S3)^{-2.7}$ for large cascade size.

For small cascade size the triggering thresholds cause artificial falloffs. The thresholds' effects are seen over a somewhat wider range than one might expect because of the nonlinear response of the S3 photomultipliers which increases the response to a cascade distributed over two detectors, relative to the response to a cascade which falls on one detector.

Figs. 14 and 15 show pulse height histograms for S1 and for the Cerenkov counter. The horizontal scale here is millimeters on the measuring screen. Clear peaks mark the pulse heights due to single particles passing through the detectors. For the S1 histogram it is clear that most events

Fig. 12. Raw differential spectra of S2+S3 for Runs 13 and 14

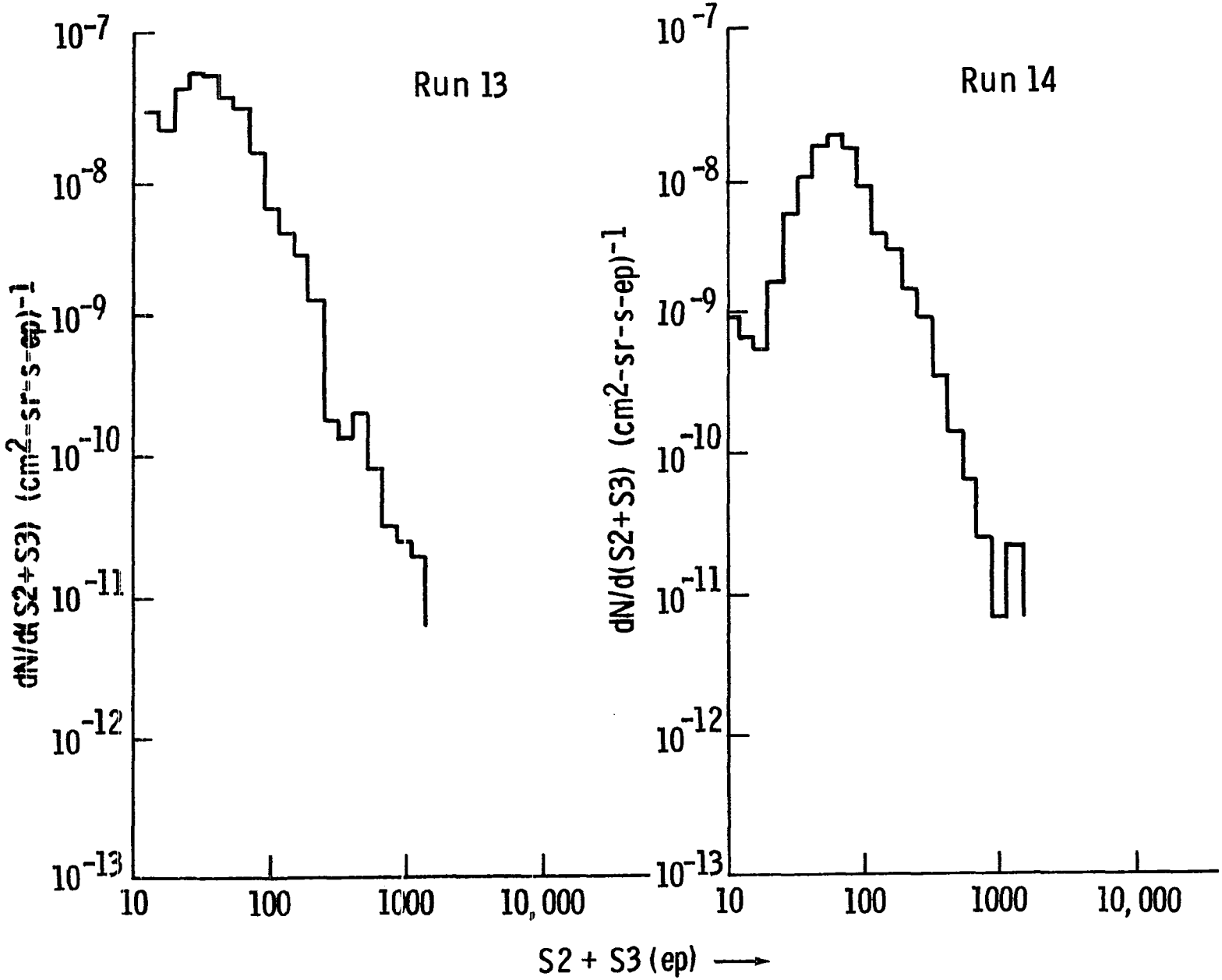
Run 13
Run 14
10^{-7}
10^{-8}
10^{-9}
10^{-10}
10^{-11}
10^{-12}
10^{-13}
dN/d(S2+S3) (cm²-sr-s-ep)⁻¹
10
100
1000
10,000
S2 + S3 (ep) ⟶

Fig. 13. Raw differential spectra of S2+S3 for Runs 15 and 16

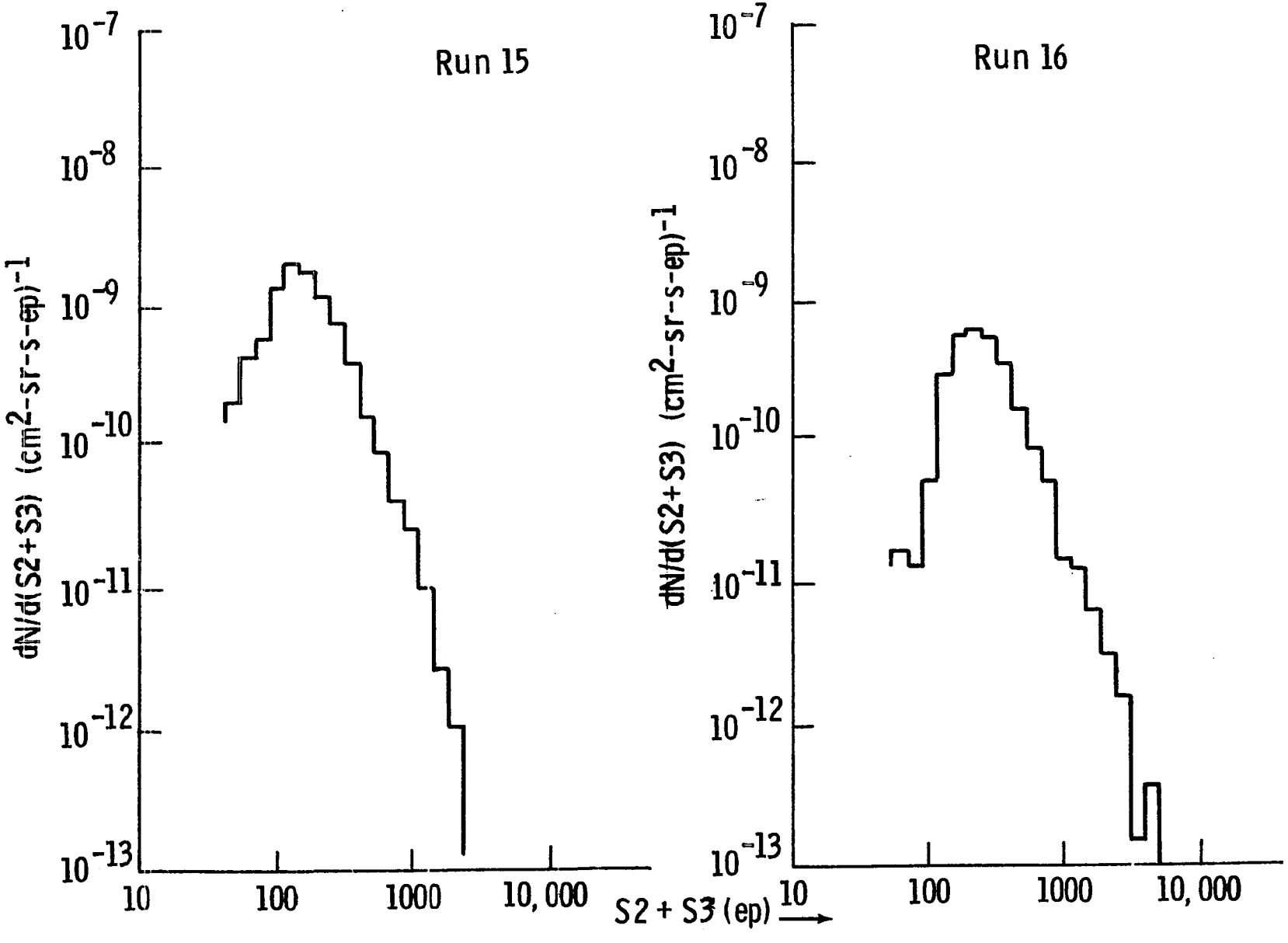
Run 15
Run 16
10^{-7}
10^{-8}
10^{-9}
10^{-10}
10^{-11}
10^{-12}
10^{-13}
dN/d(S2+S3) (cm^2-sr-s-ep)$^{-1}$
10
100
1000
10,000
S2 + S3 (ep)

Fig. 14. Histogram of pulse heights from the S1 detectors - all events Runs 13-16

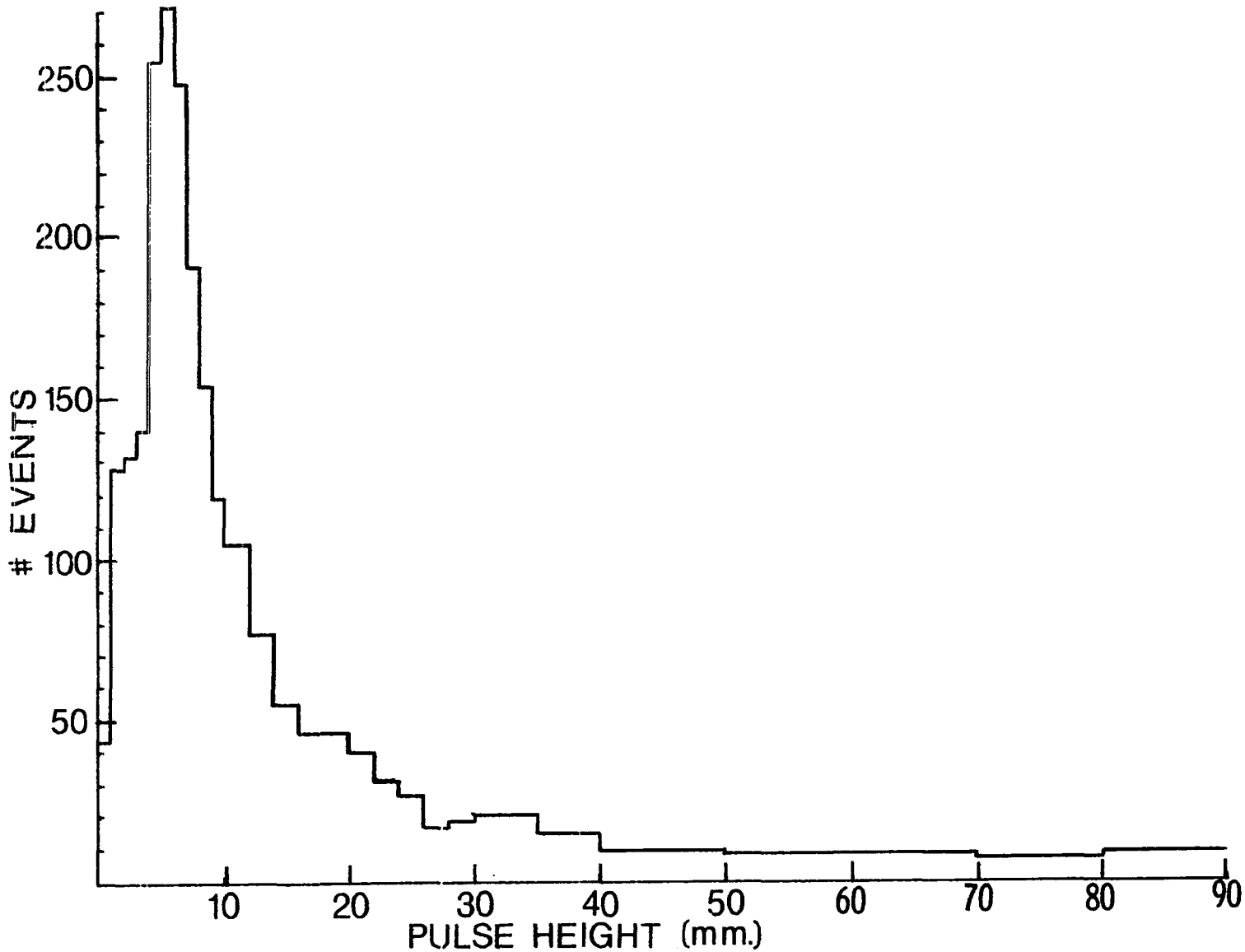
250
200
150
100
50
EVENTS
10
20
30
40
50
60
70
80
90
PULSE HEIGHT (mm.)

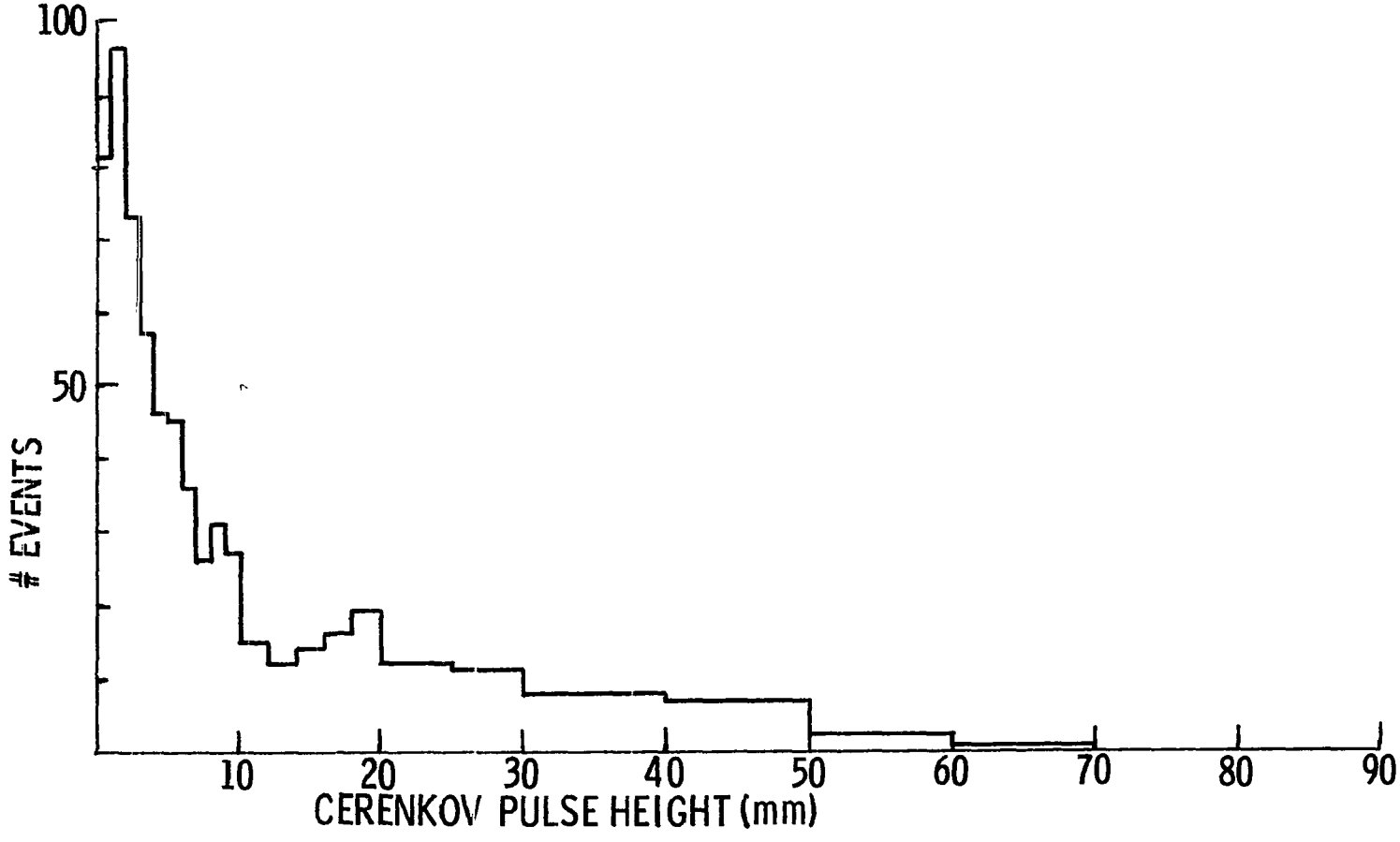

Fig. 15. Histogram of pulse heights from the Cerenkov counter - all events Runs 13-16

Table 2. Power-law fits to spectra of Runs 13-16

Fitted to form: $dN/d(S2+S3) = A\left(\frac{S2+S3}{300\ ep}\right)^{-B}$ $(cm^2-sr-s-ep)^{-1}$

Run Number	A	B
13	$4.4^{+3.4}_{-1.9}x10^{-10}$	2.54±.12
14	$5.5^{+6.9}_{-3.0}x10^{-10}$	2.44±.15
15	$5.3^{+4.8}_{-2.5}x10^{-10}$	2.69±.11
16	$4.6^{+3.5}_{-2.0}x10^{-10}$	2.76±.09

are caused by single particles. The histogram also shows a number of events with large S1 pulse heights, some of which are due to multiple incident particles and some of which are due to single particles which create electromagnetic cascades in the shielding lead. Events with S1 > 30 mm were rejected as being due to interactions in the shielding lead above S1. The Cerenkov signals show a peak above zero, indicating that few signals are lost due to low pulse height.

Individual pulse height histograms for each detector in S3 for Run 16 are shown in Fig. 16. Since cascades often struck two or more detectors in S3, there is no clear significance to their individual spectra; however, these histograms serve as a check on the analysis and on the performance of the detectors during the runs. If a detector failed or if a large error were present in the calibration curves, the counting rates for that detector would be too high or too low. This check was performed for each run.

For convenience in comparing the four runs, the (S2+S3) spectra were calculated in units of events/cm^2-sr-s-ep. The data were histogrammed in logarithmic bins of width $e^{0.25}$, and a straight line fit was determined for each spectrum. The data below S2+S3 = 54, 115, 190, and 314 ep. for Runs 13, 14, 15, and 16 respectively were ignored because of threshold effects. The results of the fits are shown in Table 2. The errors shown are for counting statistics only. The runs were

Fig. 16. Histogram of pulse heights from individual S3 detectors for Run 16

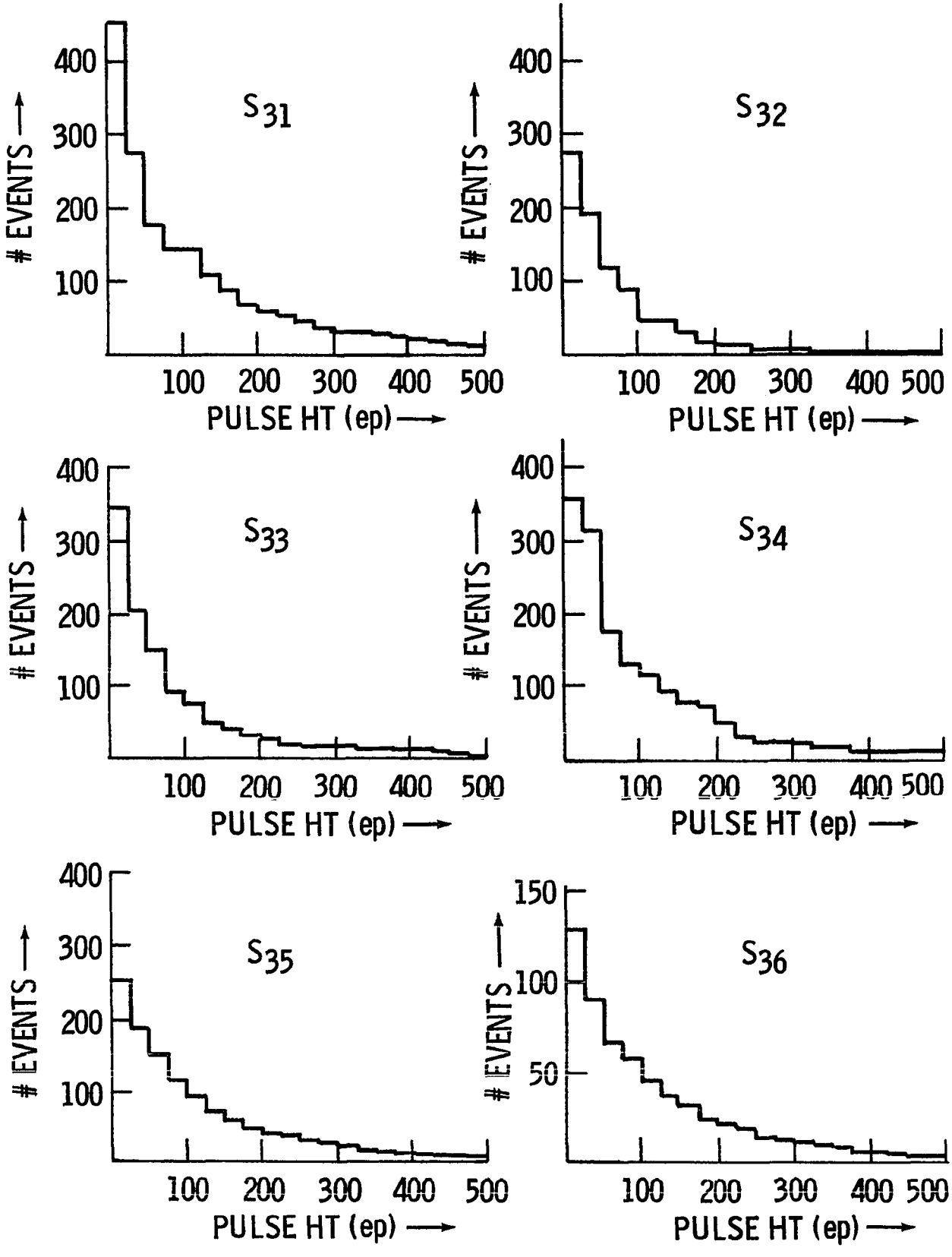
S31
S32
S33
S34
S35
S36
EVENTS
PULSE HT (ep)
100
200
300
400
500
50
150

then combined, for the runs above threshold in each bin, to form the spectrum of Fig. 17. This spectrum was fitted, with the result

$$\frac{dN}{d(S2+S3)} = (6.68\pm1.7)\times10^{-9}\left(\frac{S2+S3}{100ep}\right)^{-2.59\pm.04}$$

$$(cm^2\text{-}sr\text{-}s\text{-}ep)^{-1}$$

From the cascade curves of Müller[17], it is possible to predict the ratio of pulse heights in the two layers, S2/(S2+S3), as a function of total cascade size (S2+S3). Fluctuations in the ratio can be expected due to variation in the depth at which incident particles interact and due to statistical fluctuations in cascade development, but the average ratio can be predicted in this way. Fig. 18 shows the predicted behavior of S2/(S2+S3) for incident hadrons and the average ratio for all events in Runs 13-16. There is good agreement with the prediction over the full range of pulse heights considered. The prediction is an absolute one derived from the cascade curves of Müller and the hadron interaction characteristics described in the next section with no adjustable parameters. A calculation of χ^2 for a fit of the data to the prediction for hadrons was made, giving $\chi 2 = 17.7$ for 8 degrees of freedom. The probability that the observed distribution arose from the predicted curve is $\sim 3\%$, which, for an absolute prediction, appears to be adequate.

For comparison, the predicted S2/(S2+S3) for incident

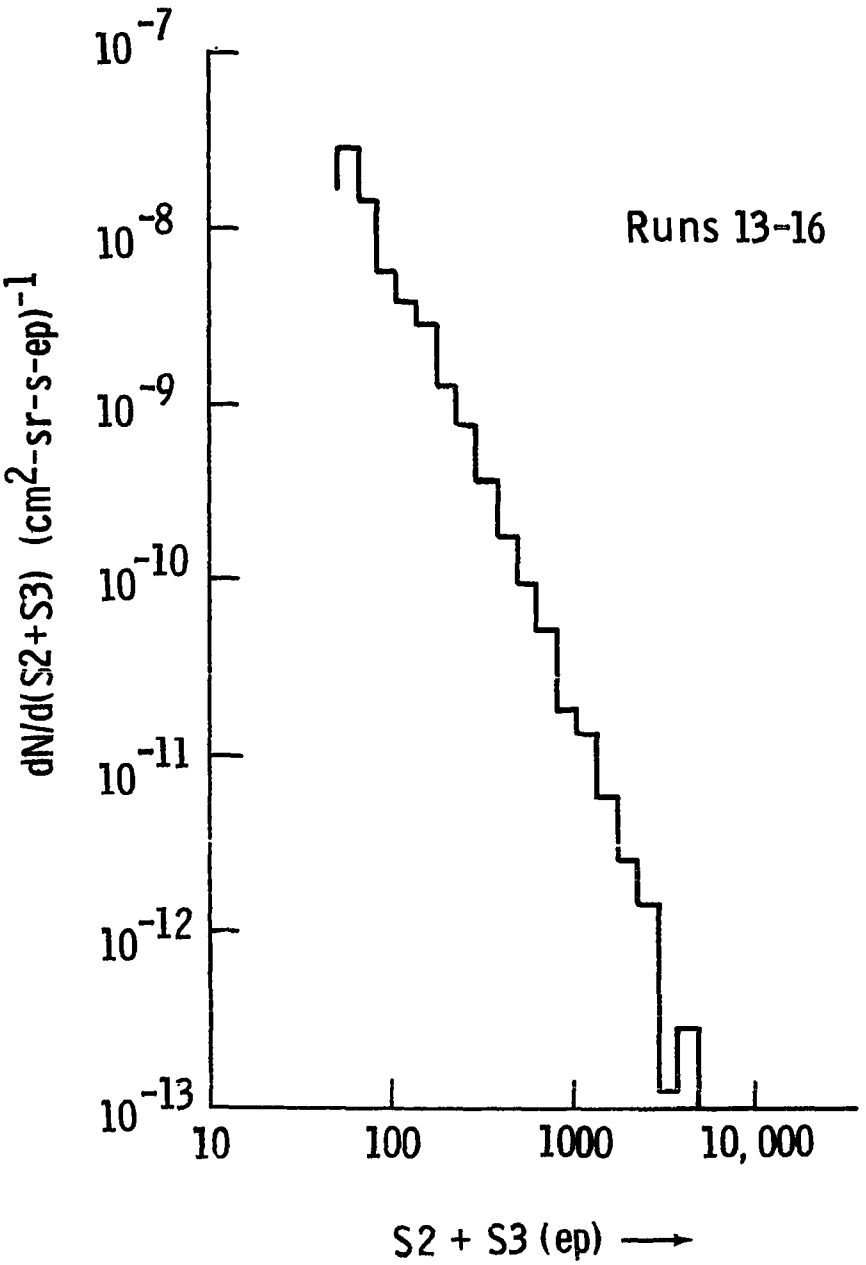

Fig. 17. Combined spectrum of S2+S3 pulse heights - Runs 13-16

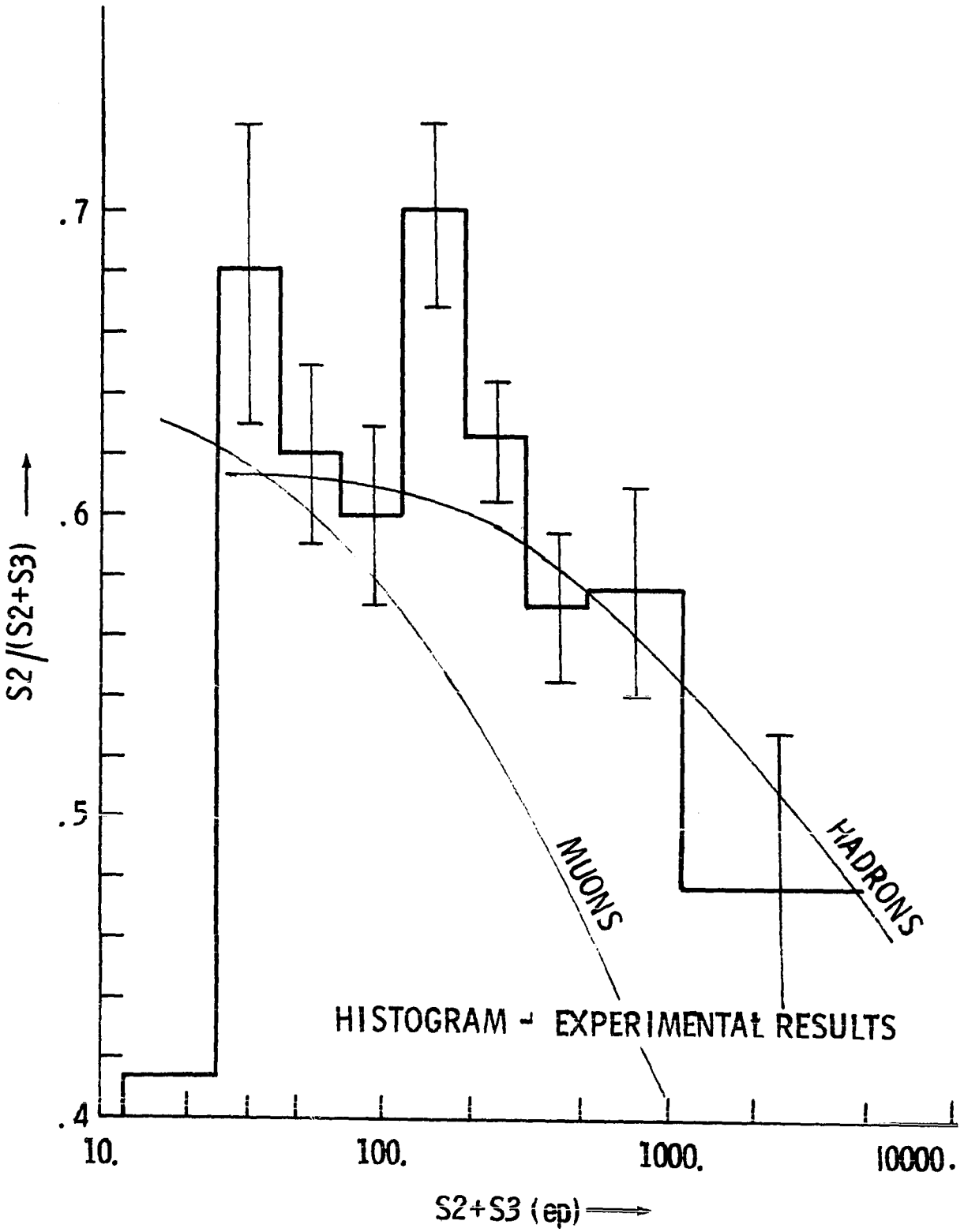

Fig. 18. Ratio of pulse heights (S2/S2+S3) vs. S2+S3

muons is also shown in Fig. 18. While the curve for muons provides a satisfactory fit to the data below 100 ep, it is obviously incompatible at larger pulse heights. The value of χ^2 calculated for a fit to the predicted curve for muons is 96.4 for 8 degrees of freedom, giving a relative likelihood of $\sim 10^{15}$ that the observed distribution arises from a hadron rather than a muon parentage. This is a strong confirmation that most of the events at S2+S3 > 100 ep are caused by hadrons.

Deriving the Hadron Spectrum

Further analysis of the data requires the separate consideration of cascades due to various incident species. Incident electrons may be ignored, since the combined effects of the shielding lead and the requirement that S1 pulses be small eliminates events due to electrons. The observed events may be assumed to be caused by muons, pions, and protons. These three particles interact differently with the calorimeter, and separate calculations of the calorimeter response for each must be made.

Pion and proton interactions have been widely studied at accelerators over the energy range of interest here (10^{10}-10^{12} eV) and therefore their cascades in the calorimeter may be calculated with some confidence. In a typical interaction, an average of about one-third of the pions pro-

duced are π^0's which decay to γ-rays, forming electromagnetic cascades. The subsequent interactions of hadrons emerging from the interaction may be ignored, as a first approximation, since the target is only about one interaction length thick. The average energy transferred to the cascade may be estimated using available data on hadron interactions. The electromagnetic cascade curves of Müller[17] can then be used to calculate the cascade size in S2 and S3.

The simulations of hadron interactions described in Appendix II give a good approximation of cascade size as a function of incident energy for both pions and protons. However, a simple, direct calculation of <S2+S3> vs. incident energy was desired to provide a check of the simulation results. Good agreement was found between the two methods; the simpler calculations described here were judged to be more accurate than the simulation results, and thus were used in deriving the hadron spectrum.

The following procedure was used to calculate cascade size as a function of incident energy. Incident particles were assumed to interact at the center of the cement target. Protons were assumed to give 1/2 their energy to a leading nucleon and distribute the remainder equally among π^+, π^-, and π^0, while incident pions were assumed to distribute their energy equally among π^+, π^-, and π^0 production. Thus for protons 1/6 of the incident energy was given to the cascade,

and for pions 1/3 of the energy was given to the cascade. The number of π^0's produced was taken from the summary of Whitmore[18] to be $\langle n_{\pi^0} \rangle = -0.82+0.79 \ln(\text{Plab})$, with Plab in GeV, for both pions and protons. Each π^0 was assumed to decay to two γ rays and each γ ray to transfer its energy to an electron-positron pair at a depth 1 r.l. below the initial interaction, so that the cascade energy was shared equally among $4\langle n_{\pi^0} \rangle$ electrons.

The size of the cascade produced by these electrons at the depths of S2 and S3 was calculated using the cascade curves of Müller[17]. For Runs 15 and 16, since the particles were incident at an average angle $\langle \cos\theta \rangle = 0.92$, these depths were multiplied by 1/0.92 and the cascade sizes from Müller's curves were multiplied by 1/0.92 to account for the increased path length through the detectors. Detector S2 was thick enough (5g/cm^2 or 0.1 r.l.) that not all cascade electrons near the critical energy of lead (7MeV) would traverse it.[19] A correction of 16% was applied to S2 to account for this effect at small cascade sizes. The S3 detectors were thin enough that no correction was needed for them. Fig. 19 shows cascade size as a function of the cascade initiating electron's energy as used in finding cascade size for incident hadrons.

Calculations of cascade size were made for a number of incident energies for both pions and protons, and the result-

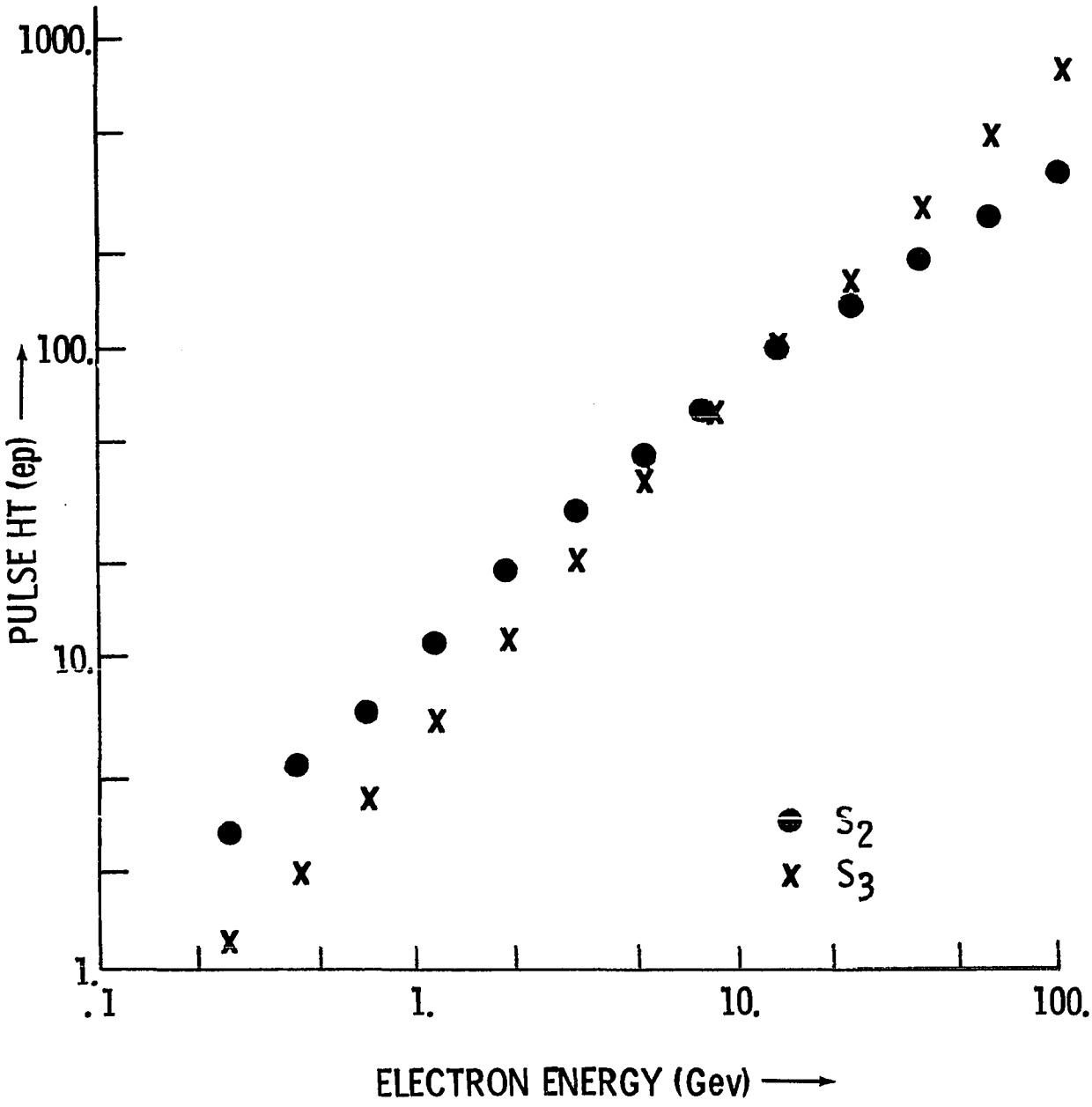

Fig. 19. Cascade size in S2 and S3 vs. energy of electron

ing relation between cascade size and incident energy is shown in Figs. 20 and 21. A correction for multiple interactions in the calorimeter has been included in these curves. There is fair agreement between this simple calculation and the results of the simulation program, as is pointed out in Appendix II; the values found for S2+S3 differ by less than 25% over the range of interest.

Several notes of caution need to be added at this point. The first is that there are errors associated with the calibration process just described. The major contribution is the error in physical calibration of the detectors, estimated to be ±20%. The approximations used in relating cascade size to incident energy also introduce an error whose magnitude is not known.

The second problem to be aware of is that there are wide fluctuations in hadron interactions from one event to the next, so that it is impossible to equate incident energy to cascade size except in the average for a large number of events. The simulation results in Appendix II show this clearly. A histogram of the fraction of energy give to π^0's, k_γ, for a large number of simulated interactions by 250 GeV pions is shown in Fig. 22. The width of this distribution is a measure of the "energy resolution" of the calorimeter.

One final note should be made regarding the effects of fluctuations in interactions on the observed spectrum. If

Fig. 20. Cascade size (S2+S3) vs. energy for vertically incident hadrons

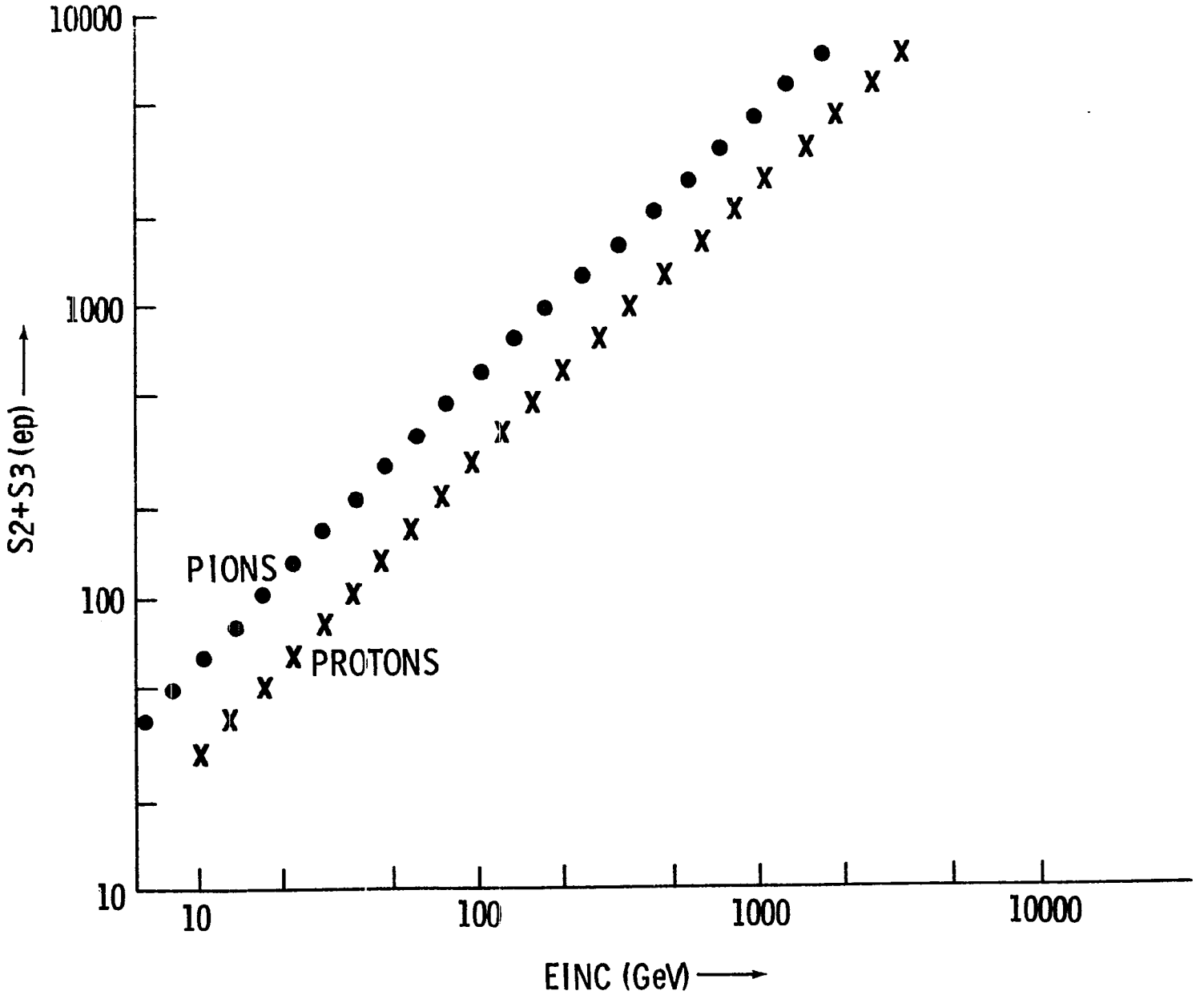
10000
1000
100
10
S2+S3 (ep)
PIONS
PROTONS
10
100
1000
10000
EINC (GeV)

Fig. 21. Cascade size (S2+S3) vs. energy for hadrons incident at $\langle\cos\theta\rangle = .92$

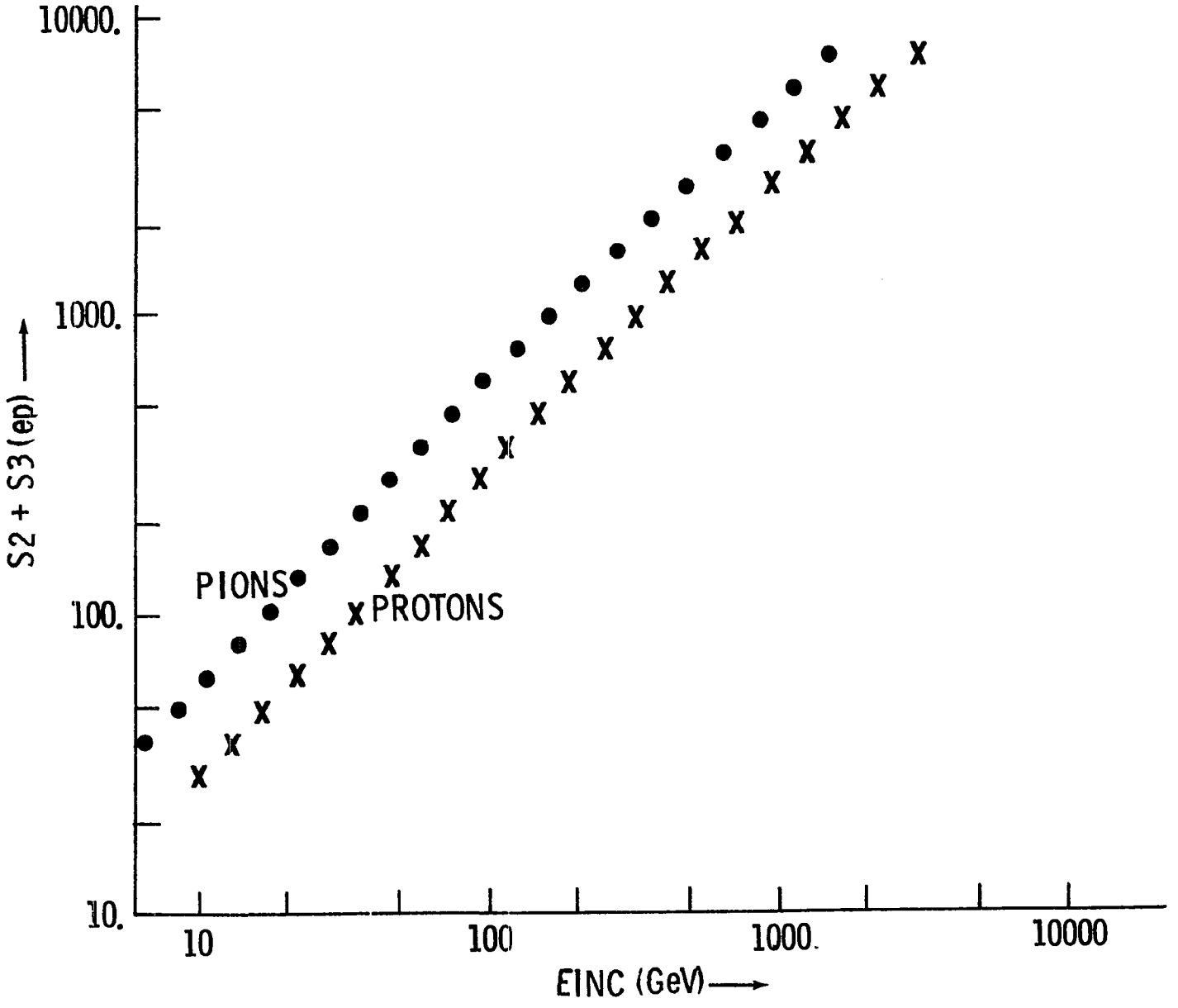
10000.
1000.
100.
10.
S2 + S3 (ep)
PIONS
PROTONS
10
100
1000.
10000
EINC (GeV)

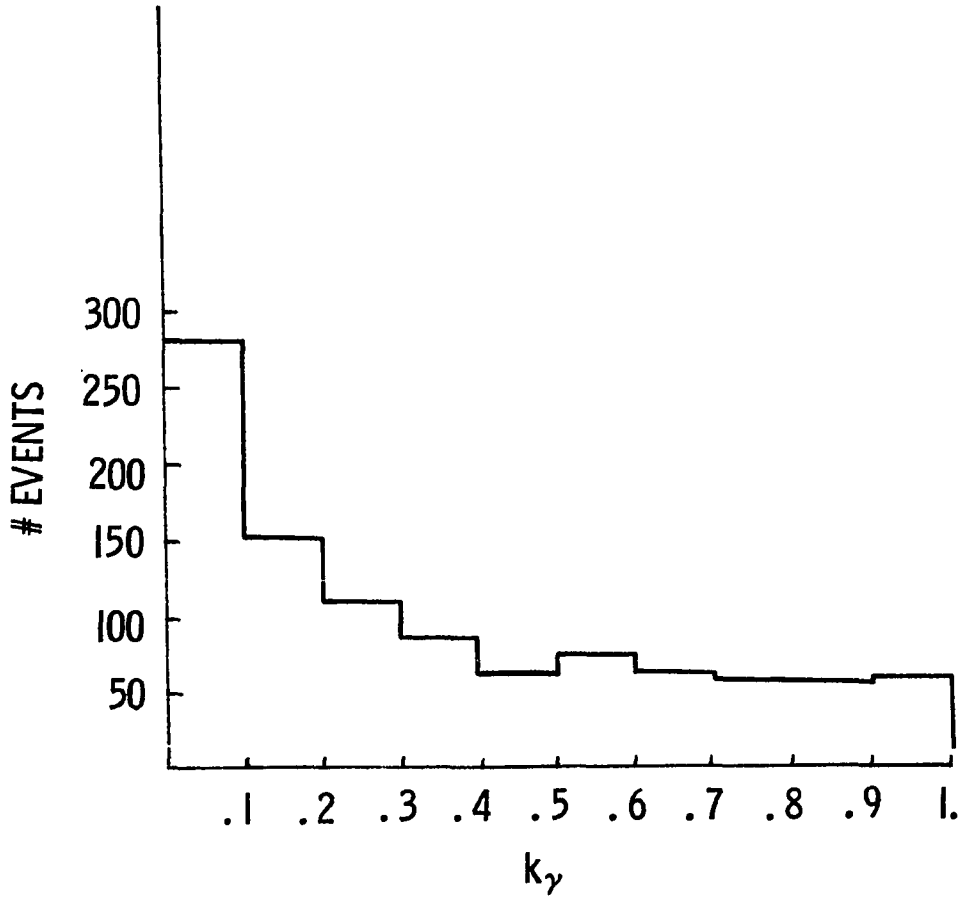

Fig. 22. Histogram of k_γ for simulated interactions of 250 GeV pions

fluctuations to greater or lesser cascade size than average occur with equal frequency, the steepness of the cascade size spectrum causes the fluctuations to greater size to be emphasized. The simulations in Appendix II indicate that this fact, if not corrected for, would cause the hadron intensity to be overestimated by a factor of about 1.6.

Corrections to the observed event rates must be made for the efficiency of the apparatus in detecting hadrons. The efficiency was calculated by assuming that hadrons interact with some characteristic attenuation length λ so that the intensity of hadrons remaining at depth x is given by $I = I_o e^{-x/\lambda}$.

Hadrons interacting above the calorimeter target are assumed to be lost; though products of the interaction could produce a cascade, it would be excluded by the large pulse height observed in S1. The roof over the calorimeter was estimated to contain 4" of cement (25.4 g/cm^2) and 2" of roofing tar (13 g/cm^2). There was 2" of lead (58 g/cm^2) in the shielding layer, and the cement target was 17" (108 g/cm^2) thick. Taking the attenuation length to be 100 g/cm^2 for cement, 80 g/cm^2 for roofing tar, and 210 g/cm^2 for lead, the fraction of incident particles which interact in the target is:

$$e^{-25.4/100} e^{-13/80} e^{-58/210} (1-e^{-108/100}) = 0.33$$

This is the estimated efficiency of the detector for inci-

dent hadrons. If event rates are systematically overestimated by a factor of 1.6 due to flucuations in the interaction process as indicated by the simulations in Appendix II, it is appropriate to use an "effective" efficiency of 1.6 x 0.33 = 0.53.

Muons can interact in the calorimeter target to produce knock-on electrons or bremsstahlung photons which form cascades. Since the study of muons was not an object of this experiment, the effects of muons had to be estimated and eliminated. To do this, a comparison of the expected event rates for muons and pions was made. This comparison is presented in Appendix I. Predicted muon and pion event rates for the apparatus are shown in Fig. 23. The comparison indicates that muon cascades contribute most of the events at small cascade size, but relatively few events at large cascade size. Because of this, events below 200 ep were not considered in determining the hadron spectrum. At 200 ep, the muon rate was estimated to be less than 40% of the total rate, and the percentage of events due to muons decreased rapidly with increasing S2+S3. Therefore muon rates were ignored in computing the hadron spectrum above 200 ep.

Cerenkov and AUX Data

By separately histogramming events with and without Cerenkov signals, it was possible to determine the percen-

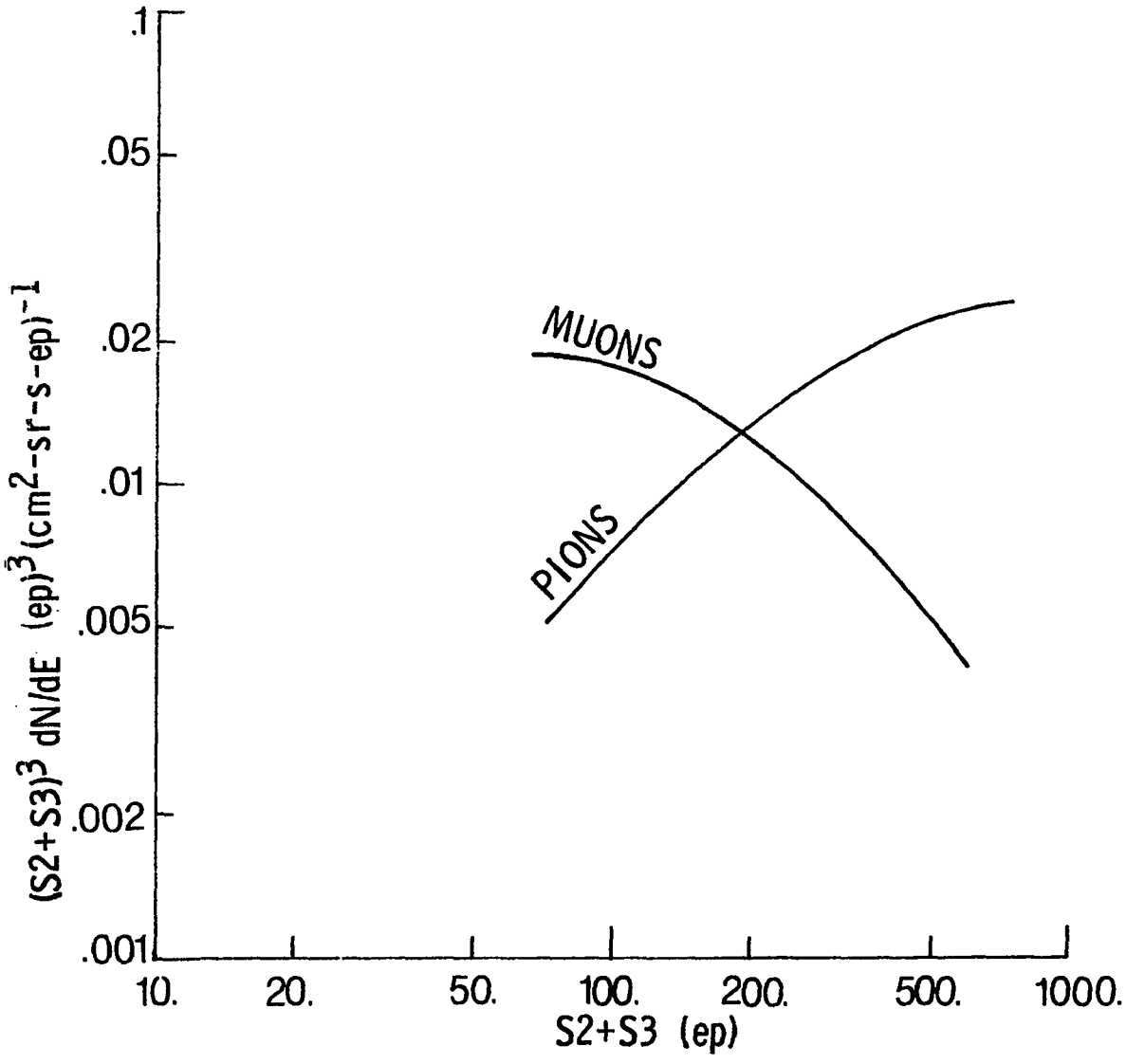

Fig. 23. Predicted event rates for muons and pions

tage of events having Cerenkov signals (%C) as a function of S2+S3. The results of this calculation are shown in Fig. 24, with statistical errors. Those events from Runs 15 and 16 in which S0 was struck have been included. One would expect particles of very low energy to be below the Cerenkov threshold and thus never to show Cerenkov signals, while all those events at large energy should be above the Cerenkov threshold. The curve is expected to rise monotonically to 100% for large cascade sizes. The proton is the heaviest hadron for which significant count rates are expected, and its Cerenkov threshold in air is 40 GeV, corresponding to a cascade size near 100 ep. Thus all events with S2+S3>100 ep should have Cerenkov signals. The failure of the curve to reach 100% indicates either that the Cerenkov counter is less than 100% efficient or that events outside the Cerenkov counter's acceptance are being observed.

Fig. 25 shows a way in which events outside the Cerenkov counter's acceptance could be mistaken for events within it. With no track determining device, the apparatus could not distinguish between legitimate events within the Cerenkov counter's acceptance (Figs. 25a and b) and events due to an accompanied particle outside the acceptance (Fig. 25c). The latter class of events would produce no Cerenkov signals.

The AUX counters provide information on accompanying

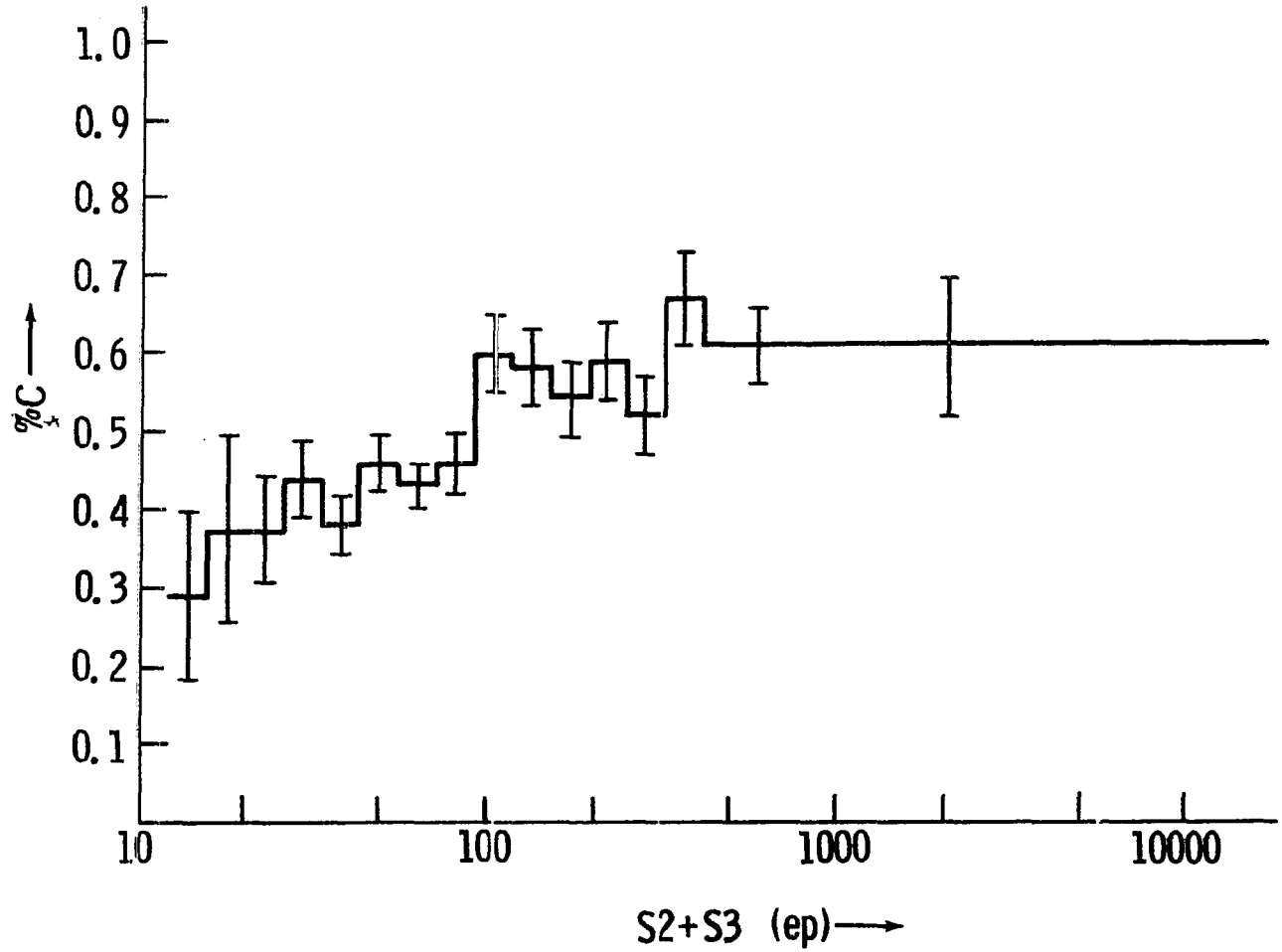

Fig. 24. Fraction of events having Cerenkov signals vs. S2+S3

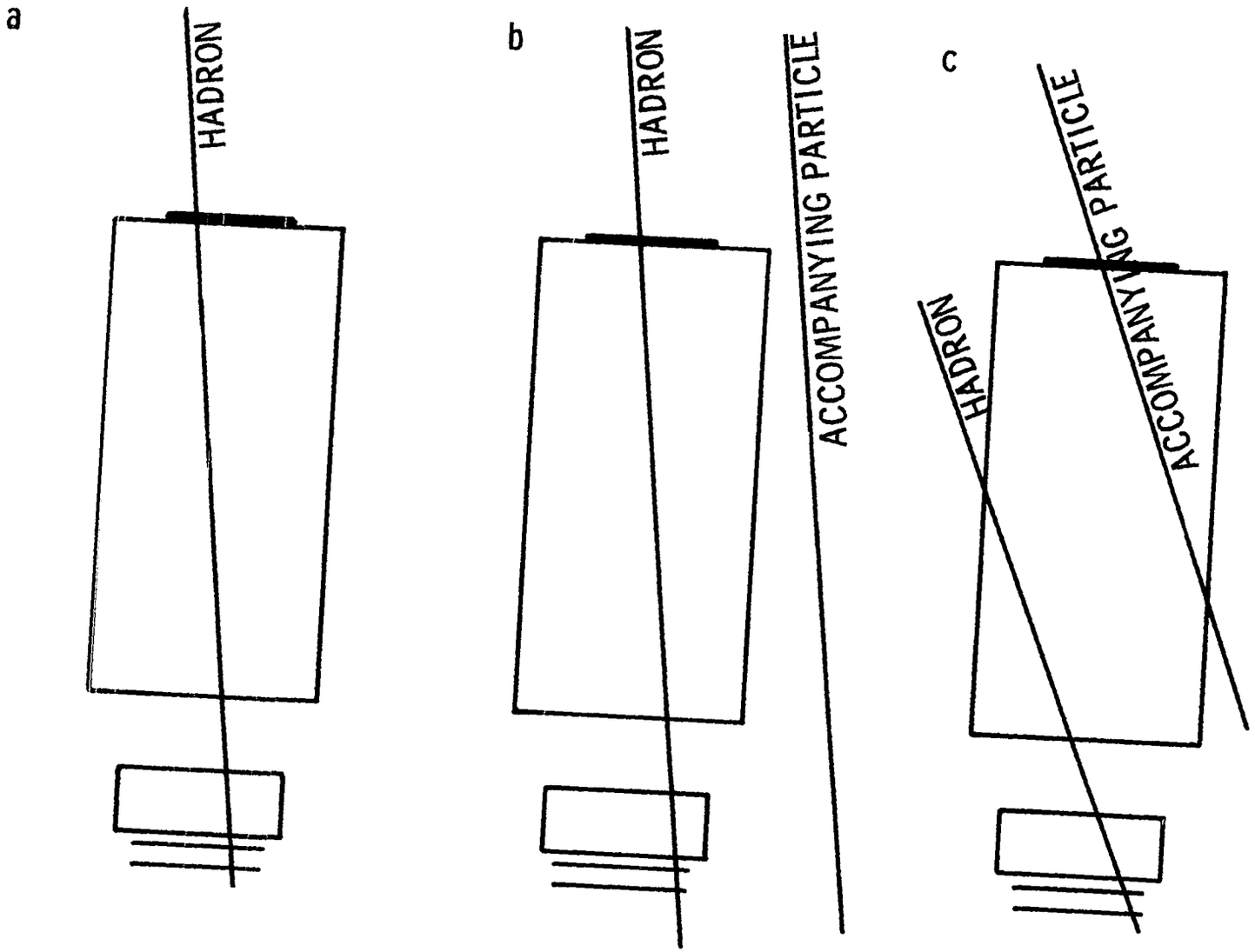

Fig. 25. Three types of events which may be observed

particles, and thus the AUX data are closely related to the question of the Cerenkov counter's efficiency. If accompanying particles are numerous they will strike the SC layer, causing events like that in Fig. 25c, often enough to account for the Cerenkov "inefficiency".

The fraction of events having AUX signals (%AUX) is shown as a function of S2+S3 in Fig. 26. A signal from the AUX counter indicates that at least one accompanying particle was present. It is clear that almost all events with large cascade size are accompanied, while events with small cascade size are unaccompanied. This is in agreement with the findings of Gaisser and Yodh[20] and with their interpretation: the hadrons striking the calorimeter originate in interactions in the atmosphere about one interaction length above the calorimeter. The accompanying particles are produced in the same interaction. At higher energies, the products of the interaction all emerge in the forward direction with small angular spread, while at low energies the products have a wider angular distribution. Thus the high energy hadrons arrive closely surrounded by accompanying particles while the particles accompanying low energy hadrons are too widely scattered to be detected by the AUX counter.

To determine whether accompanied particles outside the Cerenkov acceptance were responsible for the Cerenkov counter's inefficiency, the efficiency was determined sep-

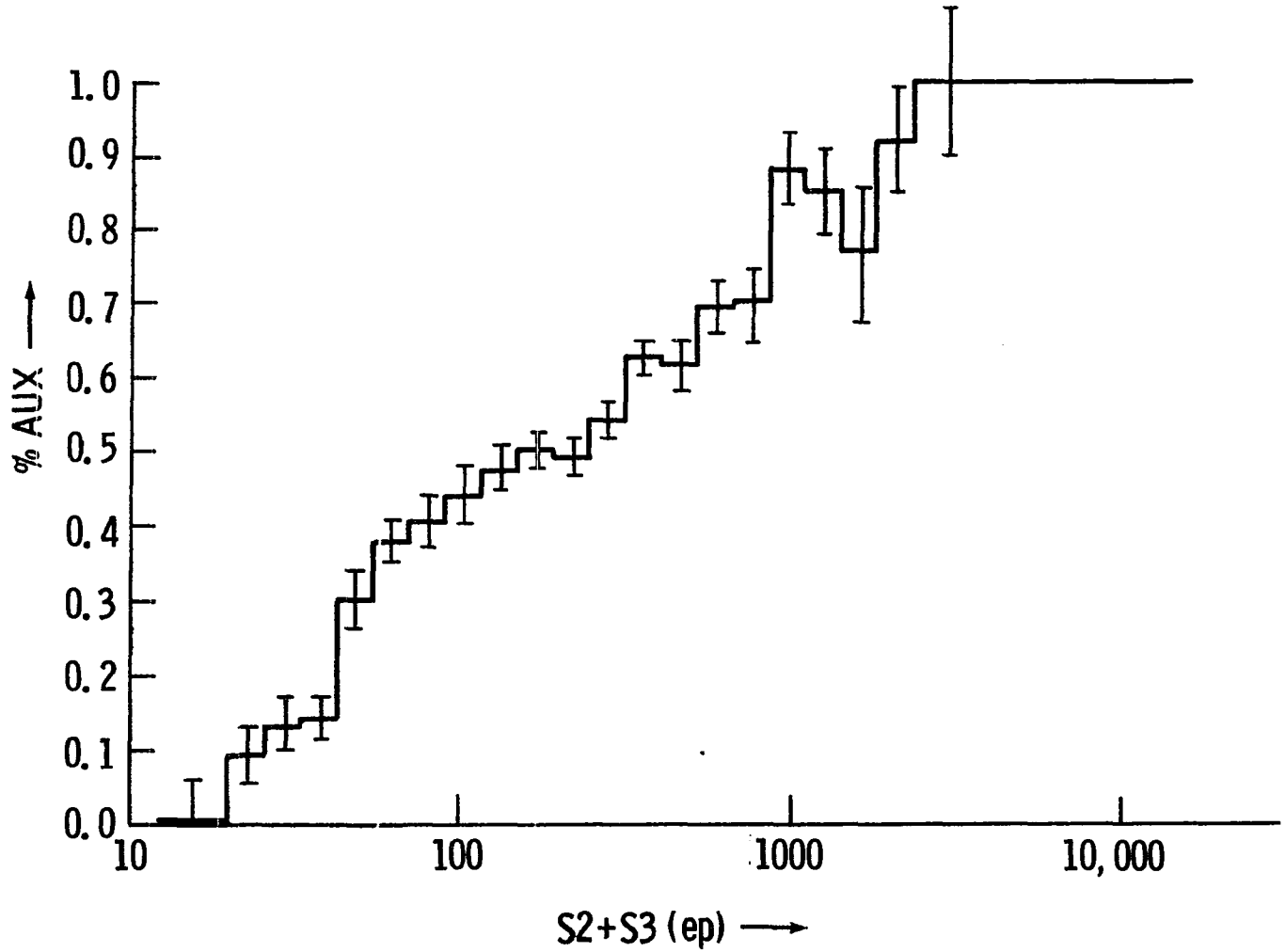

Fig. 26. Fraction of events having AUX signals vs. S2+S3

arately for accompanied and unaccompanied events. The reasoning behind this is that events unaccompanied over the large AUX array are not likely to be of the type shown in Fig. 25c. Thus events with no AUX signal should have a higher Cerenkov efficiency than those with AUX signals. The result of the comparison is shown in Fig. 27. For S2+S3>100 ep, the value of %C is .557±.026 for accompanied events and .623±.03 for unaccompanied events. This is a weak indication (1.7σ) that the Cerenkov inefficiency is due to accompanying particles, but the evidence is certainly not compelling. The separation of accompanied and unaccompanied events by the AUX counters is not absolute, so further tests are required.

The effect of accompanying particles on the Cerenkov efficiency was further investigated by looking at the fraction of events having S0 triggers (%S0) for Runs 15 and 16. If S0 is triggered only by the incident hadron, %S0 should simply be equal to the ratio of the geometric acceptances with and without S0: %S0 = 641/7618 = .086. If S0 is triggered by accompanying particles, then %S0 will be increased.

Fig. 28 shows %S0 vs. S2+S3 for Runs 15 and 16. The two lowest bins give %S0 = .098±.01, in agreement with the value expected from the ratio of the acceptances. The three bins at higher S2+S3 give %S0 = .158±.01. The increase in the value of %S0 over that found at low S2+S3 is .06±.014.

Fig. 27. %C vs. S2+S3 for accompanied and unaccompanied events

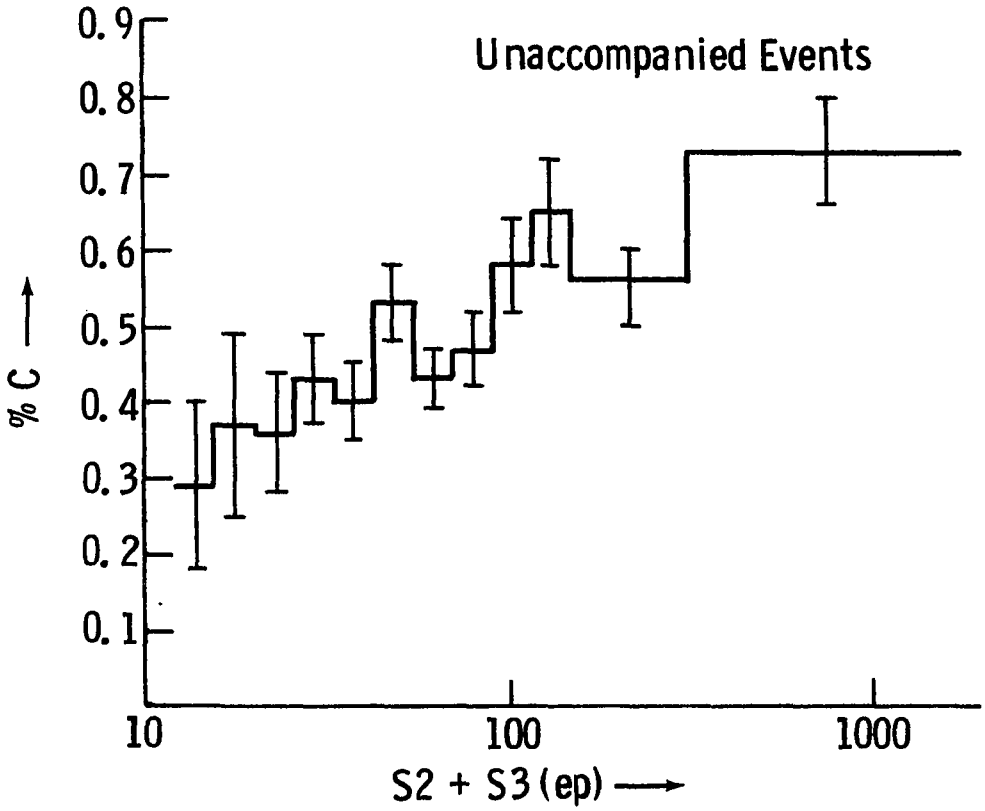
Unaccompanied Events
0.9
0.8
0.7
0.6
0.5
0.4
0.3
0.2
0.1
% C
10
100
1000
S2 + S3 (ep)

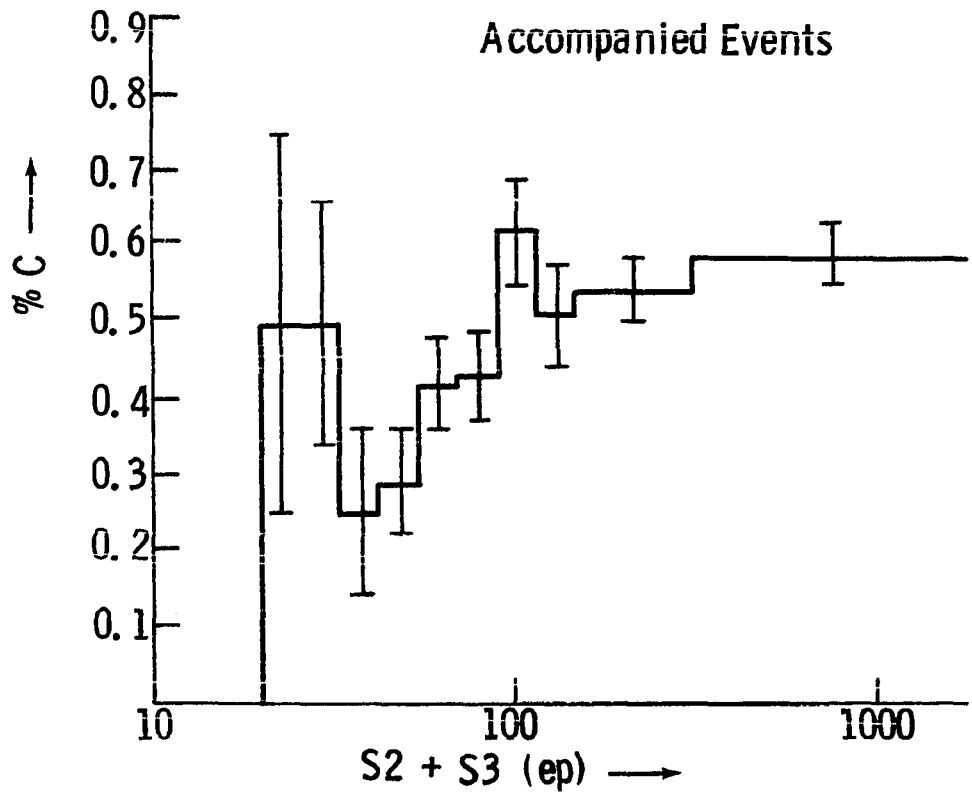
Accompanied Events
0.9
0.8
0.7
0.6
0.5
0.4
0.3
0.2
0.1
% C
10
100
1000
S2 + S3 (ep)

This increase must be due to triggers of the S0 counters by accompanying particles, causing events like that shown in Fig. 25c. These events give no Cerenkov signals, causing a Cerenkov "inefficiency" of .06/.158 = .38±.09, in agreement with the observed Cerenkov efficiency. Thus the Cerenkov inefficiency can be explained as the result of S0 triggers by accompanying particles.

As a further check, the expected rate for events like that of Fig. 25c was calculated. The accompanying particles were assumed to be uniformly distributed with an average density D which was dependent on S2+S3. At any given S2+S3, D is related to the fraction of events having AUX signals: $\%AUX = 1-e^{-DA}$, where A is the area of the AUX counters. This relation was inverted to find D, which is shown in Fig. 29 as a function of S2+S3. The probability that S0 is struck by an accompanying particle is then $\%S0 = 1-e^{-DAS0}$, where A_{S0} is the area of the S0 array. The probability that the incident hadron struck S0 was added to this, and the sum, graphed in Fig. 28, is a prediction of the number of S0 triggers which should be observed. There is qualitative agreement with the observed behavior, and the predicted rate of S0 triggers by accompanying particles is more than sufficient to account for the observed Cerenkov "inefficiency".

If the Cerenkov counter's efficiency is assumed to be independent of S2+S3, the pion-to-proton ratio (π/p) of the

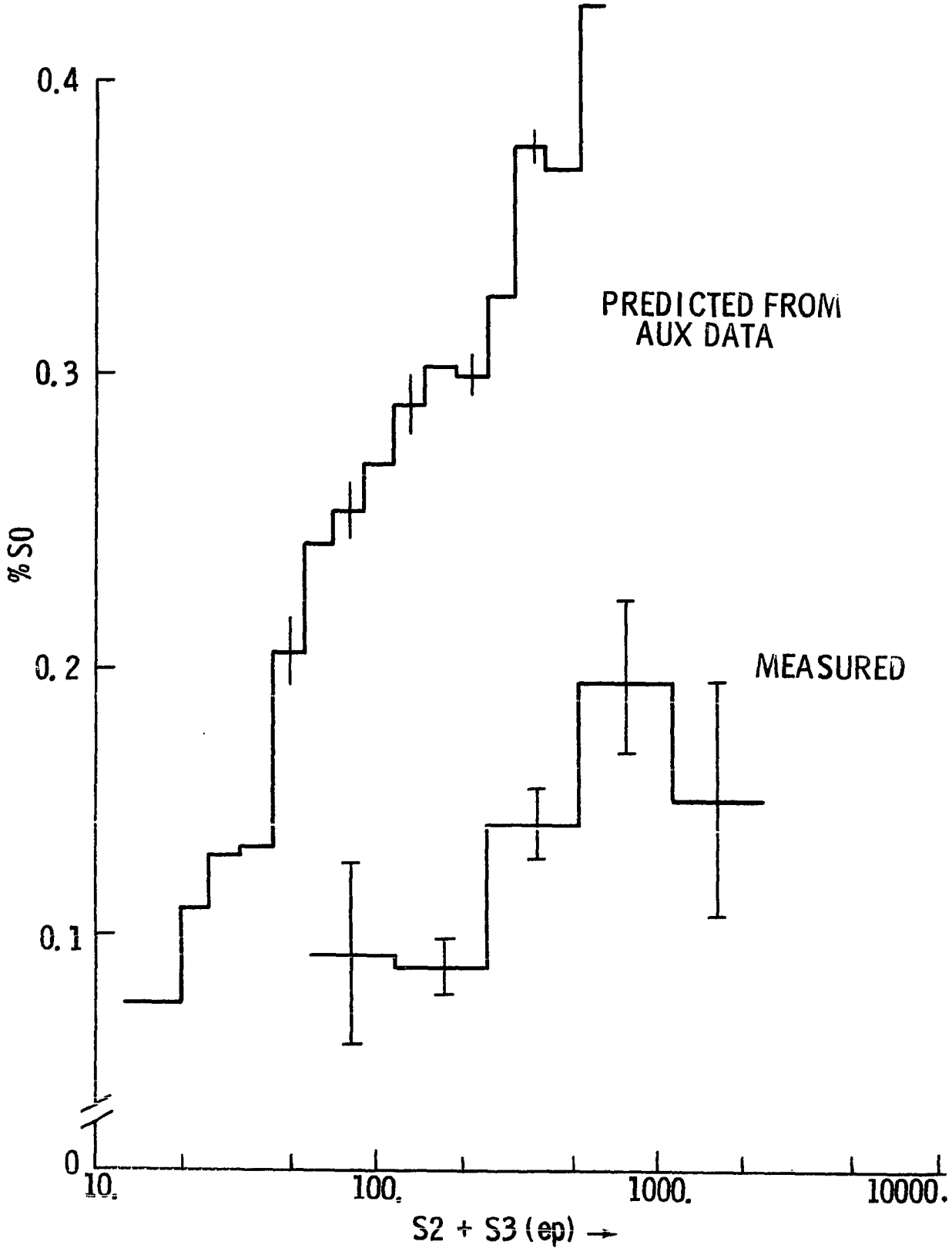

Fig. 28. Fraction of events having S0 triggers vs. S2+S3

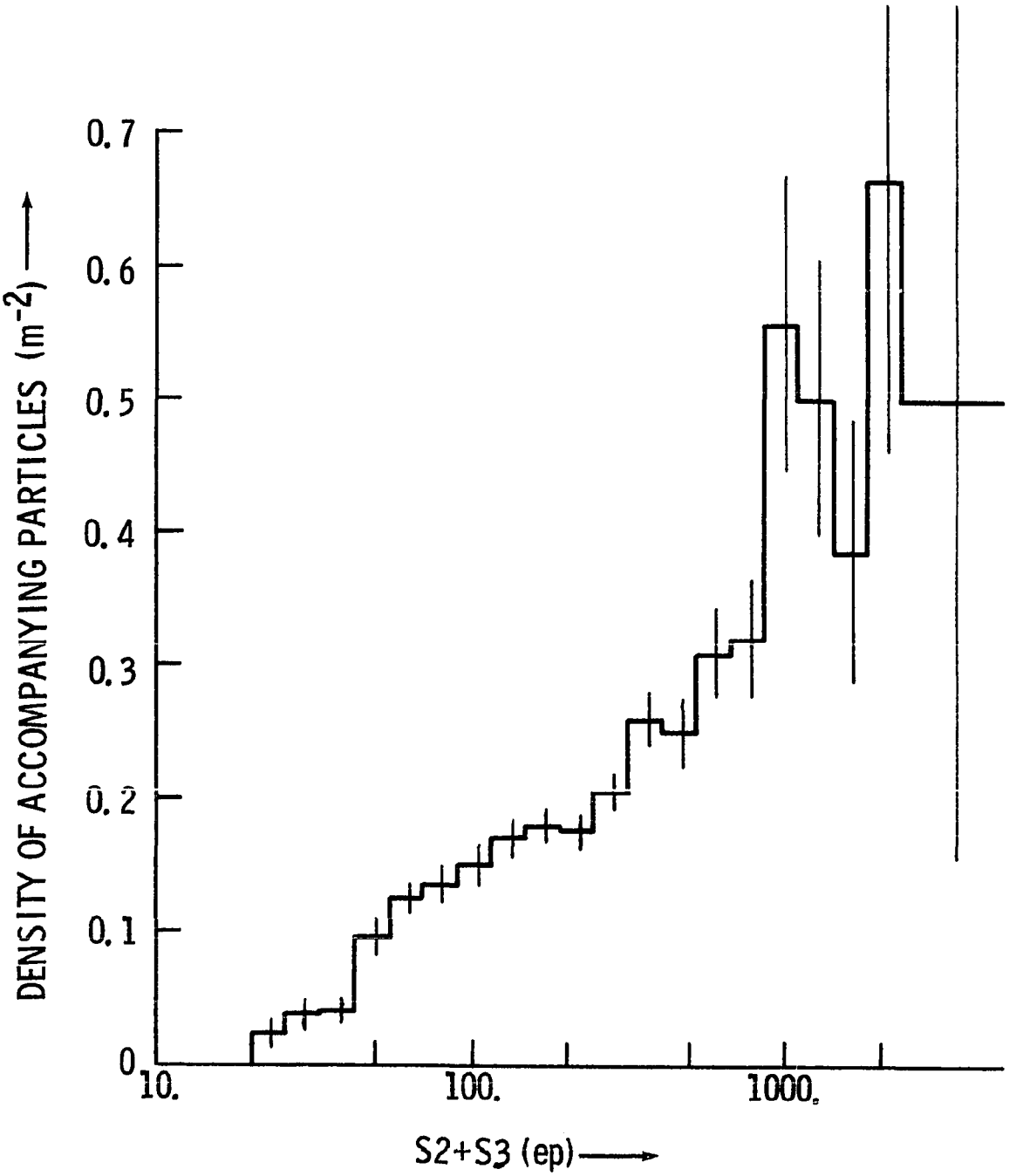

Fig. 29. Density of accompanying particles derived from AUX counter data

incident flux can be determined. The Cerenkov threshold for protons in air is 40 GeV, which corresponds to a cascade size of 154 ep, and the Cerenkov threshold for pions is 6.4 GeV, corresponding to 38 ep.

Thus in the region 38-154 ep only pions should produce Cerenkov signals. To minimize confusion of events above and below the Cerenkov thresholds due to the calorimeter's resolution, the fraction of events due to pions was calculated only for the region 50-90 ep. The Cerenkov efficiency above 300 ep was taken as a measure of the Cerenkov counter's absolute efficiency, so that, if F is the fraction of events due to pions in the region 50-90 ep, $F = \frac{\%C(50\text{-}90 \text{ ep})}{\%C(\text{above } 300 \text{ ep})}$ The result is $F = .650 \pm .06$, where a correction has been included for the probability (9%) that the incident hadron struck a photomultiplier in the Cerenkov counter. This is equivalent to a pion-to-proton ratio at equal incident energy of $\pi/p = .617 \pm .16$, where the error is statistical only. If the Cerenkov counter's efficiency decreases with increasing S2+S3, as is expected because of triggers outside the acceptance, the π/p ratio determined above will be higher than the actual ratio. Also, the contribution of muon events at low S2+S3 increases the observed ratio. Thus it seems best to take this value as an upper limit: $\pi/p \leq .94$ (2σ).

Although the Cerenkov "inefficiency" can be explained by accompanied hadron triggers, the evidence is rather indirect,

and alternative explanations should be considered. An inefficiency due to distortions in the Cerenkov counter's light buckets or low pulse heights from the photomultipliers cannot be ruled out. Also, the possibility that massive particles are responsible for some triggers remains. The signature of a massive particle would be a large cascade (large S2+S3) with no Cerenkov signal; this signature cannot be distinguished from those pions or protons which, for any reason, fail to give Cerenkov signals. If the Cerenkov "inefficiency" is assumed to be totally due to massive particles, the conclusion would be that 35% of the observed events have Lorentz factor $\gamma = \frac{1}{\sqrt{1-v^2/c^2}} \leq 41$.

The flux of massive particles corresponding to the observed Cerenkov inefficiency may be calculated as follows. Assuming the particles of mass M are produced in the atmosphere near the kinematic threshold, they would arrive with Lorentz factor $\gamma \cong 1 + M/m_p$, where m_p is the proton's mass. The particles would then have energy $E = \gamma M = M(1+M/m_p)$. This relation, applied to the range of incident energies investigated (35-1000 GeV) indicates that the experiment can detect masses in the range $5\ \text{GeV}/c^2 \lesssim M \lesssim 30\ \text{GeV}/c^2$. Under the assumption that the massive particles interact similarly to pions, the massive particle flux is $\phi_m = (1-\%C)\ N(\geq 200\ \text{ep})$, where $N(\geq 200\ \text{ep})$ is the integral flux for events with cas-

cade size exceeding that expected for 35 GeV pions. Since alternate explanations of the events with no Cerenkov signal exist, the observed rate should be taken as an upper limit: $\phi_m \leq 1.5 \times 10^{-7}$ $(cm^2\text{-sr-s})^{-1}$ for 5 GeV/c^2 $\leq$ M $\leq$ 30 GeV/c^2.

This result is obtained under the assumption that the massive particles give 1/3 of their energy to the electromagnetic cascade and have mean attenuation lengths of $\sim$ 100 g/cm^2, as do pions. An alternate, less restricted statement of the results can be made in terms of E', the electromagnetic energy deposited in the calorimeter by the incident particle: the observed rate for particles with E' $\geq$ 10 GeV and $\gamma \leq 41$ is constrained by $\phi_m \leq 4.8 \times 10^{-8}$ $(cm^2\text{-sr-s})^{-1}$, where no correction for detector efficiency has been made.

A summary by L.W. Jones[21] lists several experiments which have searched for massive particles by measuring their delay behind the fronts of associated air showers.[22,23,24] These experiments gave no confirmed positive results, and the upper limits derived for massive particles with $\gamma \lesssim 30$ range from $\sim 10^{-11}$ to 10^{-9} $(cm^2\text{-sr-s})^{-1}$. However, the experiments are sensitive only to particles produced sufficiently far above the detectors ($\sim$ 10 km for γ = 30 particles) for their delays relative to the air showers to be significant. Thus the particles must have a rather long attenuation length to be detected, and their lifetime must exceed $\sim 10^{-6}$ s. The present experiment is not sensitive to particles with

long attenuation lengths, but does provide an upper limit to the flux of massive particles where the assumption of the long life time is not necessary.

RESULTS AND DISCUSSION

In the preceding section, the relation between cascade size and hadron energy was derived. With this relation, the charged hadron spectrum can be calculated and some conclusions can be drawn about the performance of the apparatus.

The Hadron Spectrum

The contributions of pions and protons to the observed spectrum must be considered separately because a given cascade size corresponds to different energies for the two species:

$$\frac{dN\text{hadrons}}{dE} = \frac{dN\pi}{dE} + \frac{dNp}{dE}$$

For pions, the relation:

$$\frac{dN_\pi}{dE} = \frac{F}{\varepsilon} \frac{dN}{d(S2+S3)\pi} \frac{d(S2+S3)\pi}{dE}$$

is used, where the functions are evaluated at the S2+S3 value produced by pions of energy E. F is the fraction of events at any cascade size which is caused by pions. The fraction is taken to be equal to the 2σ upper limit derived from the Cerenkov data: $F = .77$. This value is assumed to be independent of S2+S3 in the following analysis. ε is the efficiency of the apparatus for detecting hadrons and has value 0.53.

For protons, a similar relation is used:

$$\frac{dN_p}{dE} = \frac{1}{\varepsilon} \frac{dN}{d(S2+S3)_p} \frac{d(S2+S3)_p}{dE} (1-F)$$

where the functions are evaluated at the S2+S3 value corresponding

to protons of energy E. If pions produce twice the cascade size as protons of the same energy, and if the integral cascade spectrum falls like $(S2+S3)^{-\gamma}$, the spectrum can be written:

$$\frac{dN\text{hadrons}}{dE} = \frac{1}{\varepsilon}\,\frac{dN}{d(S2+S3)_\pi}\,\frac{d(S2+S3)_\pi}{dE}\,\left[F+2^\gamma(1-F)\right]$$

For $\gamma = 1.59$, as determined in the section on data analysis, the expression in brackets has the value $1.46\pm.03$. For fluxes of all pions and all protons, the values of this quantity would be 1.0 and 3.0 respectively; for $\pi/p = 0.5$, as found by Brooke et al.[3], the value would be 1.8. Note that the error quoted for this quantity is statistical only.

The hadron spectrum was calculated as described above and is shown in Fig. 30. A power law fit to the points above S2+S3 = 200 ep gives $\frac{dN}{dE} = 1.08\pm.35\times10^{-9}\left(\frac{E}{100GeV}\right)^{-2.77\pm.06}$ $(cm^2\text{-sr-s-GeV})^{-1}$.

The spectrum is also plotted in Fig. 31 for comparison with the results of other experimenters. All points have been corrected to an atmosphere depth of 990 g/cm^2. The results of this experiment are similar to the other measurements shown.

Some of the differences seen can be explained on the basis of triggering requirements. Cowan and Matthews[12], for example, required that hadrons be unaccompanied over their 4_m^2 calorimeter. In view of the number of accompanying particles

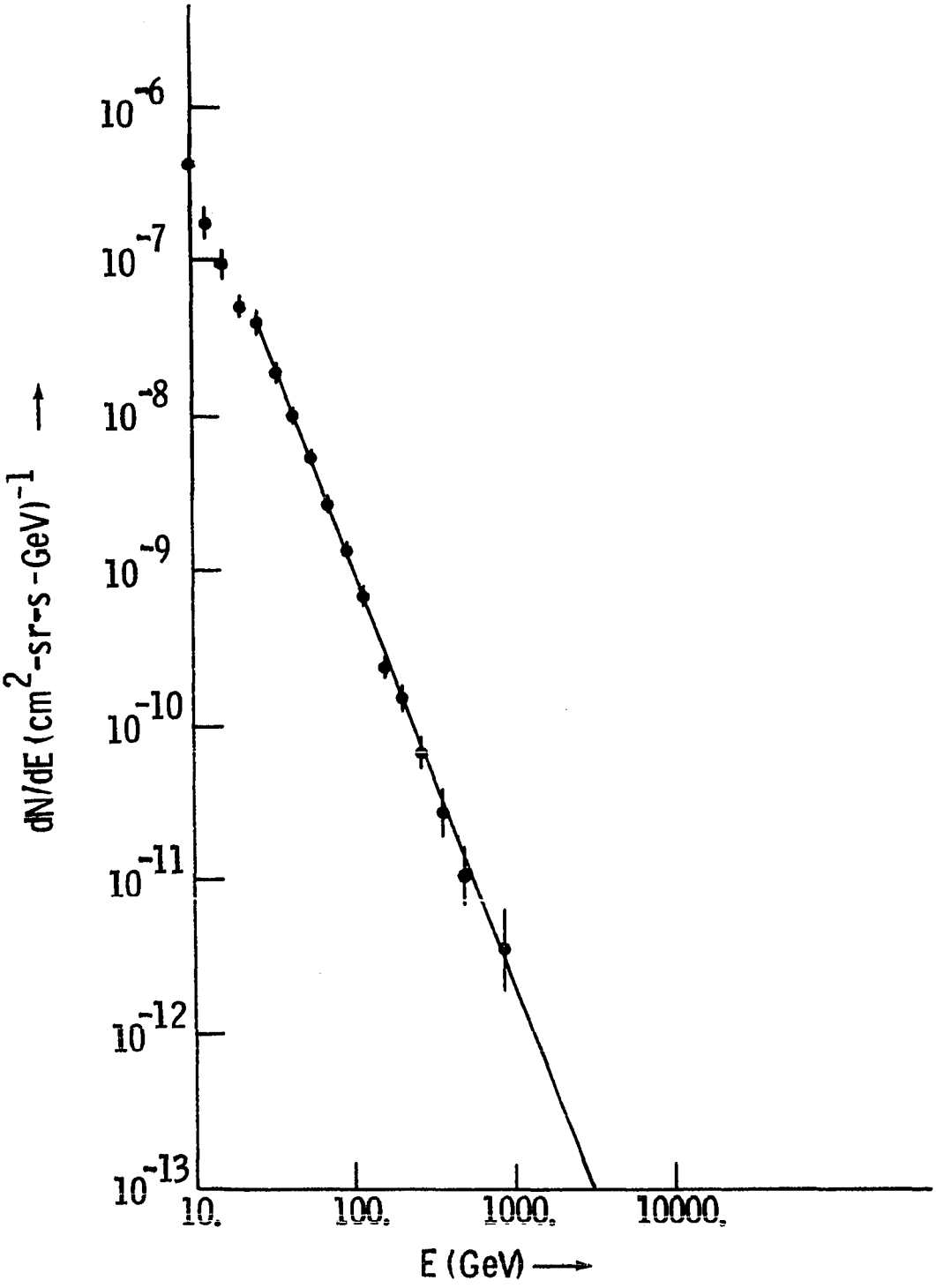

Fig. 30. Hadron spectrum derived from this experiment (pions + protons)

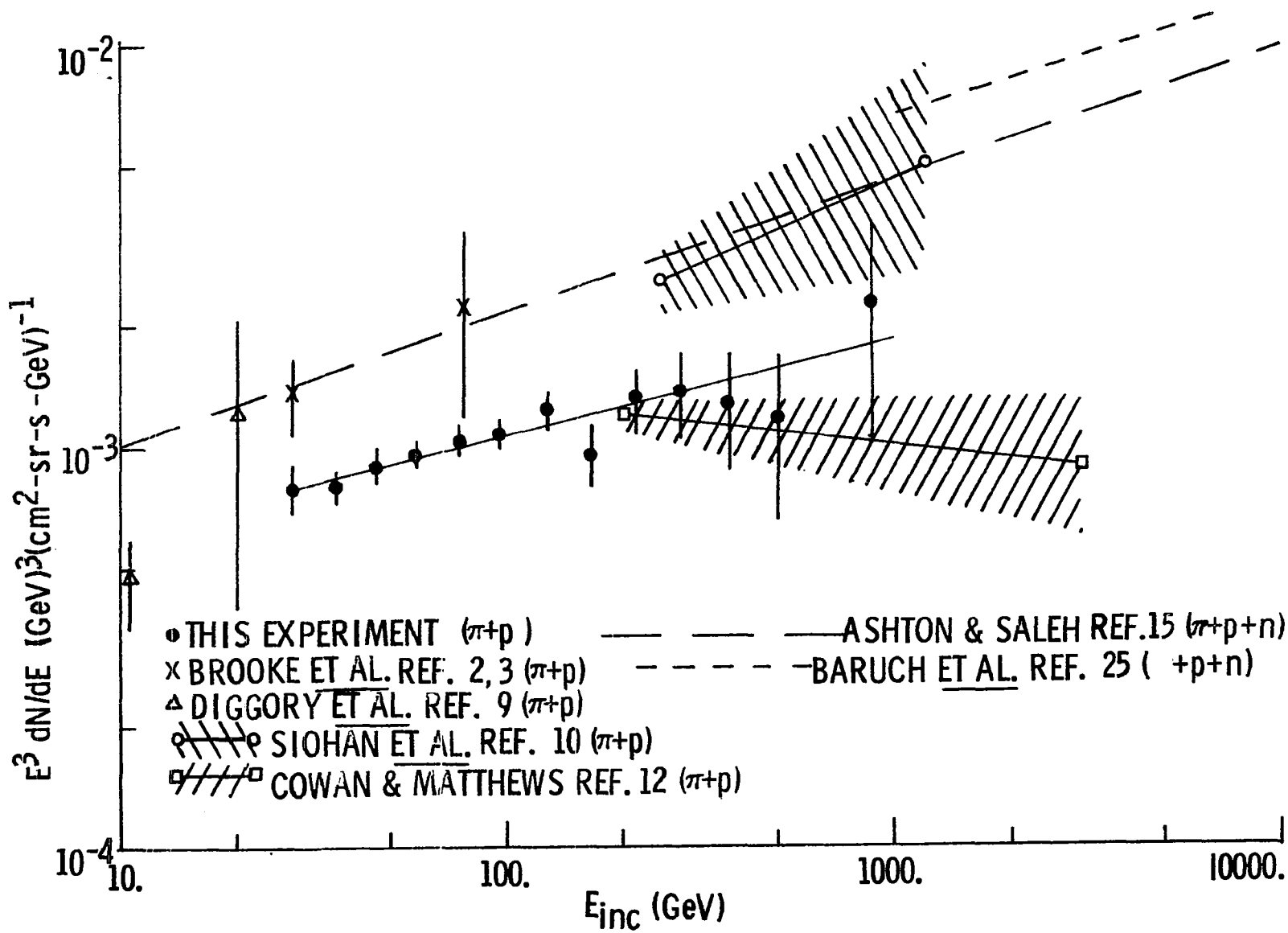

Fig. 31. Comparison of hadron spectra from various experiments

seen in the present experiment by the $3.8m^2$ AUX counters, their event rate is understandably lower than that found by other researchers. The accompaniment probability increases with energy, so the slope of the spectrum is also affected. Baruch et al.[25] and Ashton and Saleh[15] include neutrons in the event rates while the other results are for pions and protons only, so their rates are among the highest shown.

Taking these factors into consideration, the intensity found by the present experiment remains lower than the majority of the other results. This may be due to an error in the energy calibration of the calorimeter (±20%) or in the π/p ratio assumed. The π/p ratio of 0.94 assumed is in fact an upper limit; if π/p is smaller, the measured hadron intensity is larger than that shown. If $\pi/p = 0.5$, as found by Brooke et al.[3], the measured intensity shown is too low by a factor of 1.25. The requirement that one and only one counter in S1 be triggered might also reject some events, reducing the observed intensity. The slope found for the spectrum is well within statistical errors of the other results shown except that of Cowan and Matthews, who obtained a slope of 3.11±.12. Thus there is no serious disagreement between this experiment and earlier studies of the hadron spectrum.

Evaluation of the Cerenkov Counter

The 2σ upper limit on the π/p ratio determined from the

Cerenkov data is $\pi/p \leq .94$. The error quoted is statistical only, and there are possibly serious systematic errors involved in this determination. The ratio was measured near the Cerenkov counter's threshold for protons (40 GeV). Brooke et al.[3] found a π/p ratio of 0.5 in this region, while Cowan and Matthews[12] found a value of 2.0 at an average energy of 330 GeV. The present result is not compatible with that of Cowan and Matthews, but is compatible with that of Brooke.

The Cerenkov counter's efficiency was found to be about 60%. The inefficiency is thought to be due to triggers by accompanied particles lying outside the Cerenkov counter's acceptance. The possibility cannot be ruled out that the "inefficiency" is due to massive hadrons which are below the Cerenkov threshold for air ($\gamma = 41$). The best limit which can be put on the intensity of massive hadrons by this experiment is thus: $\frac{dN}{dE} \leq 4.3\times10^{-10} \left(\frac{E}{100\ GeV}\right)^{-2.77}$ $(cm^2\text{-sr-s-GeV})^{-1}$ for particles of mass $M \geq \frac{E}{46}$ GeV, or for the integral rate $\phi_m \leq 1.5\times10^{-7}$ $(cm^2\text{-sr-s})^{-1}$ for 5 GeV/c^2 $\leq M \leq$ 3 GeV/c^2.

In any case, the presence of accompanying particles makes the Cerenkov counter in its present design rather ineffective. The accompanying particles can cause confusion by registering either in the Cerenkov counter or in the triggering arrays. These problems could be solved by adding track determining

devices to the apparatus. If the hadron's path could be identified, hadrons outside the Cerenkov counter's acceptance could be rejected. Also, the Cerenkov signals from the particular segment of the counter which the hadron traversed could be separately considered; if there were no paths of accompanying particles through that segment, the Cerenkov signal of the hadron could be unambiguously determined. In designing Cerenkov counters, it would thus be advisable to make the area of each segment smaller than (1/density of accompanying particles).

Evaluation of the Calorimeter

The agreement of the hadron spectrum calculated above with that found by other observers indicates that the calorimeter's performance is reasonably well understood. Some questions about its usefulness in other applications remain, however.

The energy resolution of the calorimeter was not measured, but seems to be obtainable from accelerator data and from Monte Carlo simulations for any particular detector (see, for example, Appendix II). For energies up to 10^{12} eV, the resolution of the calorimeter used in this experiment was about a factor of two. This was adequate for the purpose at hand, i.e. measuring the cosmic ray spectrum where no rapid change of the spectral shape was expected.

The absolute energy calibration of the calorimeter was a problem in this experiment. The main uncertainty in this experiment was in the physical calibration of the detectors, but there are also uncertainties in hadron interaction characteristics and in the electromagnetic cascade curves which are used to relate cascade size to incident energy. For these reasons, it would be desirable to calibrate future calorimeters of this design using accelerator beams of hadrons.

Another property of the calorimeter to be considered is that it responds only to that fraction of the incident energy which is given to the electromagnetic cascade. Thus electrons, pions, and protons of the same energy would all produce very different signals in the calorimeter. This situation could be improved by making the target several nuclear interaction lengths thick, so that a larger fraction of the incident hadron's energy is converted to electromagnetic products. The target material, in this case, should be a light element so that the target thickness in radiation lengths is small, to minimize the uncertainty in the stage of cascade development. A thicker target would also improve the energy resolution.

Particular difficulties were encountered in this experiment because the scintillation counters used in the calorimeter were not linear in their response. The time and effort required to calibrate the detectors was such that linear devices such as proportional chambers or ionization chambers

might have been worthwhile despite the additional construction time involved. The spatial resolution of proportional counters makes them especially desirable at high energies, where many hadrons are closely accompanied.

CONCLUSIONS

A study of cosmic ray hadrons at ground level has been performed using a shallow calorimeter and gas Cerenkov counter. The measured hadron spectrum and π/p ratio are in agreement with earlier experimental results, and the performance of the calorimeter has been evaluated for future applications.

The hadron spectrum was measured over the range 3×10^{10}-10^{12} eV. The result is consistent with a single power law spectrum of form $\frac{dN}{dE} = 1.08\pm.35\times10^{-9} \left(\frac{E}{100GeV}\right)^{-2.77\pm.06}$ $(cm^2\text{-}sr\text{-}s\text{-}GeV)^{-1}$ over the entire range. A 2σ upper limit on the π/p ratio was found of $\pi/p \leq 0.94$.

No amomalies in the spectrum were found. No evidence for massive particles was found, although the upper limit placed on the massive particle flux is not stringent: $\phi_m \leq 1.5\times10^{-7}$ $(cm^2\text{-}sr\text{-}s)^{-1}$ for particles of mass 5 GeV/c^2 $\leq$ M $\leq$ 30 GeV/c^2.

The apparatus was found to be adequate for studying the hadron spectrum over the energy range indicated. Modifications to improve performance in the presence of accompanying particles have been suggested, in particular the addition of track determining devices and the use of position sensitive detectors in the calorimeter.

Recommendations for Future Study

A repetition of the experiment is not being planned at this time. Some possible applications of the shallow calorimeter technique have been considered, however, for a modified design with proportional counter detectors. The main advantages of the device would be its good spatial resolution, large geometric acceptance, and low weight compared to deep calorimeters.

One particular use would be in studying the hadron flux as a function of altitude. The large acceptance would allow such studies to be done at energies to at least 10^{12} eV. The overall size and weight ($\sim$ 2000kg) are such that the region from sea level to mountain altitude could be covered by placing the calorimeter on a medium-sized truck for transport; balloon flights to altitudes of $\sim$ 100 g/cm^2 would also be possible. The use of a single device over a wide range of altitude would give a fairly precise picture of the hadron flux's development in the atmosphere.

A conclusion of this research, then, is that the shallow calorimeter has been - and can be - a useful tool in cosmic ray studies. In applications where energy resolution is not important, the large acceptance of the shallow calorimeter makes it a leading candidate for work at high energies.

APPENDIX I

MUON EVENT RATE CALCULATIONS

The shallow calorimeter is not able to distinguish events caused by electromagnetic interactions of muons from those caused by nuclear interactions of hadrons. Since only hadrons were of interest in this experiment, the effects of muon interactions had to be determined and eliminated. This is possible because the muon flux has been measured fairly well and the cross sections for electromagnetic interactions are known. This appendix describes calculations of the muon event rate for the calorimeter described in the main body of this paper.

The muon interactions of interest for this experiment are those which transfer an energy of 1 GeV or more to an electromagnetic cascade. Electromagnetic interactions of muons are similar to those of electrons, but the cross sections are smaller by a factor $\sim (m_\mu/m_e)^2$. The probability of a 10^{12} eV muon producing an energy transfer $\geq$ 1 GeV in the calorimeter is only 5%. Thus the observed muon events are due to interactions of a small fraction of the incident muons.

The processes responsible for muon events are the production of knock-on electrons, direct production of electron-positron pairs, and bremsstrahlung interactions. The interaction probabilities can be expressed as $P(E,E')dE'$, the probabil-

ity per g/cm^2 of target that a muon of energy E will produce an electromagnetic product with energy in the range (E',E'+dE'). P(E,E') is obtained from the cross sections for the interactions: $P(E,E') = N\sigma(E,E')/A$ where N is Avogadro's number and A is the atomic weight of the target material.

In the knock-on process, a muon transfers an energy E' to an electron of the target material. Rossi[1] gives the interaction probability as

$$P(E,E')dE' = \frac{2\pi N(Z/A)r_e^2 m_e c^2}{E^2} \frac{1}{v^2}(1-v+v^2/2)dE' \text{ where } m_e, r_e$$

are the mass and classical radius of the electron and $v \equiv \frac{E'}{E}$.

A muon passing near a target nucleus can transfer some of its energy to an electron-positron pair produced in the field of the nucleus. The cross section for this direct pair production process is given by Kokoulin and Petrukhin[26]:

$$\sigma(E,v,\rho)dvd\rho = \frac{2}{3\pi}(Z\alpha r_0)^2 \frac{1-v}{v}\left[\Phi_e + \frac{m^2}{\mu^2}\Phi_\mu\right] dvd\rho \quad \text{where } P = \frac{E_+' - E_-'}{E'}$$

specifies the share of energy given to the electron and positron, and Φ_e, Φ_μ are defined by

$$\Phi_e = \left[\left((2+\rho^2)(1+\beta)+\xi(3+\rho^2)\right) \ln\left(1+\frac{1}{\xi}\right) + \frac{1-\rho^2-\beta}{1+\xi} - (3+\rho^2)\right]L_e$$

$$\Phi_\mu = \left[\left((1+\rho^2)\left(1+\tfrac{3}{2}\beta\right) - \frac{1}{\xi}(1+2\beta)(1-\rho^2)\right) \ln(1+\xi) +\right.$$

$$+ \frac{\xi(1-\rho^2-\beta)}{1+\xi} + (1+2\beta)(1-\rho^2)\Big] L_\mu$$

$$L_e = \ln\left(\frac{AZ^{-1/3}\sqrt{(1+\xi)(1+Y_e)}}{1+\frac{2m\sqrt{e}AZ^{-1/3}(1+\xi)(1+Y_e)}{Ev(1-\rho^2)}}\right)$$

$$L_\mu = \ln\left(\frac{\frac{A\mu}{m} Z^{-1/3}\sqrt{(1+1/\xi)(1+Y_\mu)}}{1+\frac{2m\sqrt{e}AZ^{-1/3}(1+\xi)(1+Y_\mu)}{Ev(1-\rho^2)}}\right)$$

$$Y_e = \frac{5-\rho^2+4\beta(1+\rho^2)}{2(1+3\beta)\ln(3+1/\xi)-\rho^2-2\beta(2-\rho^2)}$$

$$Y_\mu = \frac{4+\rho^2+3\beta(1+\rho^2)}{(1+\rho^2)(3/2+2\beta)\ln(3+\xi)+1-\frac{3}{2}\rho^2}$$

$$\beta = v^2/2(1-v) \qquad \xi = (\mu v/2m)^2 (1-\rho^2)/(1-v)$$

In the bremsstrahlung process the muon produces a γ ray in the field of a target nucleus. Petrukhin and Shestakov[27] give the cross section:

$$\sigma(v,E)dv = \alpha(2Zr_e m_e/m_\mu)^2 (4/3 - 4/3v+v^2) \times$$

$$\times \ln\left[\frac{\frac{2}{3} A \frac{m_\mu}{m_e} Z^{-2/3}}{1 + A\sqrt{e}/2)\frac{m_\mu 2}{m_e E}\frac{v}{1-v} Z^{-1/3}}\right]\frac{dv}{v}$$

The desired result of the calculation was the rate of muon events to be expected as a function of cascade size (S2+S3) in the calorimeter. To get this, the muon rate as a function of cascade energy E' was calculated, and the cascade curves of Müller[17] were used to relate E' to cascade size. The relation between cascade energy and cascade size is shown in Fig. 32.

The event rate in the calorimeter as a function of S2+S3 may be written:

$$\frac{dN}{d(S2+S3)} = 108 \text{ g/cm}^2 \; \frac{dN}{dE'} \frac{dE'}{d(S2+S3)} \quad (\text{cm}^2\text{-sr-s-ep})^{-1}$$

$$\frac{dN}{dE'} = \int_{E'}^{\infty} \frac{dN_\mu}{dE} P(E,E')dE \quad (\text{cm}^2\text{-sr-s-GeV-g/cm}^2)^{-1} \text{ where}$$

108 g/cm^2 is the thickness of the calorimeter target, dN_μ/dE is the incident muon spectrum, and P(E,E') is the sum of the three interaction probabilities described above. The muon spectrum of Allkofer *et al.*[5] was used for the calculations.

The integration over incident muon energy was done numerically for a number of values of E'. Fig. 33 shows the resulting muon event rate as a function of E'. Contributions of the knock-on, bremsstrahlung, and pair production processes are shown separately. The calculated muon event rate as a function of S2+S3 is shown in Fig. 34. For comparison, the event rate expected from the pion flux reported by Brooke

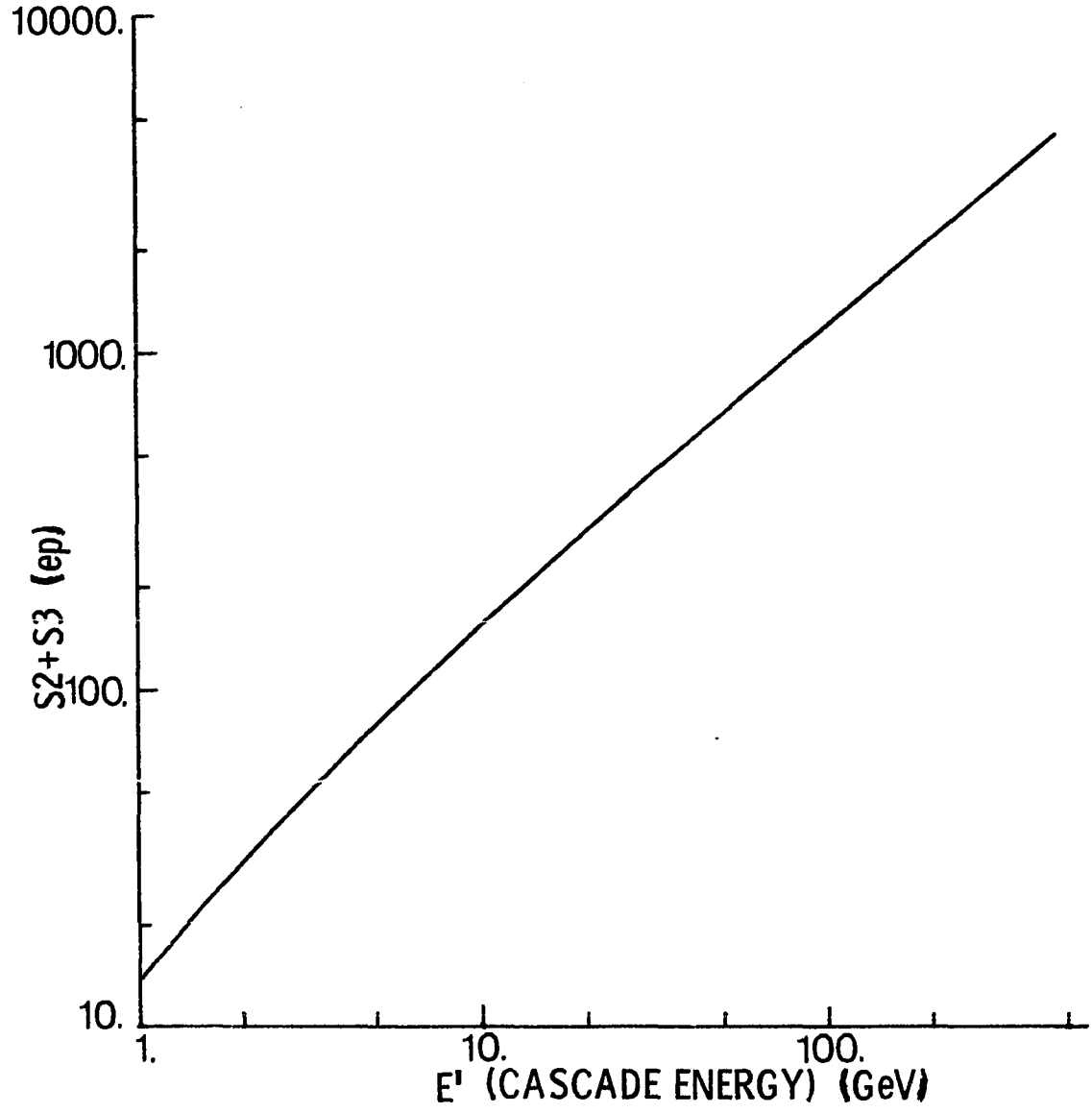

Fig. 32. Cascade size (S2+S3) vs. cascade energy for muon - initiated events

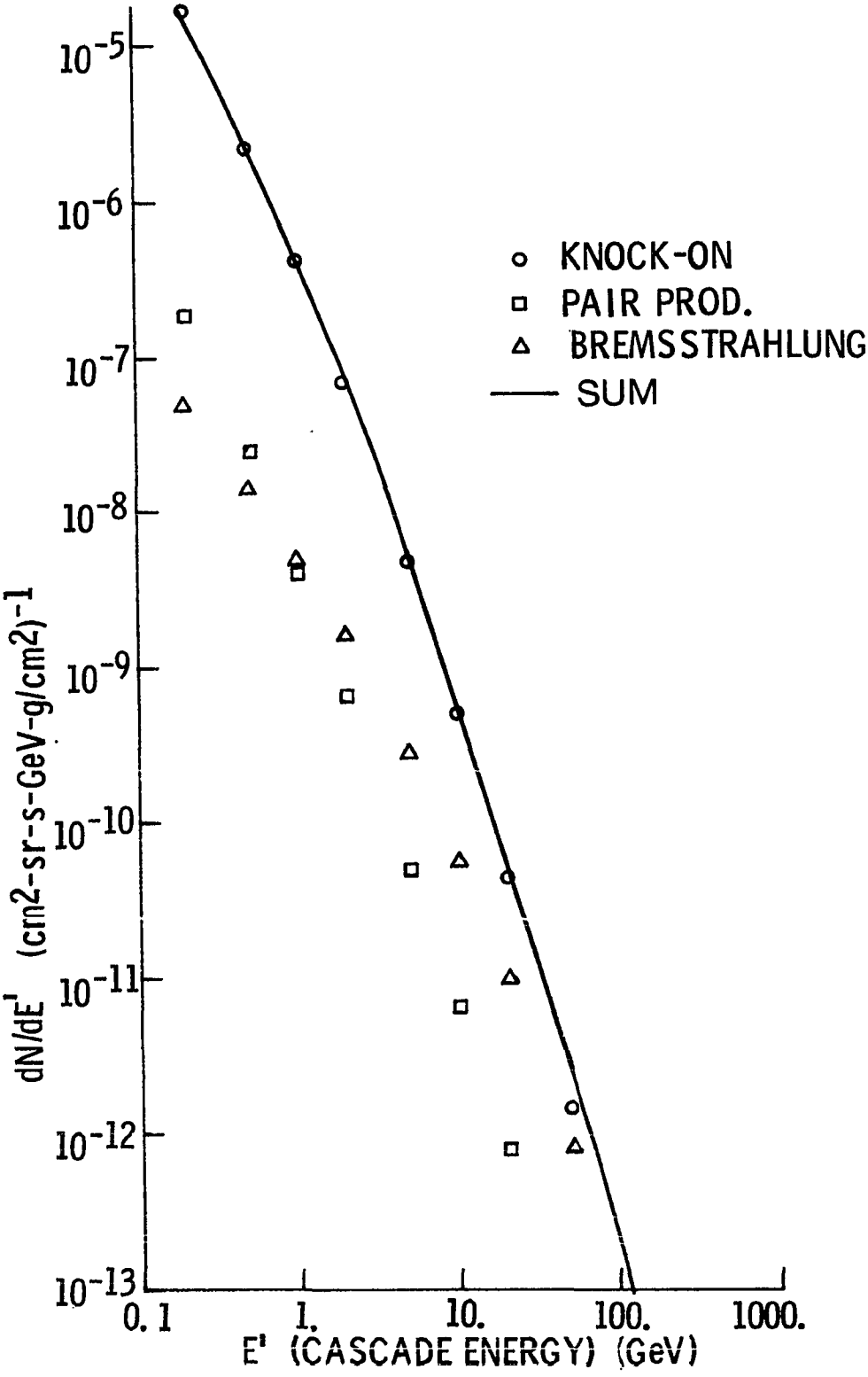

Fig. 33. Predicted dN/dE' vs. E' for muon events

et al.[3] is also shown. It is clear from Fig. 34 that the muon event rate is important at small cascade size, but becomes smaller than the rate due to hadrons at larger cascade size.

The muon rate could in principle be subtracted from the observed rate to obtain the hadron spectrum, but uncertainties in the energy scale for the calorimeter make this difficult in practice. It was therefore concluded that the calorimeter should be used to study hadrons only for cascade size $\geq$ 200 ep, where the muon rate is small enough ($\leq$ 40% of the total rate) to ignore (200 ep corresponds to an energy of 35 GeV for pions).

In conclusion, the muon event rate was found to dominate the hadron rate for cascade size S2+S3 < 200 ep. For larger sizes, the muon rate rapidly becomes negligible compared to hadrons. Consequently, only the data above S2+S3 = 200 ep were used in computing the hadron spectrum.

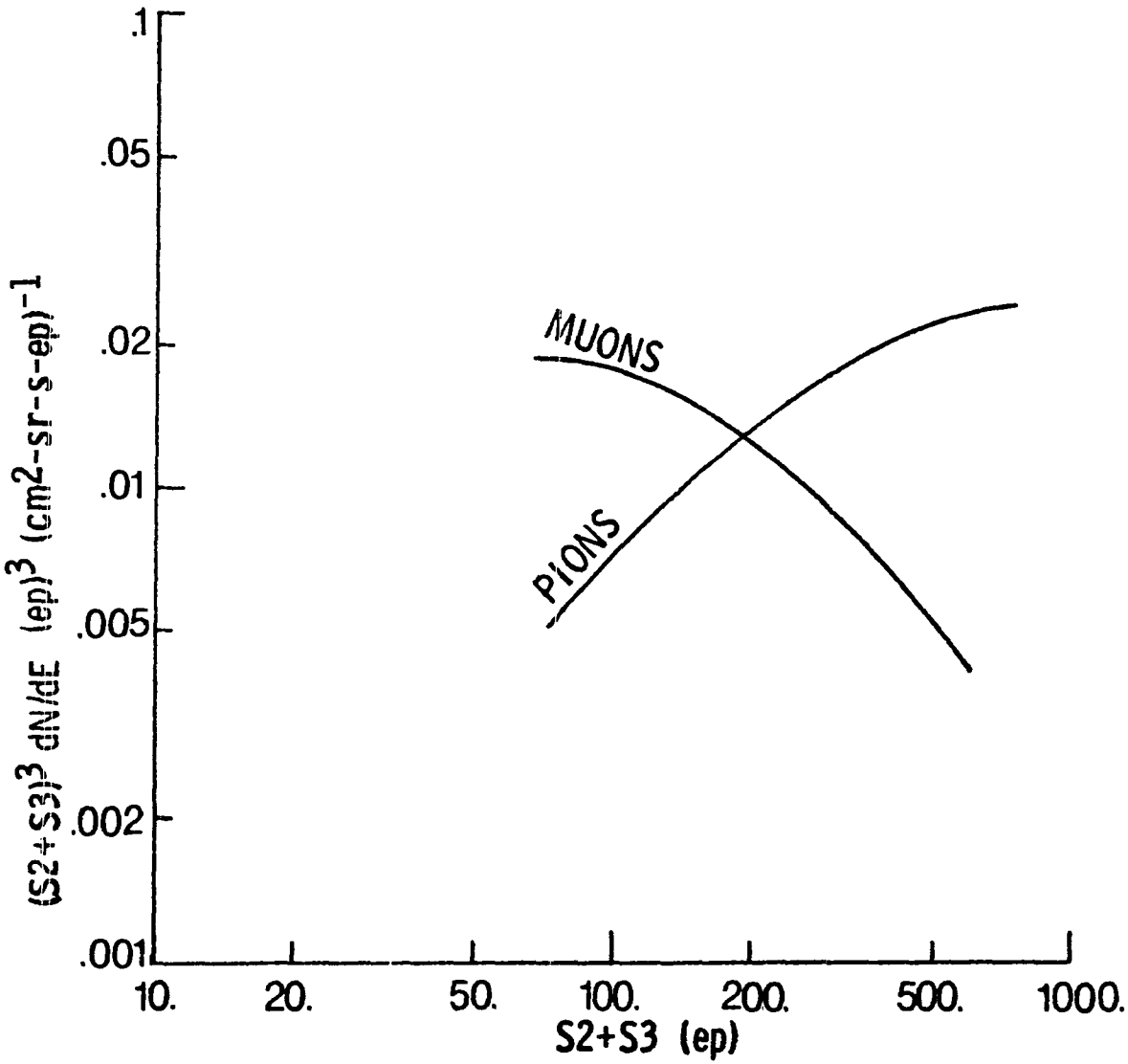

Fig. 34. Predicted event rates for muons and pions

APPENDIX II

HADRON EVENT SIMULATIONS

The shallow calorimeter measures only that fraction of an incident hadron's energy which is given to electromagnetic secondaries in a single interaction. Since this fraction can assume any value from zero to nearly one for a particular event, the calorimeter gives only a rough indication of incident energy on an individual basis. The effects of this uncertainty on the measured spectrum of cosmic ray hadrons was investigated by performing computer simulations of interactions in the calorimeter.

The calorimeter, which is described in detail in the main body of this paper, consisted of a cement target 108 g/cm^2 in thickness, under which were two layers of lead each 3.3 r.l. thick. Two layers of scintillation counters, labeled S2 and S3, lay under the first and second layers of lead respectively. Electromagnetic secondaries from hadron interactions in the target initiated electromagnetic cascades in the lead. The signal in the scintillators was roughly proportional to the energy of the electromagnetic secondaries.

The simulation process began with the generation of hadron interactions, assumed to occur at the center of the calorimeter target. Multiplicities of charged and neutral (π^0) secondaries were chosen using the semi-inclusive

scaling distribution of Slattery[28] and the average multiplicity values of Whitmore[18,29]. The neutral pions were each assumed to decay to two γ rays at a random angle in the pion rest frame, and the cascade curves of Müller[17] were then used to calculate the cascade size (in equivalent particles) produced by the γ rays at the positions of S2 and S3. The S2 and S3 cascade sizes were histogrammed for a large number of simulated events. The energy of the γ rays, and the fraction of incident energy given to all γ rays, k_γ, were also histogrammed.

Two methods of generating hadron events were used. The first, embodied in a program called SIM1, assigned momenta of the reaction products from the experimental distributions of D.C. Carey et al.[30] using the radial scaling hypothesis of F.E. Taylor et al.[31] The radial scaling formulation was used because the invariant cross sections for π^0 production, expressed in terms of the radial scaling variable $X_R \equiv E_{cm}/(\sqrt{s}/2)$ and the transverse momentum P_T, are relatively independent of energy over the range 50-500 GeV.[31] The momenta of pions were selected from the distributions subject to the constraints that momentum and energy be conserved. For incident protons, half the available energy, on average, was given to a leading nucleon. SIM1 was not used for incident pions because sufficient data on pion interactions was not available.

A second program, SIM2, used a set of event-generating

subroutines called SAGE which was written by J. Friedman[32,33]. The SAGE package generates events from a multiperipheral model which limits the four-momentum transfers between groups of particles. For each event the initial state masses and energy must be specified and the number and masses of secondaries must be provided as input. The routines then generate momenta and energies for all secondaries. Four parameters governing the distributions of the generated momentum transfers and invariant masses must also be provided as input. These parameters were chosen to give a value of $\langle k_\gamma \rangle$ near .17 for protons and to give $\langle P_T^2 \rangle$ near the experimental values reported by Whitmore[2]. For incident pions, the leading particle was allowed to be a π^+, π^-, or π^0 with equal probability, while for incident protons the leading particle was required to be a proton.

Fig. 35 shows the average cascade size in the S2 and S3 detectors produced by simulated protons of various incident energies using the SIM1 program. For comparison the pulse heights which would result if k_γ were always .17 and each event produced $2\langle n_{\pi^0} \rangle$ γ rays of equal energy are also shown. The simulation results are in fair agreement with the simpler calculation, differing by no more than 25% up to an incident energy of 1000 GeV. However, the precision of the simulation results was not considered adequate for determining the hadron spectrum. The calculated values of $\langle S2+S3 \rangle$ vs. E_{inc} were

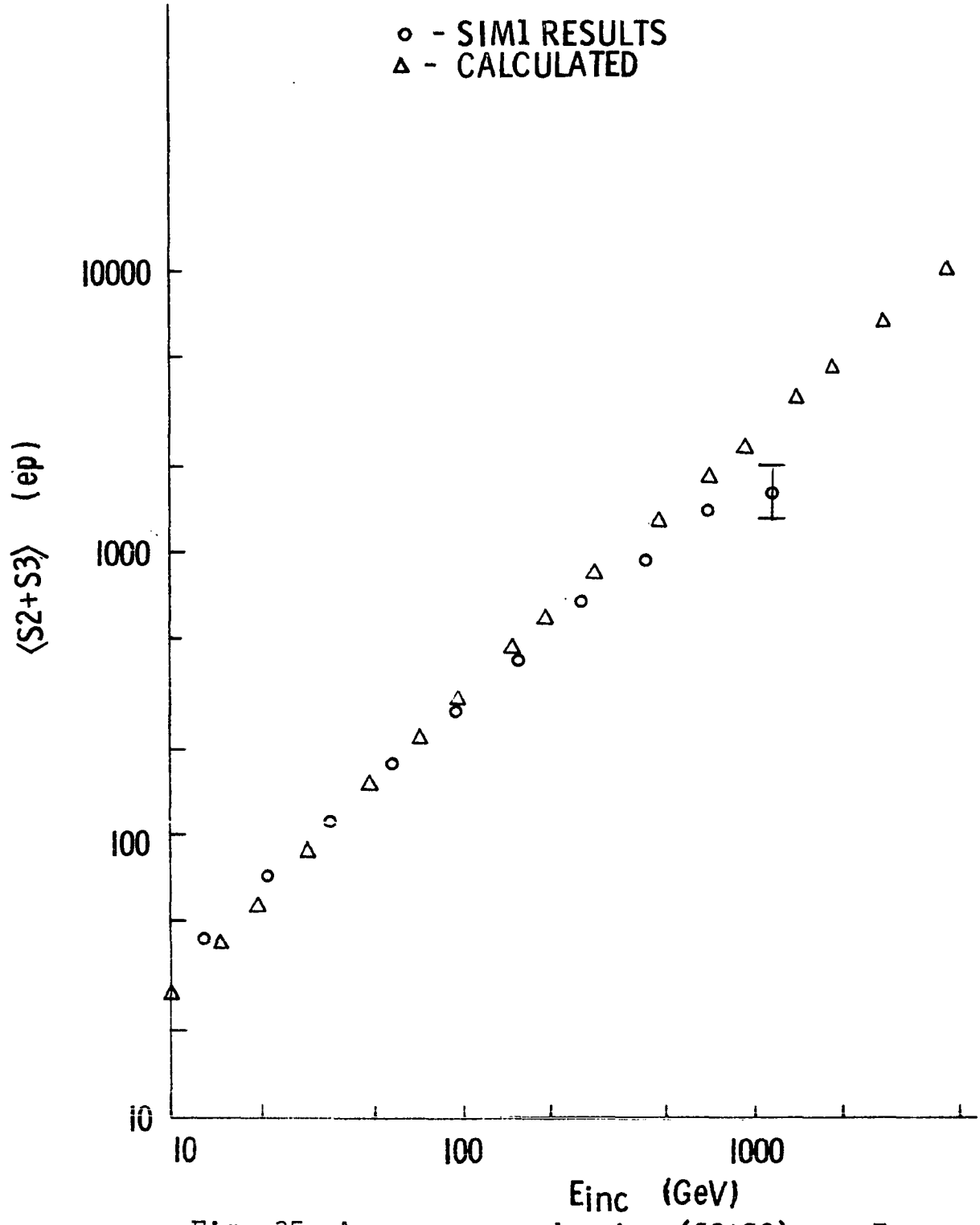

Fig. 35. Average cascade size (S2+S3) vs. E_{inc} for protons from SIM1

used in analyzing the data from operation of the calorimeter.

The longitudinal momenta of photons in the CM frame was calculated for events generated by SIM1. The Feynman variable $x = P_L/P_{Lmax}$ for photons was histogrammed to compare with $d\sigma/dx$ measured by Jaeger *et al.*[34,35] for photons from pp interactions at 12.4 GeV/c and 205 GeV/c. This comparison is made in Fig. 36. The vertical scale is arbitrary, and Jaeger's cross sections have been normalized to match the simulation results at $x = 0$. There is good agreement on the shape of the distributions both at 12.4 GeV/c and at 205 GeV/c.

Fig. 37 shows the distribution of k_γ, the fraction of incident energy given to the electromagnetic cascade, produced by SIM1 for the interactions of 250 GeV protons. The distribution of S3 pulse heights is similar in shape. About half the events have k_γ within a factor of two of the average value .17; this indicates that about half the events will produce S3 pulse heights within a factor of two of the average value for $E_{inc} = 250$ GeV. This may be taken as a measure of the calorimeter's energy resolution.

A major goal of the simulations was to investigate the effects of random variations in k_γ on the observed cosmic ray spectrum. To do this, SIM1 was used to simulate interactions of 10^5 protons with $E_{inc} \geq 10$ GeV distributed according to $\frac{dN}{dE} \propto E^{-2.8}$, which is near the observed cosmic ray

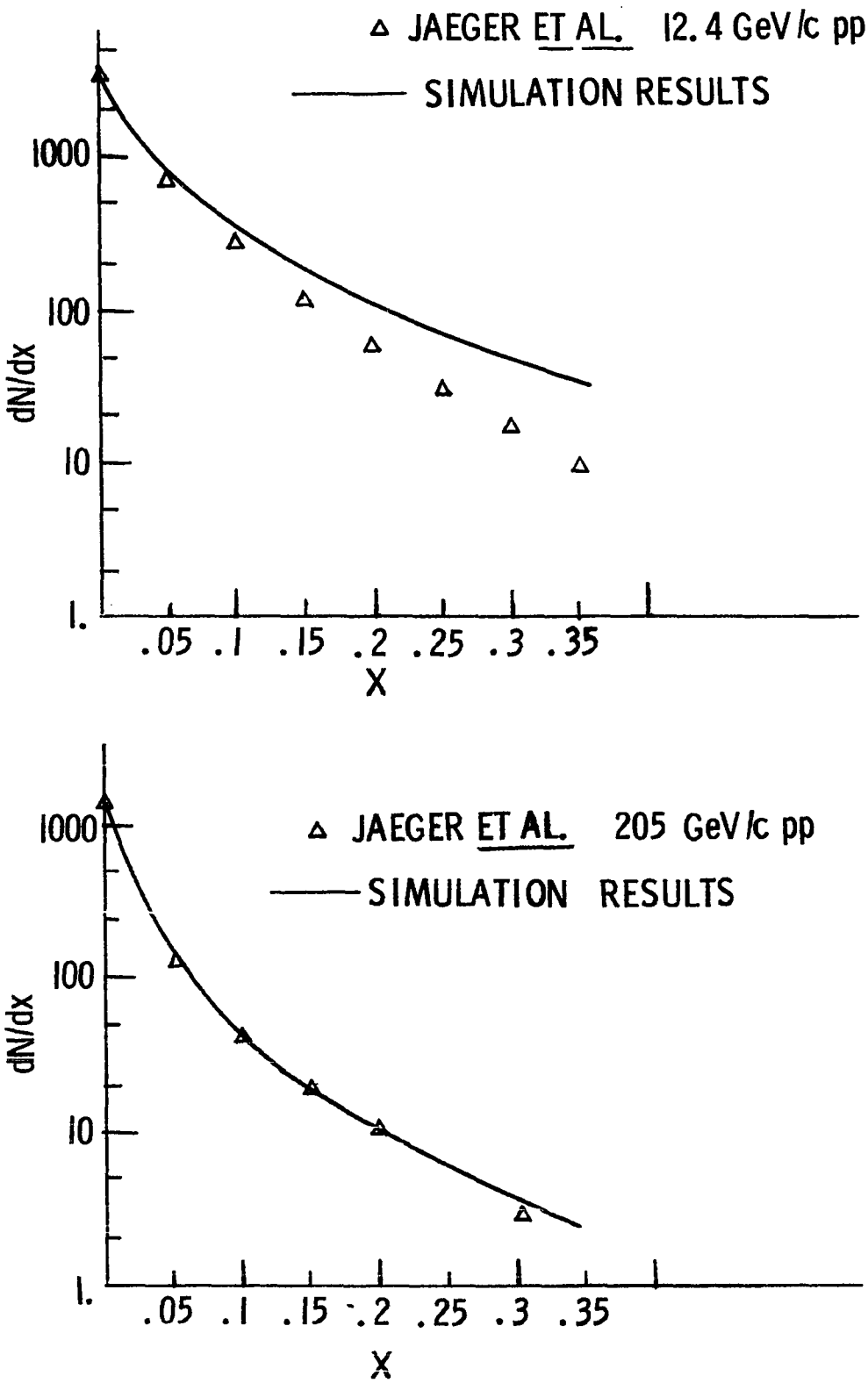

Fig. 36. dN/dx for photons generated by SIM1

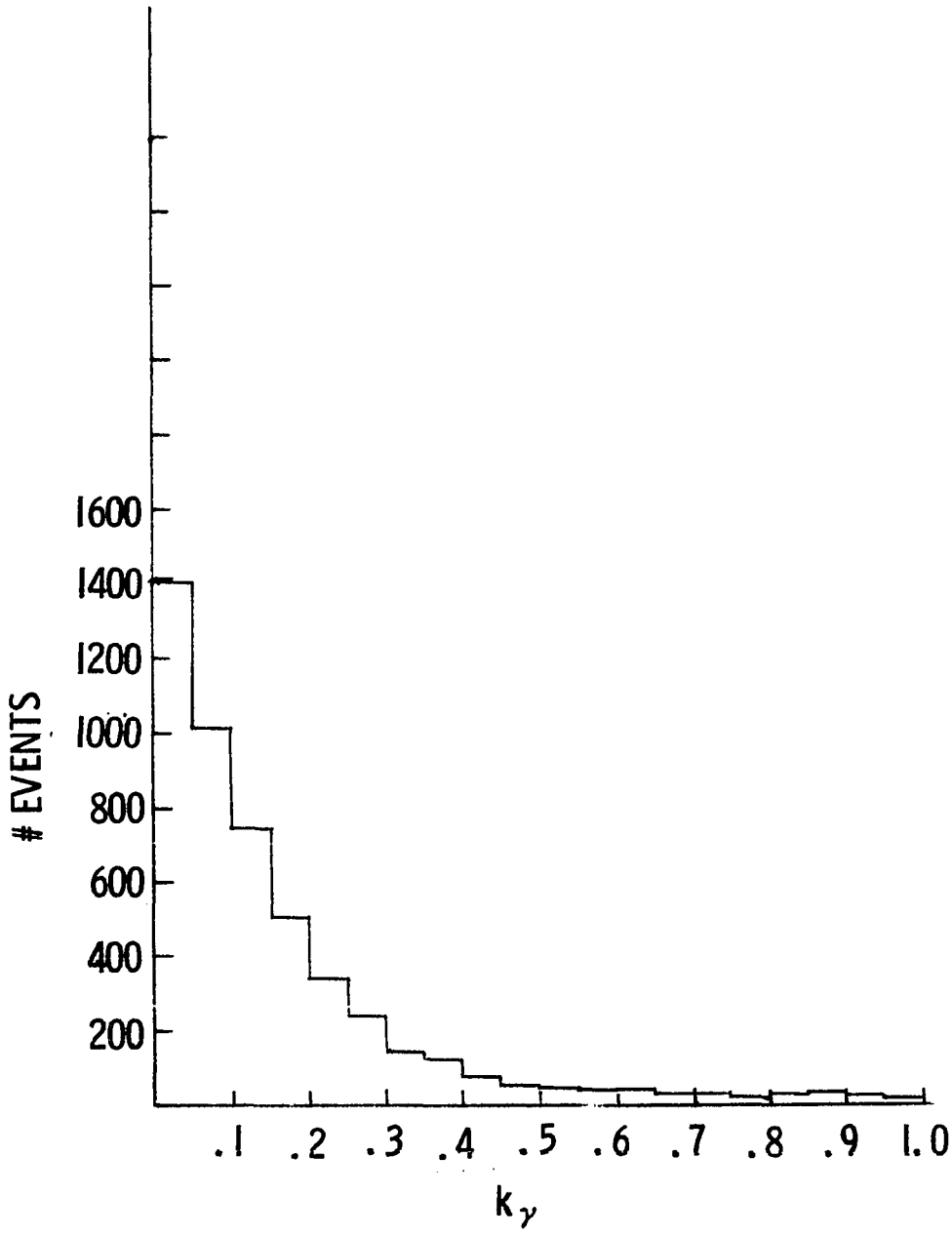

Fig. 37. Histogram of k_γ generated for 250 GeV protons by SIM1

spectral shape. The S3 cascade sizes produced by the interactions were histogrammed. The S3 histogram thus represented the S3 histogram which would be observed by the calorimeter in operation. Since the values of <S3> vs. E_{inc} obtained by the simulation were not judged to be of adequate precision, the observed and simulated S3 spectra were not compared directly. Instead, the simulated values for <S3> vs. E_{inc} were used to convert the simulated S3 spectrum to an energy spectrum, as would be done in data analysis. The energy spectrum thus derived retains any properties introduced by fluctuations in k_γ, but the effects of average values of S3, k_γ, etc. are removed by the conversion. The resulting energy spectrum is that which would be calculated from the observed S3 spectrum assuming that S3 ≡ <S3> at each incident energy for all events. This spectrum can be compared to the incident spectrum assumed for the simulations to see what changes the fluctuations have introduced.

The comparison is shown in Fig. 38. The solid line shows the incident proton spectrum for the simulations. The data points are the spectrum which would be calculated from the calorimeter data under the assumption that S3 ≡ <S3> for all events. It is clear that the calorimeter's energy resolution has no significant effect on the slope of the spectrum. It does, however, affect the absolute intensity found with the calorimeter. This is due to the combined effects of

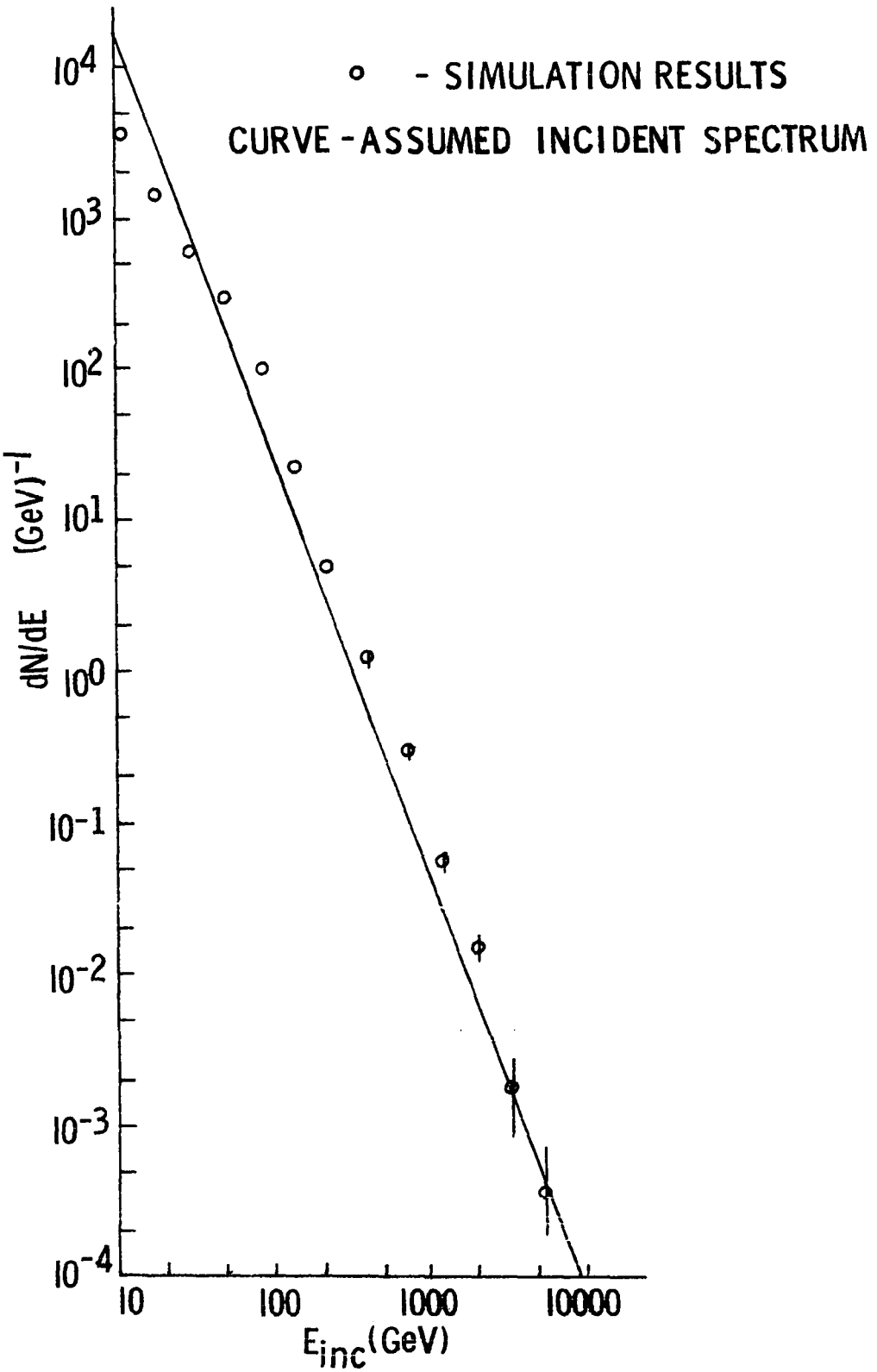

Fig. 38. dN/dE vs. E_{inc} for protons from SIM1

large fluctuations in k_γ and the steepness of the spectrum: events with large k_γ occur with about the same frequency as events with small k_γ, but because they are seen at large S3 where the intensity is much lower, the large k_γ events contribute disproportionately to the observed rate. The effect for SIM1 is to increase the hadron intensity derived from the calorimeter by about a factor of two over that actually present.

SIM1 was not considered a completely adequate model of the calorimeter. The requirement that energy and momentum be conserved resulted in an overabundance of events with large k_γ and, more importantly, the program could not be extended to simulate incident pions. These problems were overcome with SIM2.

Fig. 39 shows $\langle S2+S3 \rangle$ vs. E_{inc} for simulated pions and protons from SIM2. The calculated values shown for comparison are the same as those in Fig. 35. The disagreement with the calculated values is more pronounced than that with SIM1. The reason is that $\langle k_\gamma \rangle$ obtained with SIM2 departs slightly from the values of .17 for protons and .33 for pions which was assumed in obtaining the calculated values. Histograms of photon momenta generated by SIM2 for pp collisions with E_{inc} = 12.5 GeV and 200 GeV are given in Fig. 40 for comparison with the results of Jaeger; the agreement is good. Histograms of k_γ obtained for incident pions and pro-

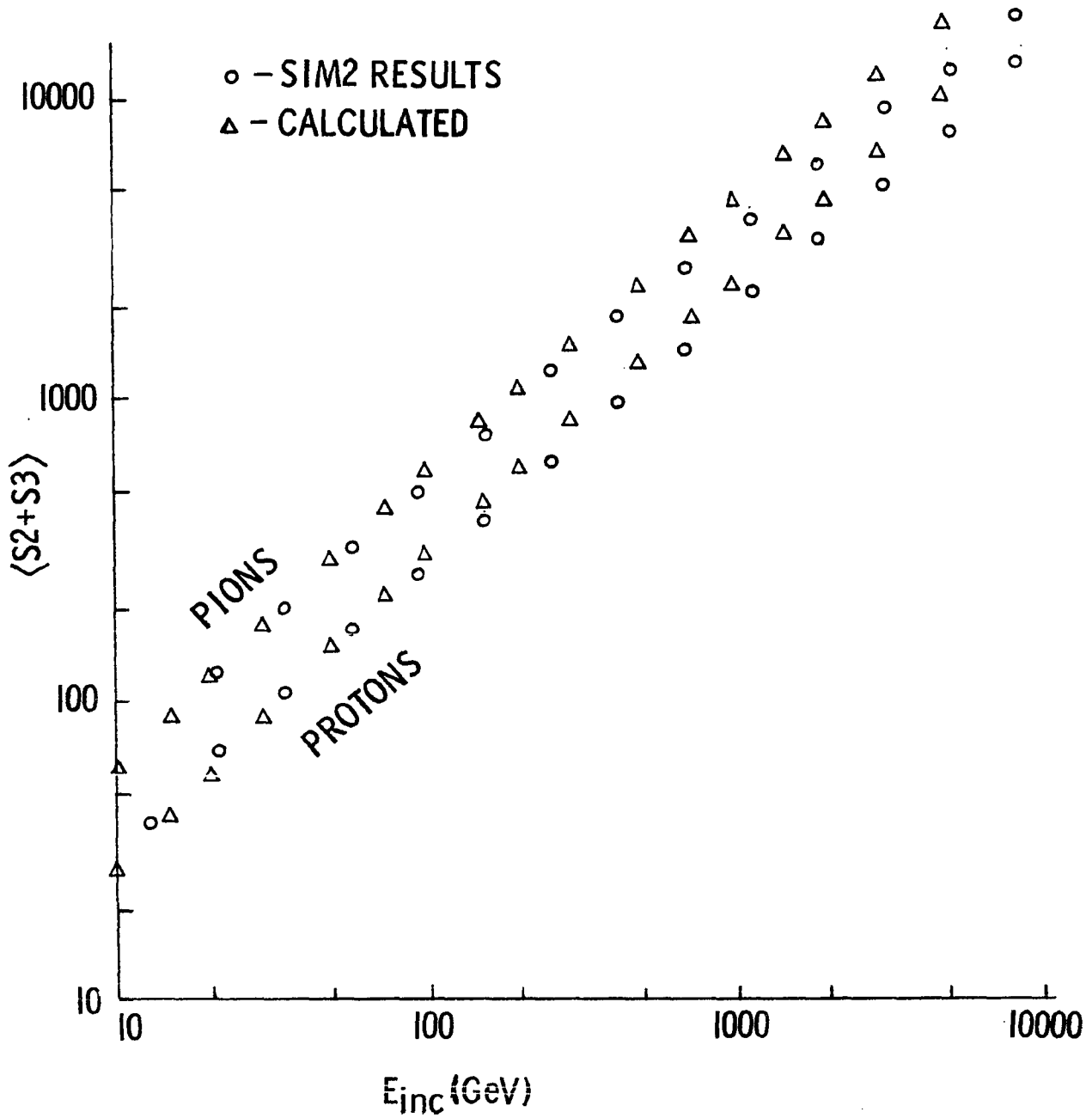

Fig. 39. Average cascade size (S2+S3) vs. E_{inc} for SIM2

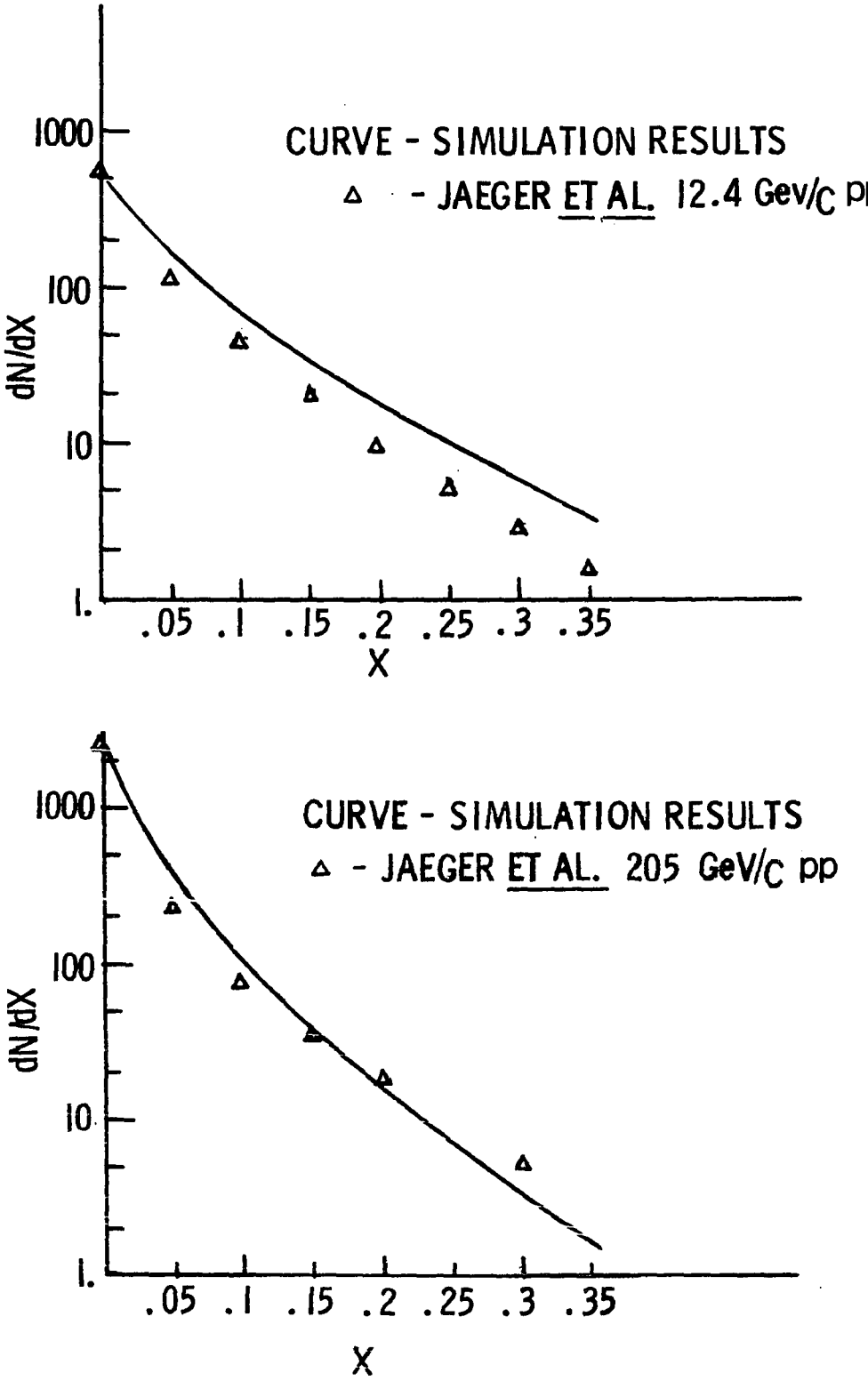

Fig.40 dN/dx for photons generated by SIM2 for incident protons

tons with SIM2 are given in Fig. 41. The energy resolution calculated from the histograms is about a factor of two, in agreement with the results from SIM1.

Simulations of pions and protons from a cosmic ray spectrum were done with SIM2 in the same manner described for SIM1. The incident and simulated "measured" spectra for pions is shown in Fig. 42 while those for protons are shown in Fig. 43. Again the "measured" rates are higher than the assumed hadron intensities, this time by about a factor of 1.6. The slopes of the spectra observed with the calorimeter are identical to the incident spectra, within errors.

The conclusion of the simulations, then, was that fluctuations in k_γ cause the observed rates to be larger by a factor of 1.6 than would be expected if all events had the same value of k_γ. No effect on the slope of the spectrum was seen, which agrees with expectations under the assumptions that k_γ is constant and $\langle S3 \rangle \propto E_\gamma$. The energy resolution of the calorimeter is about a factor of two.

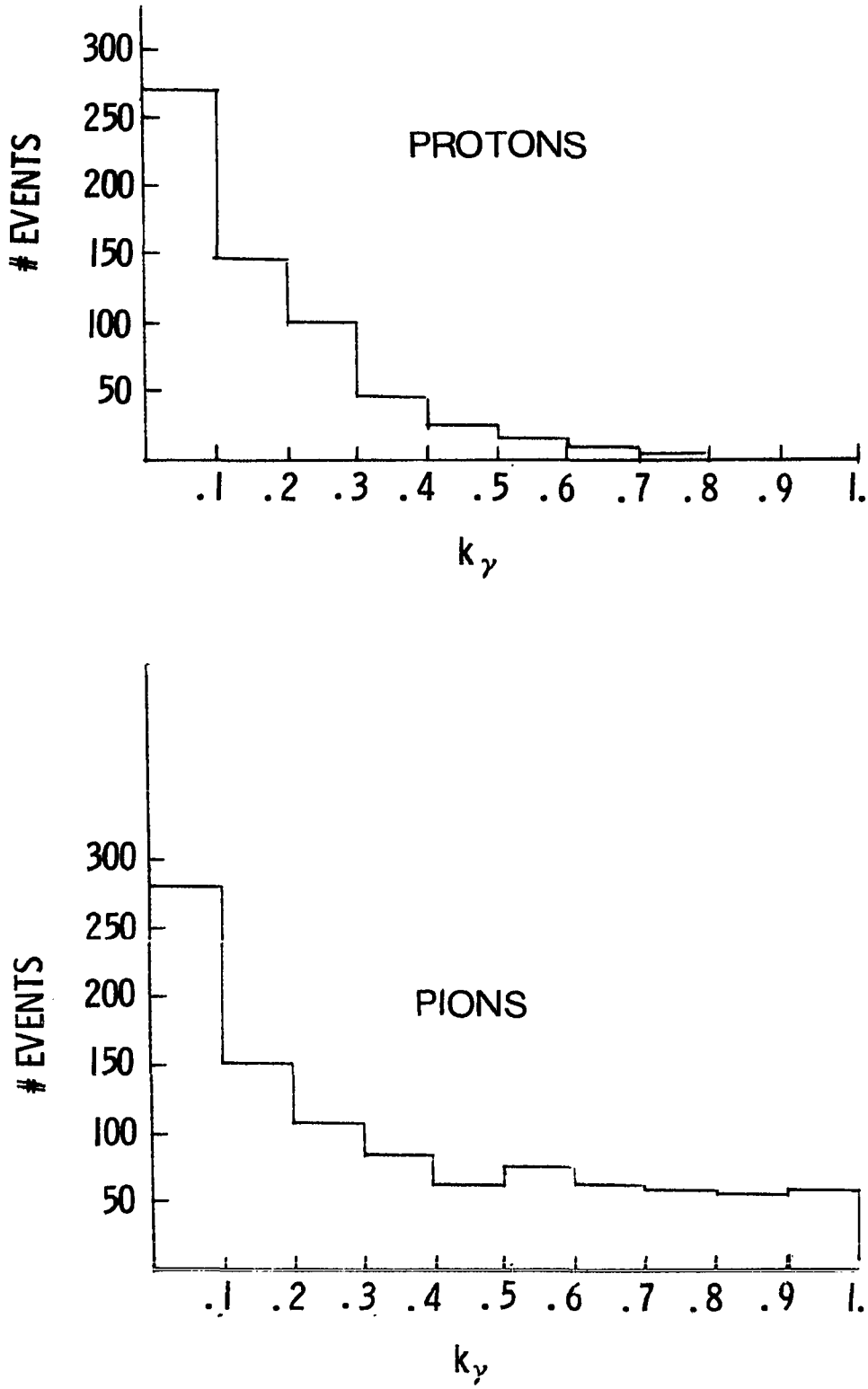

Fig. 41. Histogram of k_γ generated by SIM2 for 250 GeV pions and protons

Fig. 42. dN/dE vs. E_{inc} for pions from SIM2

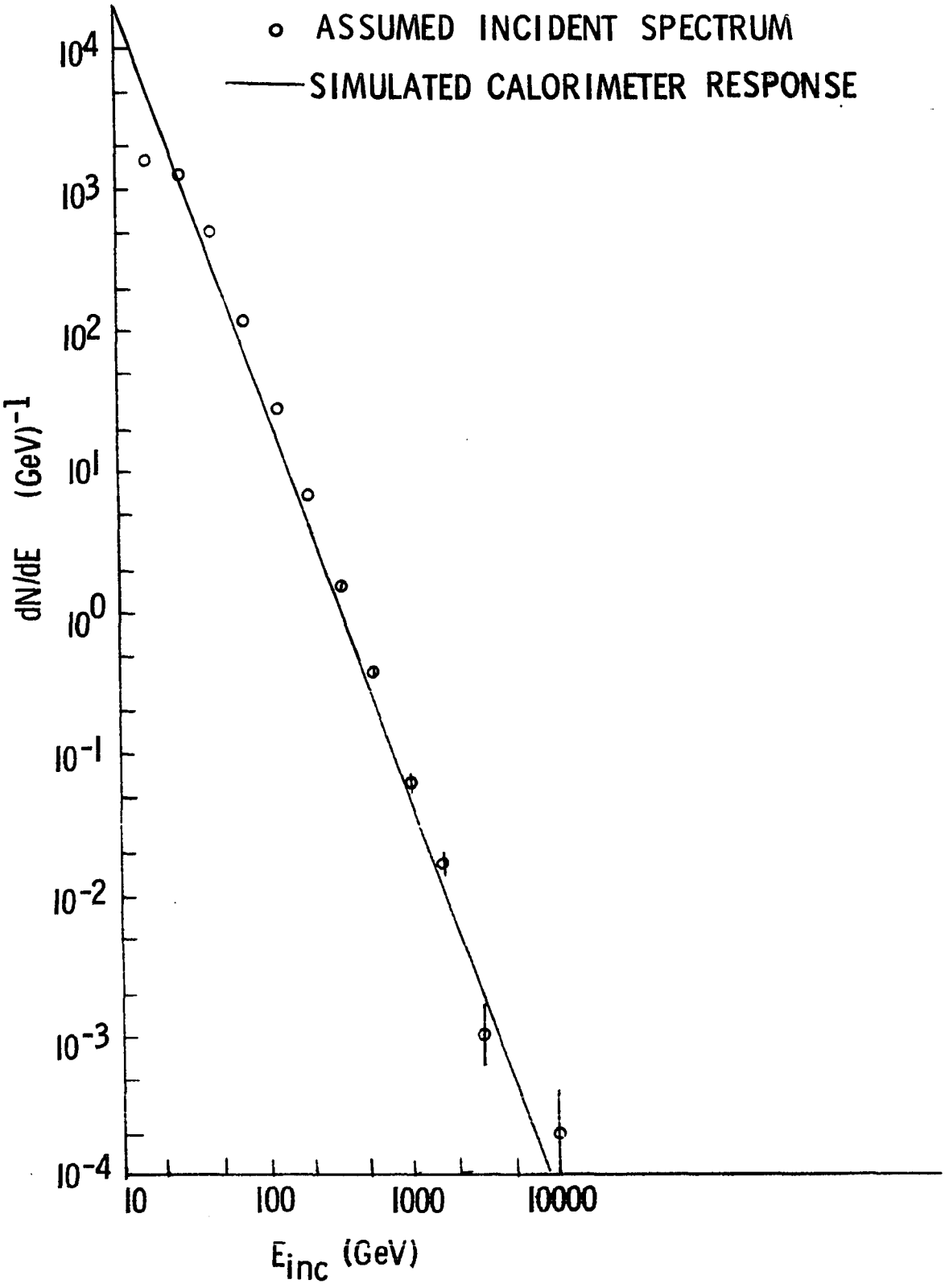
ASSUMED INCIDENT SPECTRUM
SIMULATED CALORIMETER RESPONSE
dN/dE (GeV)$^{-1}$
10^4
10^3
10^2
10^1
10^0
10^{-1}
10^{-2}
10^{-3}
10^{-4}
10
100
1000
10000
E_{inc} (GeV)

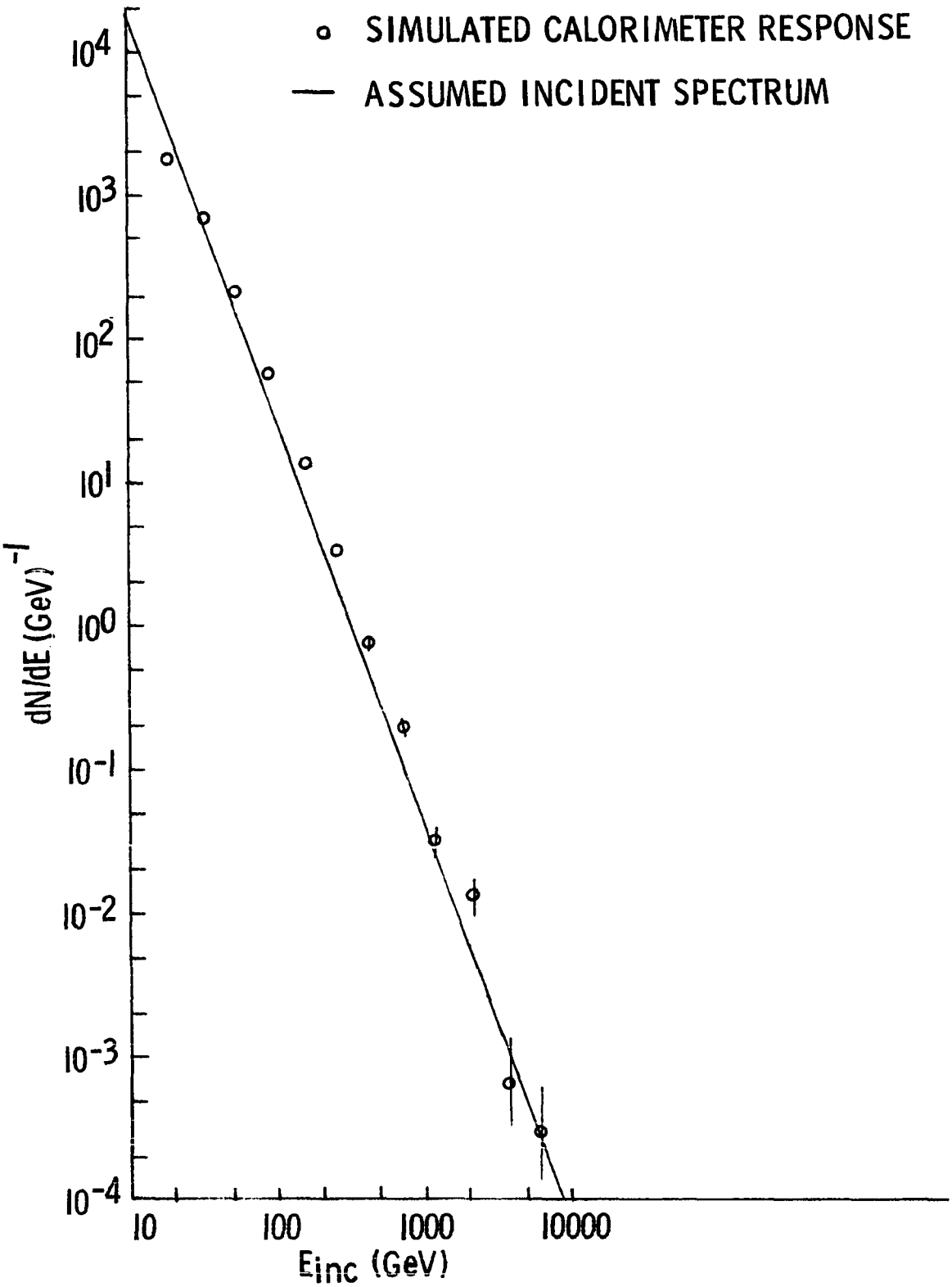

Fig. 43. dN/dE vs. E_{inc} for protons from SIM2

PART II. THE STABILITY OF THE PERIOD OF CYGNUS X-3

INTRODUCTION

This paper describes a study of the periodically variable X-ray source Cygnus X-3. The study began with an invitation to participate with my thesis adviser in a guest observation at MIT using the SAS-3 X-ray astronomy satellite. While the primary interest was a pointed observation of another source using detectors along the satellite's spin axis, Cygnus X-3 was visible in detectors which scan around the satellite's equatorial plane. A study of the time variability of Cygnus X-3 was undertaken to search for evidence that the source's 4.8-hr period is changing.

Models for Cygnus X-3 generally involve a binary system with a 4.8-hr orbital period in which there may be mass transfer from the primary to a compact companion object and/or mass loss from the system. The period is expected to change on a time scale of order $M/\dot{M}$, where M is the total mass of the binary and $\dot{M}$ is its time derivative, the exact relation being model dependent. The period derivative is thus a calculable property of various models which is subject to observation.

In this part of the thesis a summary of some known features of Cygnus X-3 is first given. The observations are then described, and the preliminary data analysis which gave the first evidence of a non-zero period derivative is pre-

sented. A more complete analysis of this same data resulted in a value for the period derivative. A paper based on this analysis will appear in the Astrophysical Journal (Letters)[36]. The results and conclusions of this analysis are discussed in the final sections.

DESCRIPTION OF CYGNUS X-3

Cygnus X-3 was first noted as an X-ray source by R. Giacconi *et al.*[37] in 1967. Its intensity is about 2.5×10^{-9} ergs/cm^2-sec. in 2-10 keV X-rays[38]. The source has also been identified with infrared[39], radio[40], and γ-ray[41] counterparts, but no optical candidate has been found. A distance determination for the radio source by Lauqué *et al.*[42] places it at 8-11 kpc. For an assumed distance of 10 kpc, the 2-10 keV X-ray luminosity is about 3×10^{37} ergs/s, and the total luminosity is $\sim 10^{38}$ ergs/s[43].

The source is variable with a very stable period, found by Parsignault *et al.*[44] to have average value P = .1996814± .0000005 days over the period December 1970-November 1975, with an upper limit on the derivative of $\dot{P}/P \leq 1.6 \times 10^{-5} yr^{-1}$ (2σ). The light curve is roughly sinusoidal and shows no eclipses[45]. The periodic component is more prominent in the γ-ray region, less so in the infrared, and not observed at radio frequencies. Irregular variations on time scales of .1-1 s contain 10% of the X-ray flux[46], and the source intensity also varies by as much as a factor of six over periods of days[47].

The complex behavior of Cygnus X-3 has given rise to a number of models for the system. A compact object such as a white dwarf, neutron star, or black hole is usually assumed to generate X-rays. Most of the models to be considered

assume the 4.8-hr period to be the orbital period of a close binary system, although one model identifies it with the precession period of a neutron star. In discussing these models, it is helpful to derive relations between $\dot{P}$, the period derivative, and various physical properties of the system. This will allow comparison of experimental results from this study with the predictions of the models.

Most models proposed for Cygnus X-3 assume that the 4.8-hr period is the orbital period of a binary system. For this case, the period changes as mass transfer and/or mass loss from the system occurs. The period can be written, in the case of circular orbit, in the form $P = \frac{2\pi}{G^2} \frac{ML^3}{m_1^3 m_2^3}$ where M, L are the total mass and angular momentum of the system and m_1, m_2 are the masses of the two components. The period derivative depends both on the individual masses and on the assumptions made about angular momentum.

If mass is transferred between the two binary components, with total mass and angular momentum remaining constant, the period derivative is given by $\frac{\dot{P}}{P} = -3 \frac{\dot{m}_1}{m_1}\left(1 - \frac{m_1}{m_2}\right)$ Supposing m_2 to be the compact object to which mass is transferred, the period derivative is positive if the compact object is more massive than its companion, and otherwise is negative.

If, on the other hand there is mass loss from the system

and no mass transfer, then, assuming the loss occurs from the mass of the non-compact member m_1, one obtains $\frac{\dot{P}}{P} = \frac{\dot{M}}{M} - \frac{3\dot{m}_1}{m_1} + \frac{3\dot{L}}{L} = \frac{-\dot{m}_1}{m_1}\left(2+\frac{m_2}{M}\right) + \frac{3\dot{L}}{L}$. If no angular momentum is lost, the period derivative is positive. If the lost mass carries the angular momentum it contained as part of m_1, then $\frac{\dot{P}}{P} = \frac{-2\dot{m}_1}{M}$ and again $\frac{\dot{P}}{P}$ is positive.

A. Treves[48] has suggested that the 4.8-hr period of Cygnus X-3 may be the free precession period of a rapidly spinning neutron star. For this situation, he estimates that the rotational period of the neutron star, τ, is about .013 s. If the luminosity is supplied where $\dot{E}$ is the luminosity (about 10^{38} ergs/s). Assuming, as Treves did, that $P \propto \tau^3$, one obtains $\frac{\dot{P}}{P} = \frac{-3}{2}\frac{\dot{E}}{E}$ and the expected change in period is $\frac{\dot{P}}{P} \sim 1.4\times10^{-5}\left(\frac{M}{M_\odot}\right)^{-5/3}\left(\frac{\tau}{10^{-2}s}\right)^{-2}$ yr^{-1}.

THE DATA AND DATA ANALYSIS

In order to search for evidence of a change in the period of Cygnus X-3, measurments of the X-ray intensity were made using the slat detectors[49] of the SAS-3 satellite during the period January 6-12, 1978. The satellite's spin axis was pointed toward the γ-ray source γ195+5, which was the main object of the observation. This placed Cygnus X-3 at an angle of 25° from the satellite's equatorial plane where it was viewed by the center slat detector with a relative efficiency of $\sim$ 0.35.

The center slat detector has an azimuthal angular acceptance of 0.96° FWHM, and a triangular response function. The satellite's spin period during the experiment was 95 minutes, so that Cygnus X-3 was within view for 30 seconds every 95 minutes. The source intensity does not change significantly on a scale of 30 seconds, so that at each scan the count rate as a function of time simply traced out the triangular response of the collimator, with the height of the triangle being proportional to the source's intensity. Data on the count rate as a function of time were available on quick-look plots at the SAS-3 control center. For each scan of Cygnus X-3 the count rate was fitted visually to a triangular response above background and the height of the triangle was measured in millimeters on the plot. This was done for each of 76 scans in which Cygnus X-3 was visible.

To gain a picture of the light curve from the data, the time of each observation was converted to a relative phase in the 4.8-hr period. Taking as a reference time to ≡ JD2443514.00 (the beginning date of the observations) the relative phase for each measurement may be defined $\phi = \frac{t-t_0}{P} - \text{Int}\left(\frac{t-t_0}{P}\right)$ where P is the period of Cygnus X-3, provisonally taken to be $.1996814 \pm .0000005^d$ from the results of Parsignault et al.[44]. The data are plotted as a function of relative phase, ϕ, in Fig. 44. More than one cycle is shown for clarity. The light curve can be seen in rough form in the figure; this is a clear confirmation that the expected 4.8-hr. periodicity is present. The time at which intensity minima occur can be taken together with earlier data published by other observers[44,50] to check the constancy of the 4.8-hr period.

If t_{min} is the time at which minimum intensity occurs, the X-ray intensity can be roughly fitted to the form[50] $I = A_0 - A_1 \cos\left(\frac{2\pi}{P}(t-t_{min})\right)$. The data in Fig. 44 were divided into three sets of ∿ 25 data points each, and for each set a fit to this form was made. A_0 was taken to be the average intensity for the set, P was taken to be $.1996814^d$, and A_1 was initially taken[47] to be .4 A_0, then optimized to improve the fit. t_{min} was fitted as a free parameter from the data. From the three sets of data points, the calculated

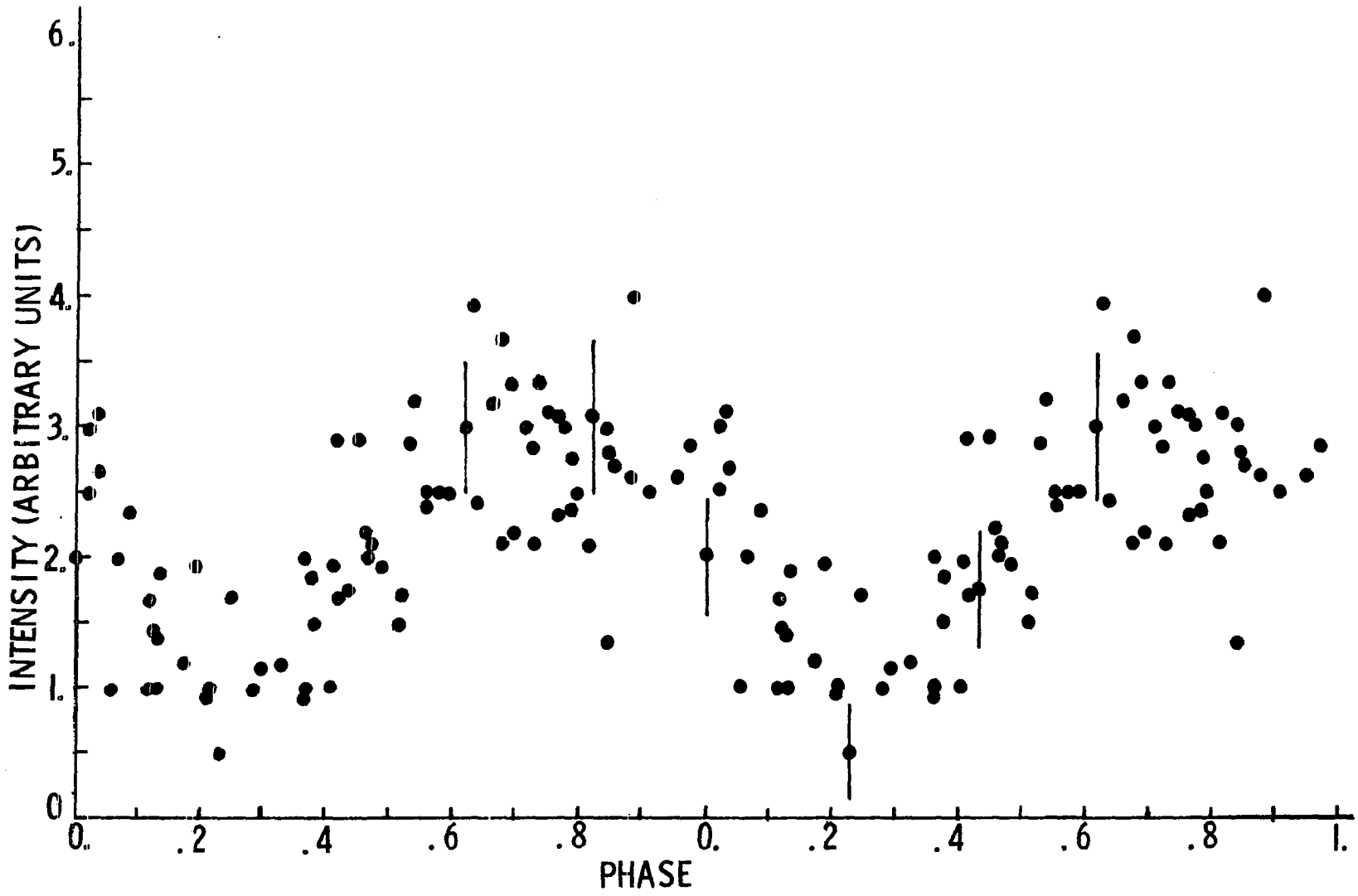

Fig. 44. Intensity vs. relative phase in the 4.8-hr. period

values of t_{min} were JD2443514.00 + .043, .053, and .047 respectively. From these three values the mean value of t_{min} and an estimate of its standard deviation were calculated: t_{min} = JD2443514.0475±.0024. This value refers to the time of arrival of signals from Cygnus X-3 at the center of the solar system, which during the observation differed by $.0024^d$ from the time of arrival at earth.

To determine whether the period of Cygnus X-3 was changing, the value found for t_{min} was compared to an extrapolation of the time of minimum intensity found by Parsignault et al.[44]. They found the value of t_{min} in November 1974 to be JD2442371.4484±.0025 and the average period to be .1996814 $\pm.0000005^d$ for the period 1970 December-1975 November. If the period is assumed to have been constant from December 1970 to January 1978, then 5722 cycles must have elapsed between their measurement in November 1974 and ours in January 1978. If this is the case, the extrapolation to our epoch gives a predicted value t_{min} of $t_{min\ pred}$ = JD2442371.4484±.0025 + (5722) (.1996814±.0000005) = JD2443514.0254±.0038.

A period change near Parsignault et al.'s[44] 2σ upper limit of $1.6\times10^{-5}\,yr^{-1}$ would change t_{min} by only .02 day, so that the phase cannot have "slipped" by a full cycle since the observation of November 1974. Then, comparing our result for t_{min} with the predicted one, it is seen that t_{min} occurs .022 $\pm.0045^d$ later than predicted if $\dot{P} = 0$, where the error in the

predicted and observed values of t_{min} have been combined. This difference is apparently greater than 4σ from zero and can be attributed to an increase in the period of Cygnus X-3.

The simple analysis described above, while adequate to show that the period of Cygnus X-3 has increased, was not able to determine the magnitude of the change. A more complete analysis, including additional data from observations taken January 26 - February 2, 1978, is described in a letter to be published in the Astrophysical Journal[36]. The data of Leach et al.[50], Parsignault et al.[44], and data from this experiment were combined in the analysis to determine $\dot{P}$. Fig. 45 shows the data used in the analysis and the best fit curves for $\dot{P} = 0$ and for $\dot{P} =$ constant. The vertical scale shows the residual phase from a fit with $\dot{P} = 0$. For $\dot{P} \neq 0$, the phase may be written $\phi = \frac{t-t_0}{P_0} - \frac{1}{2}\dot{P}\frac{(t-t_0)^2}{P_0^2}$, where t is the time of observation, t_0 is a reference time, and P_0 is the value of the period at time t_0. Thus the phase for the case of $\dot{P} \neq 0$ shows a quadratic dependence on time. The solid curve in Fig. 45 shows the best quadratic fit to the data, with the fitted values being

$$P_0 = .1996795 \pm .0000007 \text{ days}$$

$$\dot{P}/P = 5.1 \pm 1.3 \times 10^{-6} \text{yr}^{-1}$$

$$t_0 = \text{JD}2440949.9173 \pm .0010$$

The data are adequately represented by this fit with a constant period derivative having the value shown.

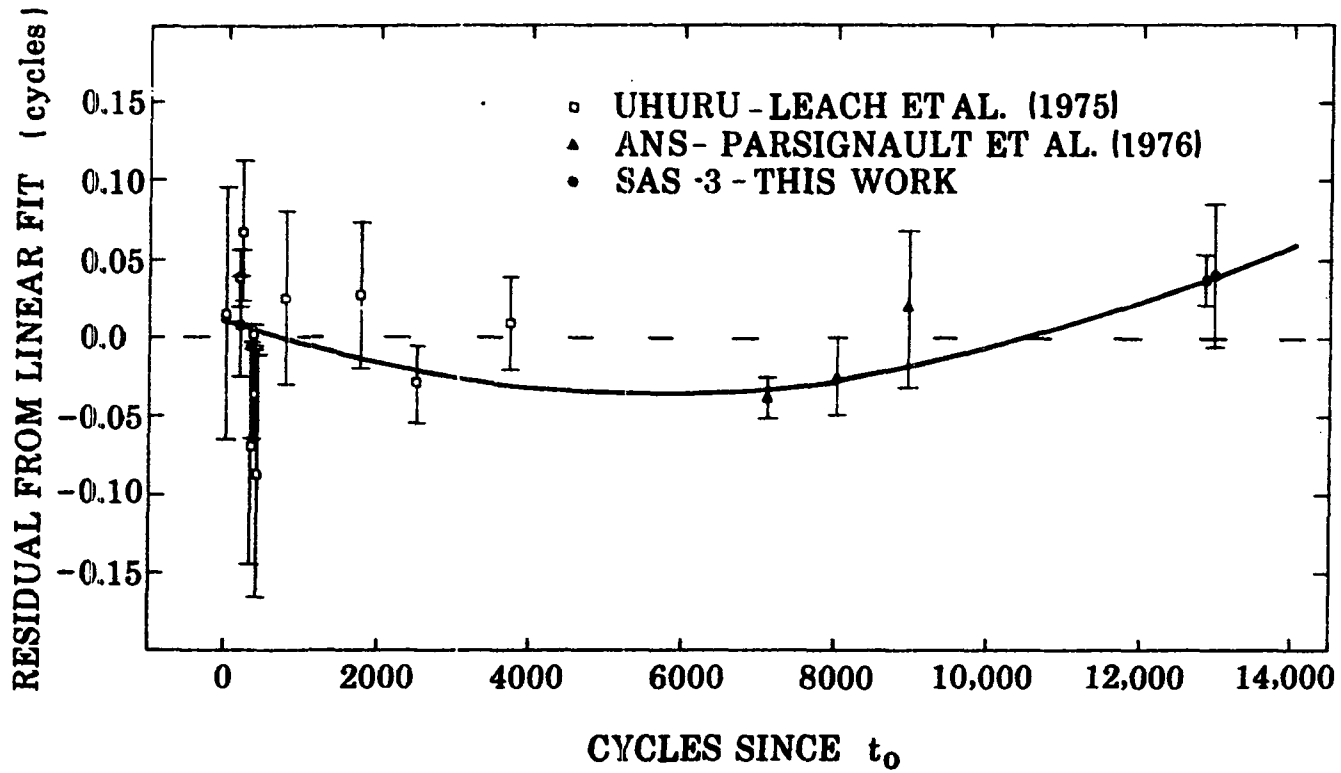

Fig. 45. Residuals from a linear fit to the observations of Cygnus X-3 phase over a 7 year period including data from Leach et al.[50], Parsignault et al.[44], and this work[36]

After this work was completed, we became aware of COS-B observations by Manzo, Molteni, and Robba[51] which, in conjunction with the earlier UHURU and ANS data, give a value of $\dot{P}/P = (5.2\pm1.2)\times10^{-6}yr^{-1}$. Their other parameters, P_0 and t_0, are also in excellent agreement with ours.

DISCUSSION OF RESULTS

The observational results indicate that the phase observed for Cygnus X-3 in January 1978 is not consistent with the hypothesis that the period of Cygnus X-3 is constant. A fit to the data over the $\sim$ 7 year baseline December 1970-January 1978 shows that the period can be adequately represented as changing at a constant rate given by $\dot{P}/P = (5.1\pm1.3)\times 10^{-6}\mathrm{yr}^{-1}$. This rate is consistent with the 2σ upper limit $\dot{P}/P \leq 1.6\times10^{-5}\mathrm{yr}^{-1}$ found by Parsignault *et al.*[44] for the data through 1975 November.

The value found for $\dot{P}/P$ can now be compared to the predictions of models for the Cygnus X-3 system. Several binary models have been proposed in which there is a strong stellar wind from the non-compact object. Davidsen and Ostriker[52] have proposed such a model in which the non-compact object is a white dwarf and its companion is a red dwarf. The wind provides absorption of low-energy X-rays and modulates the X-ray intensity through absorption and scattering with the 4.8-hr orbital period. They estimate that an accretion rate onto the white dwarf of $1.5\times10^{-6}\ M_{\odot}/\mathrm{yr}$ would be required to provide the observed luminosity. A mass loss from the system due to the wind is also expected, and Davidsen and Ostriker accordingly place a lower limit on the expected period derivative: $\dot{P}/P \geq 3.1\times10^{-6}\mathrm{yr}^{-1}$ based on mass loss alone. This is in good agreement with our observational results.

It has been suggested[41] that, since γ-rays of $\sim$ 100 MeV energy are observed, it is likely that Cygnus X-3 is a neutron star rather than a white dwarf. If this is the case, the accretion rate need be only $\sim 3\times10^{-9}\ M_\odot/yr$ to supply the X-ray luminosity. This mass transfer rate alone would produce a period change of only $\dot{P}/P = 6\times10^{-9}yr^{-1}$, well below the observed value. Thus the period derivative must be caused by mass loss in this model. Under the particular assumption that the lost mass carries its orbital angular momentum away the mass rate loss is: $\frac{\dot{M}}{M} = \frac{-1}{2}\frac{\dot{P}}{P} = -2.5\times10^{-6}yr^{-1}$,

A stellar wind model has also been proposed by Pringle[53], who estimates the time scale for period change due to mass loss to be 10^6 yr. This is roughly consistent with our result.

A different picture of the system has been given by M. Milgrom[54] who suggests that, rather than a stellar wind, there is a spherical shell of circumstellar material located outside the binary orbit. Parsignault et al.[47] have estimated the mass loss rate from this shell to be $\sim 10^{-6}M_\odot/yr$. This loss would give rise to a period change comparable to that observed.

The model by A. Treves[48], involving a rapidly rotating neutron star whose free precession period is 4.8-hr, also predicts a changing period. The rate of change calculated

for this model, under the assumption that the luminosity is supplied from rotational energy, roughly agrees with the observational result and has the right sign.

Some general remarks about the implications of the period derivative for binary systems can be made. If the dominant cause of the observed period change is mass transfer, then the compact object must be more massive than its companion to give the correct sign for the change, and the transfer rate must be $\sim 10^{-6} M_\odot/yr$. However, if the compact object is a neutron star, there is no need to assume a mass transfer rate of this size. A neutron star could supply the required luminosity with an accretion of $3 \times 10^{-9} M_\odot/yr$ or from rotational energy with no mass transfer at all. Thus, in a binary system with a neutron star, almost all of the period change is likely to be caused by mass loss. The implied mass loss rate, if the mass carries its orbital angular momentum, is $\frac{\dot{M}}{M} = -2.5 \times 10^{-6} M_\odot/yr$.

CONCLUSION

The phase found for Cygnus X-3 in January 1978 is inconsistent with the hypothesis that Cygnus X-3 has a constant period. An analysis of published data for the period December 1970-January 1978 shows the period to be adequately fit with a continuous change at a rate given by $\dot{P}/P = 5.1 \pm 1.3 \times 10^{-6} \mathrm{yr.}^{-1}$ This rate is consistent in magnitude and sign with several binary models for the system, under the assumption that the period change is caused by mass loss or mass transfer between the binary components. If mass transfer occurs at the rate required to supply the luminosity by accretion onto a neutron star, the dominant cause of period change is mass loss.

CONCLUSION

The study of cosmic ray hadrons described in Part I has yielded results essentially in agreement with the results of a number of other experiments. The spectrum found for charged hadrons in the energy range 3×10^{10}-10^{12} eV is represented by

$$\frac{dN}{dE} = 1.08\pm.35\times10^{-9}\left(\frac{E}{100\ \text{GeV}}\right)^{-2.77\pm.06} \quad (\text{cm}^2\text{-sr-s-GeV})^{-1}.$$

An upper limit on the π/p ratio was found of $\pi/p \leq 0.94$ (2σ), which is consistent with the result of Brooke *et al.*[3] but not consistent with the value found by Cowan and Matthews[12] at higher energies. No evidence for massive particles was found, with an upper limit on the massive particle flux of $\phi_m \leq 1.5\times10^{-7}$ $(\text{cm}^2\text{-sr-s})^{-1}$ for particles with masses of 5-30 GeV/c^2.

In Part II, observations of Cygnus X-3 have been presented which show evidence that this source's 4.8-hr period is increasing. The rate found for the increase is given by $\frac{\dot{P}}{P} = 5.1\pm1.3\times10^{-6}\text{yr.}^{-1}$ This result is consistent with previous upper limits on the period derivative. Several models for the system predict period derivatives which are in agreement with this value both in magnitude and sign. If the system is a binary in which one component is a neutron star, the period change is not closely tied to the energetics of the system and may be caused mainly by mass loss from the system. For this

case, a mass loss rate of $\frac{\dot{M}}{M} = -2.5 \times 10^{-6} M_{\odot}/yr$ will produce the observed change in period.

BIBLIOGRAPHY

1. B. Rossi, in High-Energy Particles, edited by Donald H. Menzel (Prentice-Hall, Inc., New York, 1952).

2. G. Brooke, and A.W. Wolfendale, Proc. Phys. Soc. (London) 83, 843-851 (1964).

3. G. Brooke, A. Meyer, and A.W. Wolfendale, Proc. Phys. Soc. (London) 83, 871-877 (1964).

4. F. Ashton, in Cosmic Rays at Ground Level, edited by A.W. Wolfendale (The Institute of Physics, London and Bristol, 1973), p. 75.

5. O.C. Allkofer, K. Carstensen, and W.D. Dav, in Proceedings of the 12th International Conference on Cosmic Rays, Hobart, (University of Tasmania, 1971), vol.4, p. 1314.

6. J.E.F. Baruch, G. Brooke, and E.W. Kellermann, in Proceedings of the 12th International Conference on Cosmic Rays, Hobart, (University of Tasmania, 1971), vol. 4, p. 1301.

7. J.E.F. Baruch, G. Brooke, and E.W. Kellermann, Nature Phys. Sci. 242, L6 (1973).

8. J.E.F. Baruch, G. Brooke, and E.W. Kellermann, in Proceedings of the 12th International Conference on Cosmic Rays, Hobart, (University of Tasmania, 1971), vol. 6, p. 2301.

9. I.S. Diggory, H.G. Dixon, J.C. Earnshaw, J.R. Hook, I.A. Jenkins, G.C. Maslin, B.D. O'Donnell, K.J. Orford, and K.E. Turver, in Proceedings of the 12th International Conference on Cosmic Rays, Hobart (University of Tasmania, 1971), vol. 3, p. 1236.

10. F. Siohan, M. LaPointe, J.R. MacFall, A. Stottlemeyer, R.W. Ellsworth, and G.B. Yodh, in Proceedings of the 13th International Conference on Cosmic Rays, Denver (Univer- of Denver, 1973), vol. 4, p. 2532.

11. N.L. Grigorov, V.S. Murzin, and I.D. Rapaport, JETP 7, 348 (1958).

12. G.W. Cowan, and K. Matthews, Phys. Rev. D4, 37 (1971).

13. V.A. Dmitriev, G.V. Kulikov, and G.B. Khristiansen, JETP 37(10), 637 (1960).

14. J.E.F. Baruch, G. Brooke, and E.W. Kellermann, Acta Physica Academiae Scientiarum Hungarica 29, suppl. 4, 493 (1969).

15. F. Ashton, and A.J. Saleh, Nature Phys. Sci. 256, 387 (1975).

16. W.K. McFarlane, Rev. Sci. Instr. 45, 286 (1974).

17. D. Müller, Phys. Rev. D5, 2677 (1972).

18. J. Whitmore, Phys. Rep. 10C, 273 (1974).

19. C.J. Crannell, H. Crannell, C.R. Gillespie, K. Pinkau, and R.R. Whitney, Phys. Rev. 182, 1435 (1969).

20. T.K. Gaisser, and G.B. Yodh, in Proceedings of the 13th International Conference on Cosmic Rays, Denver (University of Denver, 1973), vol. 3, p. 2140.

21. L.W. Jones, Rev. Mod. Phys. 49, 717 (1977).

22. L.W. Jones, D.E. Lyon, Jr., P.V. Ramana Murthy, G. DeMeester, R.W. Hartung, S. Mikamo, D.D. Reeder, A. Subramanian, B. Cork, B. Dayton, A. Benvenuti, E. Marquit, P.D. Kearney, A.E. Bussian, F. Mills, C. Radmer, and W.R. Winter, Phys. Rev. 164, 1584 (1967).

23. G.M. White, and J.R. Prescott, Acta Physica Academiae Scientiarum Hungarica 29, suppl. 3, 31 (1969).

24. S.C. Tonwar, R.V. Sreekantan, and R.H. Vatcha, Pramana 8, 50 (1977).

25. J.E.F. Baruch, G. Brooke, C.H. Huang, E.W. Kellermann, and W.D. Wallter, in Proceedings of the 14th International Cosmic Ray Conference, (May-Plank-Institut fur Extraterrestrische Physik, Munich, 1975), vol. 12, p. 4303.

26. R.P. Kokoulin, and A.A. Petrukhin, Acta Physica Academiae Scientarium Hungarica 29, suppl. 4, 277 (1969).

27. A.A. Petrukhin, and V.V. Shestakov, Can. J. Phys. 46, S377 (1968).

28. P. Slattery, Phys. Rev. Lett. 29, 1624 (1972).

29. J. Whitmore, Phys. Rep. 27C, 187 (1975).

30. D.C. Carey, J.R. Johnson, R. Kammerud, D.J. Ritchie, A. Roberts, J.R. Sauer, R. Shafer, D. Theriot, J.K. Walker, and F.E. Taylor, Phys. Rev. D14, 1196 (1976).

31. F.E. Taylor, D.C. Carey, J.R. Johnson, R. Kammerud, D.J. Ritchie, A. Roberts, J.R. Sauer, R. Shafer, D. Theriot, and J.K. Walker, Phys. Rev. D14, 1217 (1976).

32. J. Friedman, SLAC Computational Group Technical Memo 145 (1972) (unpublished).

33. J.H. Friedman, G.R. Lynch, C.G. Risk, and T.A. Zang, J. Comp. Phys. 8, 1 (1971).

34. K. Jaeger, J. Campbell, G. Charlton, D. Swanson. C. Fu, H.A. Rubin, R.G. Glasser, D. Koetke, and J. Whitmore, Phys. Rev. D11, 1756 (1975).

35. K. Jaeger, D. Colley, L. Hyman, and J. Rest, Phys. Rev. D11, 2405 (1975).

36. R.C. Lamb, R.G. Dower, and R.K. Fickle, to be published in the Astrophysical Journal (Letters) (1979).

37. R. Giacconi, P. Gorenstein, H. Gursky, and J.R. Waters, Ap. J. 148, L119 (1967).

38. R.H. Becker, J.L. Robinson - Saba, E.A. Boldt, S.S. Holt, S.H. Pravdo, P.S. Serlemitsos, and J.H. Swank, Ap. J. 224, L113 (1978).

39. E.E. Becklin, J. Kristian, G. Neugebauer, and G.G. Wynn-Williams, Nature Phys. Sci. 239, 130 (1972).

40. L.L.E. Braes, and G.K. Miley, Nature 237, 506 (1972).

41. R.C. Lamb, C.E. Fichtel, R.C. Hartman, D.A. Kniffen, and D.J. Thompson, Ap. J. 212, L63 (1977).

42. R. Lauqué, J. Lecueux, and N.Q. Rieu, Nature Phys. Sci. 239, L119 (1972).

43. G.F. Bignami, L. Maraschi, and A. Treves, Astron. Astrophys. 55, 155 (1977).

44. D.R. Parsignault, E. Schreier, J. Grindlay, and H. Gursky, Ap. J. 209. L73 (1976).

45. K.O. Mason. E.E. Becklin, L. Blankenship. R.L. Brown, J. Elias, R.M. Hjellming, K. Matthews, P.G. Murdin, G. Neugebauer, P.W. Sanford, and S.P. Willner, Ap. J. 207, 78 (1976).

46. W. Forman, C. Jones, and H. Tananbaum, Ap. J. 208. 849 (1976).

47. D.R. Parsignault, J. Grindlay, H. Gursky, and W. Tucker, Ap. J. 218, 232 (1977).

48. A. Treves, Nature Phys. Sci. 242, 121 (1973).

49. J. Buff, G. Jernigan, B. Laufer, H. Bradt, G.W. Clark, W.H.G. Lewin, T. Matilsky, W. Mayer, and F. Primini, Ap. J. 212, 768 (1977).

50. R.W. Leach, S.S. Murray, E.J. Schreier, H.D. Tananbaum, M.P. Ulmer, and D.R. Parsignault, Ap. J. 199, 184 (1975).

51. G. Manzo, D. Molteni, and N.R. Robba, Astron. Astrophys. 70, 317 (1978).

52. A. Davidsen, and J.P. Ostriker, Ap. J. 189, 331 (1974).

53. J.E. Pringle, Nature 247, L21 (1974).

54. M. Milgrom, Astron. Astrophys. 51, 215 (1976).

ACKNOWLEDGMENTS

First of all, I would like to thank my wife, Susan, for doing all of the typing and many of the illustrations, generally getting all the "little" details finished, cracking the whip as needed, and in general showing the kind of love and support which brought this work to a successful conclusion.

I would like to thank my major professor, R.C. Lamb, for his contributions to all phases of the work described in this thesis, and most especially for his encouragement when things went badly.

Thanks are also due to a number of other people for particular contributions to this research: to D.L. Parker for help with the hadron event simulations described in Appendix II; to W.J. Kernan for loaning equipment from the High Energy Physics Group for use in the cosmic ray experiment; and to Richard Brown for help in the physical construction of the cosmic ray apparatus.

Finally, thanks are due to those who provided financial support for this work. The work on Cygnus X-3 was supported in part by the National Aeronautics and Space Administration. Funds for the cosmic ray research project were provided by the Iowa State University Research Foundation.